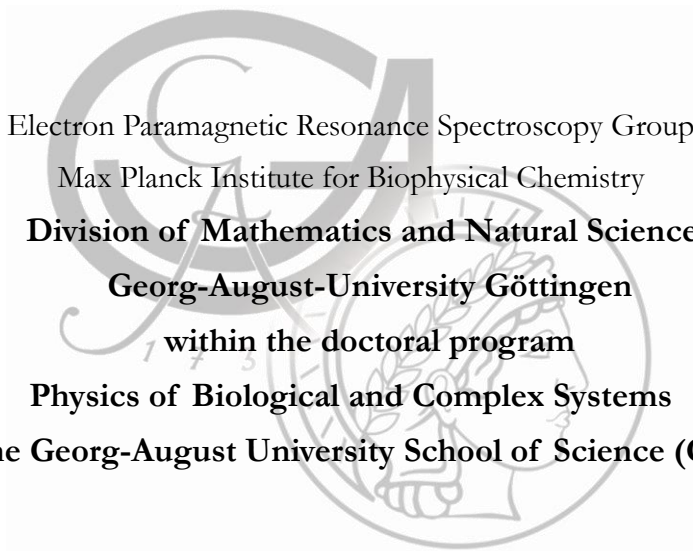


Dissertation  
for the award of the degree  
„Doctor rerum naturalium”

**LONG-RANGE EPR DISTANCE MEASUREMENTS**  
**WITH SEMI-RIGID SPIN LABELS**  
**AT Q-BAND FREQUENCIES**



Electron Paramagnetic Resonance Spectroscopy Group  
Max Planck Institute for Biophysical Chemistry  
**Division of Mathematics and Natural Sciences**  
**Georg-August-University Göttingen**  
within the doctoral program  
**Physics of Biological and Complex Systems**  
of the Georg-August University School of Science (GAUSS)

submitted by

Karin Halbmaier

from Rathenow

Göttingen 2016



Members of the PhD Thesis Committee:

**Prof. Dr. Marina Bennati (Reviewer)**

Electron Paramagnetic Resonance Spectroscopy Group  
Max Planck Institute for Biophysical Chemistry  
&  
Institute for Organic and Biomolecular Chemistry  
Georg August University – Göttingen

**Prof. Dr. Ulf Diederichsen (Reviewer)**

Institute for Organic and Biomolecular Chemistry  
Georg August University – Göttingen

**Prof. Dr. Markus Zweckstetter**

Structure Determination of Proteins Using NMR  
Max Planck Institute for Biophysical Chemistry

**Prof. Dr. Claudia Steinem**

Institute for Organic and Biomolecular Chemistry  
Georg August University – Göttingen

**Prof. Dr. Claudia Höbartner**

Institute for Organic and Biomolecular Chemistry  
Georg August University – Göttingen

**Prof. Dr. Michael Meinecke**

European Neuroscience Institute  
Georg August University – Göttingen

**Date of the oral examination:**

11.11.2016



## **Declaration**

I hereby declare that this thesis has been written independently and with no other sources and aids than quoted.

Karin Halbmaier

Göttingen, August 31<sup>st</sup> 2016



## Acknowledgements

Firstly, I sincerely thank Prof. Dr. Marina Bennati for offering me the opportunity for a doctoral thesis by providing a position, a project and most importantly enthusiastic scientific guidance. Numerous discussions pushed me to grow my scientific understanding. Above that she offers navigation through the scientific world and advice on obstacles beyond science, which I truly appreciate. She cares about her students in all senses and I am happy to have her as my “Doktormutter” as she truly deserves this term.

My gratitude also goes to the members of my thesis committee Prof. Ulf Diederichsen and Prof. Markus Zweckstetter who accompanied my research the last four years by offering advice and improving my research by challenging discussions.

Dr. Igor Tkach deserves my credit and thanks for always helping handling little disasters not only by generously sharing his scientific and technical skills but also in the kindest way.

The whole EPR spectroscopy group created an atmosphere of collegiality, support and trust, which I do not take for granted and I am thankful for. I want to thank my (former) fellow PhD students Isa, Thomas, Nikolay and Roberto for sharing this experience with all its fantastic and challenging aspects and their friendship, as well as Dr. Tomas Orlando, Dr. Roberta Pievo and Dr. Guoquan Liu for sharing their experience and being always helpful. Brigitta Angerstein I want thank for practical help especially with sample preparation.

The content of this thesis could not have been created without collaborators. Here I want to thank Prof. Claudia Höbartner for her cooperation in the RNA project and Jan Seikowski for synthesizing the spin labelled RNA samples. I also thank Prof. Ulf Diederichsen for the cooperation on the WALP project and Janine Wegener for synthesis of the samples. Working with Janine was always easy even when the project

was tough as she is positive and interested, which led to a very close collaboration.

A very special place in these acknowledgments is reserved for Dr. Müge Kasanmascheff. She is enthusiastic and courage scientist who really helped me to develop my professional action and independence. More than once she infected me with her positive energy when I lost mine. Even more importantly she is a supporting and loving friend I do never want to miss.

I thank Tim from the bottom of my heart for being incredibly supporting and understanding during times when I nearly went crazy upon the challenges arising with righting a PhD thesis. He has been my anchor to the real life. I also want to use the opportunity to thank Nadja for being there and encouraging me to stay strong, if necessary three times per day.

The deepest gratitude goes my parents Renate and Ulrich. Their unconditional support and love empowered me to grow to the person I am now. They found this perfect balance between encouraging independence and offering a strong boundary of a home I can always come back to. I also want to thank my brothers Matthias and Sebastian who had an essential influence on my education and really carried me through the hardest of times.



## Abstract

Elucidating the structure of biomolecules is essential to understand their function. Pulsed electron double resonance (PELDOR) in conjunction with site-directed spin labelling has become a well-established experiment for measuring long-range distances between paramagnetic centres. In this thesis the capacity of PELDOR distance measurements performed Q-band frequency (34 GHz/1.2 T) employing a high power microwave amplifier in conjunction with spin labels of reduced mobility is demonstrated. It is shown that the high microwave power does not only enable high sensitivity in PELDOR experiments but also allows to suppress artefacts arising from orientation selection. The power of this method is documented for two representative biological model system spin labelled with distinct semi-rigid nitroxides.

Distances up to 8 nm could be recorded with high accuracy (error in the main distance  $\leq 0.1$  nm) on a ribonucleic acid (RNA) duplex labelled with a TEMPO-based nitroxide called  $C^T$  that is attached to a cytosine.  $C^T$  is preserving Watson-Crick base-pairing capability, which restricts it to a small conformational space. Therefore subtle dynamics of the RNA itself could be observed. The narrow width of the distance distributions obtained in the experiment ( $\Delta r \leq 0.5$  nm) suggest overall small deviations of the duplex from an ideal A-form RNA.

A transmembrane model peptide (WALP24) labelled with the standard MTSSL as well as the unnatural amino acid TOPP was investigated by EPR distance measurements in solution and two different lipid environments. A comparison between WALP24-MTSSL and WALP24-TOPP, clearly reveals the superiority of the rigid TOPP label, as it delivers sharp one-peak inter-spin distances ( $\Delta r \leq 0.4$  nm) even in the

lipid environment. In contrast MTSSL reported broad distances that do show a strong dependence on the hydrophobic thickness of the bilayer, suggesting an adaption of the flexible label to the lipid environment, which results in a loss of information on peptide structure.

## Contents

<b>1 . Chapter Biophysical Methods for Structural Biology – A Place for Electron Paramagnetic Resonance .....</b>	<b>1</b>
<b>2 . Chapter Introduction and Theory of EPR Distance Measurements .....</b>	<b>7</b>
2.1 Concept of EPR Distance Measurements.....	7
2.1.1 Electron Spin-Spin Dipolar Coupling .....	7
2.1.2 EPR Techniques to Probe the Dipolar Coupling .....	11
2.2 Pulsed Electron Double Resonance (PELDOR) .....	14
2.2.1 The Four-Pulse PELDOR/DEER Experiment.....	15
2.2.2 Orientation Selection in PELDOR.....	20
2.2.3 Analysis of Experimental Data .....	25
2.2.4 PELDOR vs. Other Techniques of Pulsed Dipolar Spectroscopy .....	30
<b>3 . Chapter Introduction to Site-Directed Spin Labelling EPR .....</b>	<b>33</b>
3.1 Strategies for Site-Directed Spin Labelling.....	33
3.2 Spin Label Classes.....	36
3.2.1 Metal-Based Spin Labels.....	36
3.2.2 Carbon-Centred Organic Radicals .....	37
3.3 Nitroxide Spin Labels.....	38
3.3.1 Nitroxide Spin Labels for Nucleic Acids .....	40
3.3.2 Nitroxide Labels for Proteins .....	43
<b>4 . Chapter Scope of the Thesis .....</b>	<b>48</b>
4.1 High-Power PELDOR at Q band - Motivation.....	48
4.1.1 Ribonucleic Acids (RNA).....	50
4.1.2 Transmembrane Helices (WALP) .....	51
<b>5 . Chapter General Experimental Setup for PELDOR Experiments Reported in this Thesis.....</b>	<b>56</b>
<b>6 . Chapter PELDOR on <sup>13</sup>C-Labelled Ribonucleic Acid – Measurement of Long Distances.....</b>	<b>61</b>
6.1 Materials and Methods.....	61

6.1.1	Preparation of EPR Samples .....	63
6.1.2	PELDOR/DEER Experiments.....	64
6.1.3	Construction of Molecular Model of C <sup>T</sup> -labelled RNA.....	66
6.1.4	Simulation of Orientation Selective PELDOR Traces .....	67
6.2	Results on C <sup>T</sup> -labelled RNA.....	68
6.2.1	Examination of Orientation Selection.....	68
6.2.2	Long-Range Distance Measurements .....	79
6.2.3	Error Estimation - Effect of Trace Length and Background Subtraction .....	84
6.3	Discussion of PELDOR Experiments on C <sup>T</sup> -labelled RNA .....	91
<b>7</b>	<b>Chapter PELDOR on TOPP-labelled Transmembrane Peptides – Distance Measurements in Lipid Bilayers .....</b>	<b>95</b>
7.1	Materials and Methods.....	95
7.1.1	Preparation of EPR samples.....	96
7.1.2	PELDOR/DEER Experiments.....	98
7.1.3	Construction of Molecular Model of TOPP and MTSSL- labelled WALP24.....	99
7.1.4	Experiments and Simulation of Orientation Selective PELDOR on WALP24-TOPP.....	100
7.2	Results on TOPP and MTSSL-labelled WALP24.....	101
7.2.1	Examination of Orientation Selection.....	101
7.2.2	PELDOR Experiments in Solution.....	107
7.2.3	PELDOR/DEER Experiments in Lipid Environment .....	108
7.3	Discussion of PELDOR Experiments on MTSSL- and TOPP- Labelled WALP24 .....	112
<b>8</b>	<b>Chapter Conclusion – Perspectives for High Power Q-band PELDOR Using Semi-Rigid Spin Labels .....</b>	<b>115</b>
8.1	C <sup>T</sup> label for Distance Measurements in RNA.....	115
8.2	TOPP Label for Investigation of Peptide Structure in Lipid Bilayers .....	119
	<b>Bibliography .....</b>	<b>123</b>
	<b>Publications .....</b>	<b>139</b>

## List of Abbreviations

bp	<u>B</u> ase <u>p</u> air
DEER	<u>D</u> ouble <u>e</u> lectron <u>e</u> lectron <u>r</u> esonance
DFT	<u>D</u> ensity <u>f</u> unctional <u>t</u> heory
DNA	<u>D</u> eoxyribonucleic <u>a</u> cid
DQC	<u>D</u> ouble <u>q</u> uantum <u>c</u> oherence
EM	<u>E</u> lectron <u>m</u> icroscopy
ENDOR	<u>E</u> lectron <u>n</u> uclear <u>d</u> ouble <u>r</u> esonance
EPR	<u>E</u> lectron <u>p</u> aramagnetic <u>r</u> esonance
ESEEM	<u>E</u> lectron <u>s</u> pin <u>e</u> cho <u>e</u> nvelope <u>m</u> odulation
ESR	<u>E</u> lectron <u>s</u> pin <u>r</u> esonance
FRET	<u>F</u> örster <u>r</u> esonance <u>e</u> nergy <u>t</u> ransfer
HM	<u>H</u> ydrophobic <u>m</u> atch
HMM	<u>H</u> ydrophobic <u>m</u> ismatch
MD	<u>M</u> olecular <u>d</u> ynamics
MLV	<u>M</u> ultilamellar <u>v</u> esicle
mw	<u>M</u> icrowave
nc	<u>N</u> on <u>c</u> oding
NMR	<u>N</u> uclear <u>m</u> agnetic <u>r</u> esonance
nt	<u>N</u> ucleotide
PDB	<u>P</u> rotein <u>d</u> atabank
PDS	<u>P</u> ulsed <u>d</u> ipolar <u>s</u> pectroscopy
PELDOR	<u>P</u> ulsed <u>e</u> lectron <u>d</u> ouble <u>r</u> esonance
PFU	<u>P</u> ulse <u>f</u> orming <u>u</u> nit
RIDME	<u>R</u> elaxation <u>i</u> nduced <u>d</u> ipolar <u>m</u> odulation <u>e</u> nhancement
RNA	<u>R</u> ibonucleic <u>a</u> cid
rt	<u>R</u> oom <u>t</u> emperature
SDSL	<u>S</u> ite <u>d</u> irected <u>s</u> pin <u>l</u> abelling
SIFTER	<u>S</u> ingle <u>f</u> requency <u>t</u> echnique for <u>r</u> efocusing
TM	<u>T</u> ransmembrane
TWT	<u>T</u> ravelling <u>w</u> ave <u>t</u> ube



## List of Figures

Figure 1-1: Magnetic Interactions Probed by EPR spectroscopy .....	3
Figure 1-2: $g$ -Tensor Resolution.....	4
Figure 2-1: Dipole-Dipole-Coupling and Pake Doublet .....	10
Figure 2-2: Single Frequency PDS Techniques .....	12
Figure 2-3: Excitation Profiles of Rectangular vs. Adiabatic Pulses .....	13
Figure 2-4: PELDOR/DEER Sequences.....	14
Figure 2-5: Four-Pulse PELDOR/DEER Experiment .....	16
Figure 2-6: $g$ -Tensor Resolution and Orientation Selection.....	23
Figure 2-7 Orientation Selection in PELDOR .....	24
Figure 2-8: Trace Length vs. Experimental Distance.....	26
Figure 2-9: L-Curve .....	29
Figure 3-1: Strategies for Site-Directed Spin Labelling .....	34
Figure 3-2: Examples for Nitroxide Parent Structures and Steric Groups .....	38
Figure 3-3: Nitroxides for Post-Synthetic Nucleic Acid Labelling .....	41
Figure 3-4: Nitroxides Introduced During Oligonucleotide Synthesis.....	42
Figure 3-5: Nitroxides for Labelling of Amino Acids.....	45
Figure 4-1: Illustration of Possible Reactions to Hydrophobic Mismatch .....	53
Figure 5-1: Simplified Scheme of a Pulsed EPR Spectrometer.....	57
Figure 5-2: Resonator Dip and PELDOR Setup.....	58
Figure 5-3: General Pulse Sequence for PELDOR/DEER Experiments.....	60
Figure 6-1: RNA Sequence and $C^T$ Spin Label .....	61
Figure 6-2: Determination of the RNA Samples' Spin Concentration .....	63
Figure 6-3: <i>Ab Initio</i> Scan of $C^T$ Conformations.....	66
Figure 6-4: Comparison of High and Low Power PELDOR Experiments.....	69
Figure 6-5: Low-Power PELDOR Experiments Performed on Sample 2 .....	70
Figure 6-6: High-Power PELDOR Experiments Performed on Sample 2 .....	72
Figure 6-7: Model of Sample 2 with $C^T$ in Conformation 1 and 2.....	73
Figure 6-8: Low-Power PELDOR Traces Simulated for Sample 2.....	74
Figure 6-9: High-Power PELDOR Traces Simulated for Sample 2.....	75
Figure 6-10: Low-Power PELDOR Traces on Sample 2 Simulation vs. Experiments.....	76
Figure 6-11: High-Power PELDOR Traces on Sample 2 Simulation vs. Experiments.....	77
Figure 6-12: High-Power PELDOR on Samples 1-4 .....	78
Figure 6-13: Experimental PELDOR Traces and Distance Distributions of $C^T$ -Labelled RNA .....	80
Figure 6-14: PELDOR Traces with Longer Evolution Time for Sample 2 and 5 .....	81

Figure 6-15: Experimental Distances vs. Base-Pair Separation .....	83
Figure 6-16: PELDOR Traces of Samples 6 - 8 at Duplex Concentrations of 100 $\mu$ M .....	84
Figure 6-17: Effect of Background Subtraction on the Analysis of Traces Recorded on Sample 1.....	86
Figure 6-18: Effect of Background Subtraction on the Analysis of Traces Recorded on Sample 3.....	87
Figure 6-19: Effect of Background Subtraction on the Analysis of Traces Recorded on Sample 6.....	88
Figure 6-20: Effect of Background Subtraction on the Analysis of Traces Recorded on Sample 7.....	89
Figure 6-21: Model of C <sup>T</sup> -Labelled RNA, Top View .....	91
Figure 6-22: MD Simulations.....	93
Figure 7-1: Spin Labelled WALP24. ....	95
Figure 7-2: Model of WALP24-TOPP for Simulation.....	101
Figure 7-3: Orientation Selection Experiment WALP24-TOPP Series 1 .....	102
Figure 7-4: Orientation Selection Experiment WALP24-TOPP Series 2 .....	103
Figure 7-5: Orientation Selective PELDOR Series 1 Simulation vs. Experiment .....	104
Figure 7-6: Orientation Selection Simulation WALP24-TOPP Series 2 .....	105
Figure 7-7: Comparison of Experiments from Series 1 and Series 2.....	106
Figure 7-8: WALP24-MTSSL vs. WALP24-TOPP in MeOH .....	108
Figure 7-9: Illustration of WALP24, DMPC and POPC.....	109
eFigure 7-10: PELDOR Experiments on WALP24-MTSSL in DMPC for Different Peptide-to-Lipid Ratios .....	110
Figure 7-11: PELDOR Experiment on WALP24-MTSSL vs. WALP24-TOPP in Different Environments .....	111
Figure 8-1: Architecture of the Deoxyribozyme 9DB1 .....	117
Figure 8-2: PELDOR Traces Recorded on 9DB1 .....	118
Figure 8-3: Illustration of Possible Reactions to Hydrophobic Mismatch .....	120
Figure 8-4: Determination of a Helix Tilt Angle in a Membrane .....	121



## 1. Chapter

### Biophysical Methods for Structural Biology

#### – A Place for Electron Paramagnetic Resonance

Elucidation of the molecular structure of biological systems is the cornerstone of understanding their function and dynamics. The most prominent and influential representative of high-resolution structure methods is x-ray diffraction.<sup>1</sup> Since the publication of myoglobin's crystal structure in 1958 more than 100,000 crystal structures have been deposited in the protein databank (PDB).<sup>2,4</sup> In fact,  $\approx 89\%$  of the 120,879 structures held in PDB in July 2016 are based on x-ray crystallography, evidencing the predominance of the technique. However a limitation arises from its need for crystallized biomolecules, in terms of success of crystallization process itself and the meaningfulness of the crystallized state.<sup>5</sup> Second place in this ranking goes to nuclear magnetic resonance (NMR), which essentially delivered all the remaining structures ( $\approx 10\%$ ). NMR experiments can be performed on biomolecules in solution and are therefore able to measure dynamics, making it a powerful complement to x-ray.<sup>6</sup> A drawback of NMR spectroscopy is its limitation to macromolecular complexes smaller than 100 kDa. Recently, cryo-electron microscopy (cryo-EM) is attracting a lot of attention, due to an increasing number of structures with a resolution higher than 4 Å.<sup>7</sup> Though the method is closely chasing a very high ranking in the group of high-resolution structural methods, the majority of structures delivered by cryo-EM still has a resolution below 5 Å. Fluorescence techniques offer a possibility to investigate biological

systems in liquid solution with single molecule sensitivity. Particularly a special application called Förster resonance energy transfer (FRET) which can measure distances between two chromophores (FRET pairs), should be mentioned.<sup>8, 9</sup> The method has been widely used for proteins, nucleic acids and transmembrane segments.<sup>8-10</sup> Adversely, interpretation of the experimental FRET efficiencies requires knowledge about the so-called form factor. This parameter describes the mutual orientation of the two chromophores dipoles and is required for distance determination.

Electron paramagnetic resonance (EPR) spectroscopy has also taken its well-earned place among the pool of biophysical methods for structural biology. The method is a natural choice for studying biomolecules with intrinsic paramagnetic centres. In biology EPR active species can be found as transition metals in active centres or radical intermediates of organic molecules such as quinones, amino- or nucleic acid radicals. On top of this, EPR's restriction to naturally occurring paramagnetic centres was overridden by the development of a technique to insert paramagnetic reporter groups, mostly organic radicals like nitroxides, at user defined sites, well known as site-directed spin labelling (SDSL).<sup>11</sup> Structural information is encoded in the magnetic interactions experienced by the electron spin which are probed by EPR. Most importantly the interaction with the static magnetic field (electron-Zeeman) and surrounding spins of nuclei (hyperfine) or electrons. Continuous wave EPR (cw-EPR) at X-band fields and frequencies (9 GHz/0.34 T) has been employed for decades to investigate paramagnetic species in biological systems. However, the rise of EPR as method for structural biology has been advanced by technical developments in the fields of high field/high frequency and pulse EPR

instrumentation as well as technology enabling double frequency experiments.<sup>12</sup> Figure 1-1 gives an overview of the probed interactions and classifies the frequencies/fields they are best investigated at.

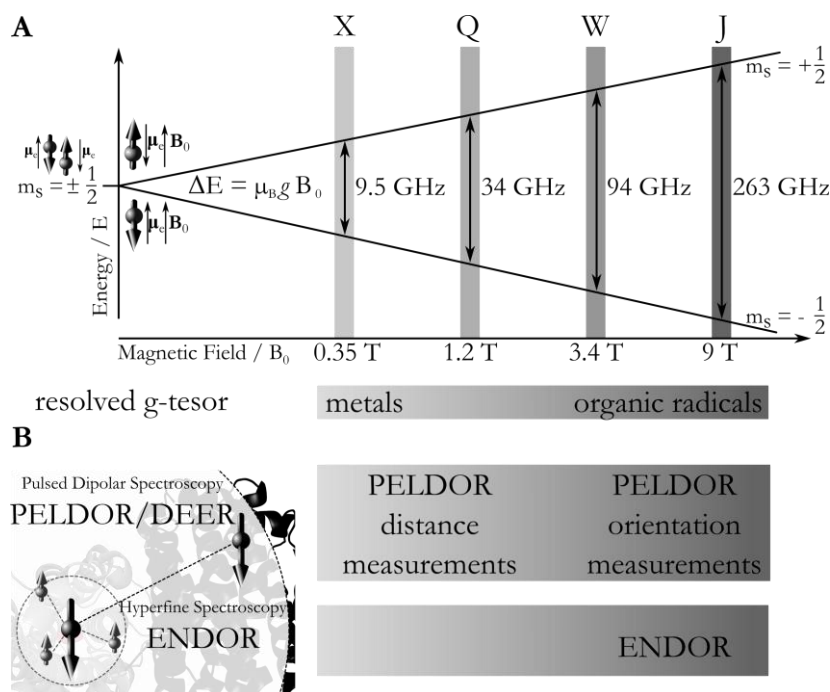


**Figure 1-1: Magnetic Interactions Probed by EPR spectroscopy**

*A: Electron-Zeeman interaction. The interaction of the magnetic moment  $\mu_e$ , arising from the electron's spin, and the external magnetic field  $\mathbf{B}_0$ , causes a splitting of the energy levels of the two  $m_s$  states ( $+\frac{1}{2}$ ,  $-\frac{1}{2}$ ). The energy difference  $\Delta E$  is dependent on the g-value and is scaling with the magnetic field as:  $\Delta E = \mu_B g B_0$ . Characteristic field strengths and microwave frequencies are given for the four EPR bands: X, Q, W and J. The electron-Zeeman is an anisotropic interaction and the resolution of the corresponding  $g$ -tensor is field dependent. Metals display a strong  $g$ -anisotropy, which is resolved already at low fields and frequencies, application of high fields and frequencies is required to resolve the  $g$ -tensor of organic radicals. B: Spin-spin interactions. EPR techniques can probe interactions between the electron spin of a paramagnetic species (large arrow) and the spin of nearby nuclei (small arrows) by hyperfine techniques, like ENDOR. As the interaction between two electron spins is stronger, when compared to nucleus-electron, it can be measured over larger distances by pulsed dipolar spectroscopy, most prominently PELDOR/DEER.*

The electron-Zeeman interaction can be probed by field-sweep EPR experiments, either by pulsed or cw-EPR, revealing the  $g$ -tensor that will give information about the electrostatic environment and the geometry of the paramagnetic species. As the resolution of the  $g$ -tensor scales with the applied field strength (Figure 1-1, A), properties of the system under investigation will determine

which field is best suited. Transition metals give rise to a large anisotropy of the electron-Zeeman interaction, due to strong spin-orbit coupling. The  $g$ -tensor will be therefore resolved at low magnetic fields and microwave frequencies, enabling informative analysis of EPR spectra recorded at X or Q-band frequencies. Organic radicals in contrast show comparatively low anisotropy, making the resolution of their  $g$ -tensor only possible if high fields and frequencies are applied.<sup>13</sup> Figure 1-2 shows the echo-detected field swept EPR spectra of a nitroxide label. While at X-band frequency the shape of the spectrum is dominated by the hyperfine interaction, the  $g$ -tensor is completely resolved at W and J band. Hyperfine techniques, the most contemporary is a technique employing both microwave- and radio-frequencies called electron nuclear double resonance (ENDOR), enable

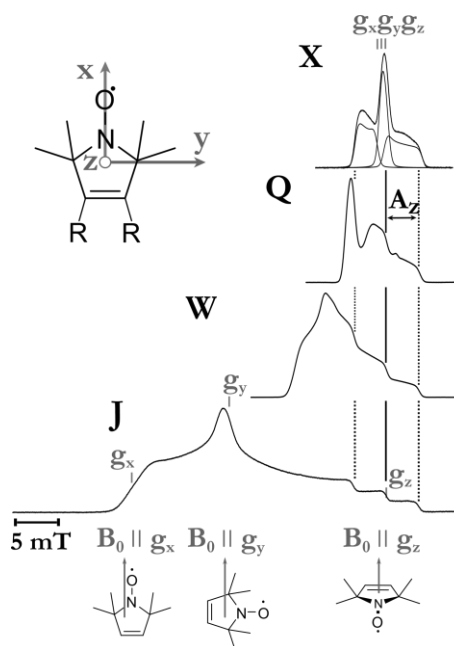


**Figure 1-2:  $g$ -Tensor Resolution**

*Experimental field-sweeps (black lines) of the representative nitroxide spin label  $\zeta m$  (3.3.1) recorded at four different frequencies, illustrating the enhancement of  $g$ -tensor resolution with increasing fields and frequencies. The orientation of  $g$ - and  $A$ -tensor are shown as inset. They are collinear in the nitroxide's molecular frame.*

the investigation of the hyperfine interaction between the electron spin and spins of coupled nuclei as sketched in Figure 1-1, B.<sup>14, 15</sup> The method cannot only report on the number and nature of coupled nuclei, but also on their distance and orientation towards the electron spin. Application of high fields empowers the technique for several reasons. First, analysis of the ENDOR spectra is simplified when the Zeeman interaction is much larger than the probed hyperfine interaction (high-field approximation) and the nuclei are completely quantized along the static magnetic field  $\mathbf{B}_0$ , as in this case hyperfine spectra are symmetric around the nuclear Zeeman frequency. Additionally, orientation selectivity, which is increased at high fields, can be exploited to determine the orientation between the electron and the nuclear spin carrying centre. ENDOR has been applied to elucidate coordination chemistry, structure and biochemical mechanism of metal containing systems as iron-sulfur clusters in proteins or organic radical intermediates.<sup>16-19</sup>

In recent years particular focus, in EPR for structural biology, was set on the determination of long-range distances between two paramagnetic centres with pulsed EPR spectroscopy. The dipolar spin-spin interaction between two electrons is way stronger than the hyperfine interaction (due to the electron's larger gyromagnetic ratio) and is therefore reaching further in space (Figure 1-1, B). The different techniques developed to probe this interaction are called pulsed dipolar spectroscopy (PDS). Pulsed electron double resonance (PELDOR), also called double electron-electron resonance (DEER), is one PDS technique that enables the detection of the weak dipole-dipole interaction between two paramagnetic centres in the range of 1.5 – 10 nm.<sup>20-22</sup> The experiment can be performed in solution (frozen) and does not suffer from a molecular size limitation as its relatives from NMR, making it a powerful

method for delivering long-range distance constrains. Noteworthy, distance extraction is more straightforward than for its fluorescence counterpart FRET, as parameters like the form factor are not necessarily required for distance measurements if these are performed in the absence of orientation effects at low fields and frequencies (X and Q band). However, at higher magnetic fields and microwave frequencies, increased resolution of the  $g$ -tensor will introduce orientation selection effects that can complicate the data analysis for distance measurements. At W and J-band frequencies orientation selection effects are enhanced to a degree where they enable determining the mutual orientation of the two paramagnetic centres (§ 2.2.2). This work focuses on exploring the performance of PELDOR/DEER distance measurements between nitroxide spin labels at Q-band fields and frequencies in two representative biological systems posing particular challenges in structural biology, transmembrane helices and ribonucleic acids.

## 2. Chapter

### Introduction and Theory of EPR Distance

#### Measurements

In this chapter an introduction to state of the art EPR-based distance measurements will be provided. Particular focus will be set on the theoretical background of the PELDOR/DEER technique. It will be shown, how structural parameters of biomolecules, like distance and orientation between residues and aggregation states, are encoded in the experimental data.

#### 2.1 Concept of EPR Distance Measurements

The interaction probed in all EPR distance measurements is the dipole-dipole interaction between two magnetic moments  $\vec{\mu}_A$  and  $\vec{\mu}_B$ , that are associated with two spins, and its dependence on the distance between them. While NMR probes the dipole-dipole interaction between two nuclear spins, EPR investigates the interaction between either nuclear and electron spins (hyperfine spectroscopy) or between two electron spins, the latter is the strongest among these examples and therefore enables long-range distance measurements.

##### 2.1.1 Electron Spin-Spin Dipolar Coupling

The interaction energy  $E$  between two magnetic moments  $\vec{\mu}_A$  and  $\vec{\mu}_B$ , connected through space via a distance vector  $\vec{r}_{AB}$ , can be classically

described as shown by equation (1), with  $\mu_0$  being the vacuum permeability.

$$E = \frac{\mu_0}{4\pi} \left( \frac{\vec{\mu}_A \cdot \vec{\mu}_B}{r_{AB}^3} - \frac{3(\vec{\mu}_A \cdot \vec{r}_{AB})(\vec{\mu}_B \cdot \vec{r}_{AB})}{r_{AB}^5} \right) \quad (1)$$

The magnetic moment of an electron can be described with the spin operator vector  $\vec{S} = \hat{S}_x, \hat{S}_y, \hat{S}_z$  and the gyromagnetic ratio  $\gamma_e$  (equation (2)), that can be written as in equation (3), with  $\mu_B$  as the Bohr magneton, the  $g$ -factor of an electron  $g_e$  and the reduced Planck constant  $\hbar$ , or as the ratio of its elementary charge  $e$  and mass  $m_e$ .

$$\vec{\mu} = \gamma_e \vec{S} \quad (2)$$

$$\gamma_e = \frac{\mu_B g_e}{\hbar} = \frac{e}{2m_e} g_e \quad (3)$$

The classical expression (equation (1)) can now be written as a Hamiltonian  $\hat{\mathcal{H}}_{dd}$  describing the dipolar interaction (4).

$$\hat{\mathcal{H}}_{dd} = \frac{\mu_0 \mu_B^2 g_A g_B}{4\pi \hbar} \frac{1}{r^3} (A + B + C + D + E + F) \quad (4)$$

$g_A$  and  $g_B$  are the  $g$ -values of the coupled paramagnetic centres A and B. The terms  $A-F$  in equation (4) are products of spin operators, (spherical coordinates:  $\vec{r}_{AB} = (r \cdot \sin \theta \cdot \cos \phi, r \cdot \sin \theta \cdot \sin \phi, r \cdot \cos \theta)$  angular variables  $\theta, \phi$ ), to describe the orientation between  $\vec{r}_{AB}$  and the magnetic field as sketched in Figure 2-1 (left).



$$\begin{aligned}
A &= \hat{S}_z^A \hat{S}_z^B (3 \cos^2 \theta - 1) \\
B &= -\frac{1}{4} (\hat{S}_+^A \hat{S}_-^B + \hat{S}_-^A \hat{S}_+^B) (3 \cos^2 \theta - 1) \\
C &= -\frac{3}{2} (\hat{S}_+^A \hat{S}_z^B + \hat{S}_z^A \hat{S}_+^B) \sin \theta \cdot \cos \theta \cdot e^{-i\phi} \\
D &= -\frac{3}{2} (\hat{S}_-^A \hat{S}_z^B + \hat{S}_z^A \hat{S}_-^B) \sin \theta \cdot \cos \theta \cdot e^{i\phi} \\
E &= -\frac{3}{4} \hat{S}_+^A \hat{S}_+^B \sin^2 \theta \cdot e^{-2i\phi} \\
F &= -\frac{3}{4} \hat{S}_-^A \hat{S}_-^B \sin^2 \theta \cdot e^{2i\phi}
\end{aligned} \tag{5}$$

The direction of the static magnetic field defines the z-axis of the laboratory frame (depicted in Figure 2-1). If the dipolar coupling is small when compared to electron Zeeman splitting the dipolar splitting is determined mainly by the secular term  $\mathcal{A}$  from equation (5), and the dipolar frequency  $\omega_{\text{dd}}$  can be written as:

$$\omega_{\text{dd}} \approx \frac{\mu_0 \mu_B^2 g_A g_B}{4\pi \hbar} \frac{1}{r^3} (3 \cos^2 \theta - 1) \tag{6}$$

Note that in equation (6)  $\omega_{\text{dd}}$  is an angular frequency (rad/s). The frequency in Hertz is given by  $\nu_{\text{dd}} = \omega_{\text{dd}}/2\pi$ . With  $\mu_0 = 1.26 \cdot 10^6 \text{ T}^2 \text{m}^3 \text{s}^{-1}$ ,  $\mu_B = 9.247 \cdot 10^{-24} \text{ JT}^{-1}$ ,  $\hbar = 1.055 \cdot 10^{-24} \text{ Js}$  and the g-values given as  $g_A = g_B = 2$ , the dipolar frequency can be written as:

$$\nu_{\text{dd}} = \frac{\omega_{\text{dd}}}{2\pi} = 52.18 \text{ MHz} \cdot \text{nm}^3 \frac{1}{r^3} (3 \cos^2 \theta - 1) \tag{7}$$

The distribution of the dipolar frequency in a powder sample gives rise to a characteristic spectrum the so-called Pake pattern (or Pake doublet) as displayed in Figure 2-1 (right). There are three significant features to be discussed in terms of the dipolar frequency's angular dependence. First, at an angle of  $\theta = 54.7^\circ$  (magic angle) the dipolar interaction vanishes. In solution the dipolar frequency is averaged out to zero, if molecules rotate fast compared to coupling strength. In frozen solution however, the full Pake pattern will be observed as each doubly labelled macromolecule contributes to the spectrum with its own resonance frequency.

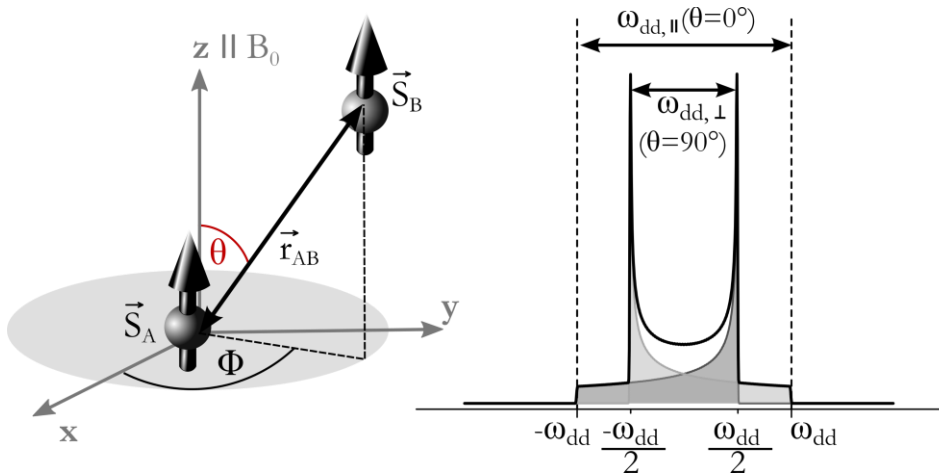


**Figure 2-1: Dipole-Dipole-Coupling and Pake Doublet**

*Left: A pair of spins ( $\vec{S}_A$  and  $\vec{S}_B$ ) coupled by dipole-dipole-interaction via  $\vec{r}_{AB}$ . The orientation of  $\vec{r}_{AB}$  in the laboratory frame (direction of the external magnetic field  $B_0$ ) is defined by the Euler angles  $\theta, \phi$ . Right: Pake doublet, which displays the distribution of the dipolar frequency  $\omega_{dd}$  in a powder sample. Two singularities are visible for  $\vec{r}_{AB}$  perpendicular  $\omega_{dd,\perp}(\theta=90^\circ)$  and parallel  $\omega_{dd,\parallel}(\theta=0^\circ) = 2\omega_{dd,\perp}$  to  $B_0$ .*

The splitting between the two maxima of the spectrum represents the dipolar frequency corresponding to a perpendicular orientation of the

inter-spin vector  $\vec{r}_{AB}$  towards the magnetic field  $\omega_{dd,\perp}$  ( $\theta = 90^\circ$ ). According to equation (7) the inter-spin distance can be calculated from this splitting as

$$r [nm] = \sqrt[3]{\frac{52.18}{\nu_{dd}}} = \sqrt[3]{\frac{2\pi \cdot 52.18}{\omega_{dd}}} \quad (8)$$

For an alignment of  $\vec{r}_{AB}$  parallel to the static magnetic field the dipolar splitting is twice as large as for the perpendicular case. The edge-to-edge distance in the Pake pattern represents  $\omega_{dd,\parallel}$  ( $\theta=0^\circ$ ) =  $2\omega_{dd,\perp}$ .

### 2.1.2 EPR Techniques to Probe the Dipolar Coupling

If the dipolar coupling is sufficiently large to broaden an EPR line beyond its intrinsic line width it can be measured by continuous wave (cw)-EPR. Either directly, if  $\omega_{dd}$  is larger than the line width of at least one of the paramagnetic centres involved, and the splitting into two lines can be extracted from the spectrum.<sup>23</sup> Or, in case of smaller couplings, by deconvolution of the EPR line into the different contributions to the observed line width, like for example relaxation. However, in this case calibration is required.<sup>24</sup> The intrinsic line width of the EPR resonance depends on the species under investigation and the applied magnetic field strength. For nitroxides at X-band fields and frequencies (0.35 T/9 GHz) the method is applicable for distances 0.8 to 2.5 nm<sup>25, 26</sup>, observation of smaller couplings is prevented by the nitroxide's intrinsic line width. The accessible range for cw-EPR can be extended if species with narrow intrinsic line width are used and high fields are applied. A maximum distance of 3.8 nm has been suggested for gadolinium-based

labels at high fields.<sup>27</sup> Distances exceeding this range can be measured pulse EPR spectroscopy. Although pulsed experiments are usually performed at low temperatures, where the spectrum is even more broadened when compared to those recorded at room temperature, small dipolar couplings can be recovered by refocusing inhomogeneous broadening. Figure 2-2 displays a selection of single frequency sequences introduced in this chapter.<sup>20, 21</sup>

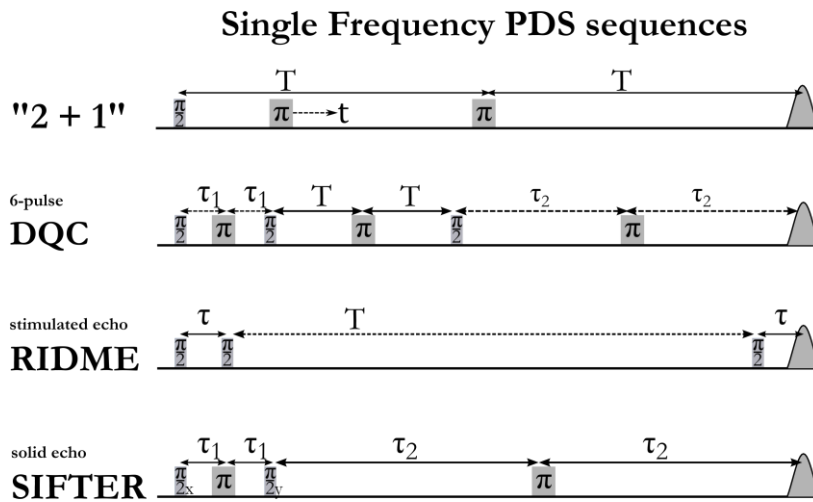


**Figure 2-2: Single Frequency PDS Techniques**

*Single frequency techniques for probing the dipolar interaction, displayed with rectangular pulses. Adiabatic pulses generated by an arbitrary waveform generator (AWG), which became recently commercially available offer a great advantage over rectangular pulses in terms of excitation profile (compare Figure 2-3).*

Single microwave frequency techniques include the “2+1”-sequence<sup>28</sup>, double quantum coherence (DQC)<sup>29-31</sup> and single frequency technique for refocusing (SIFTER).<sup>32</sup> In the last years a lot of attention has been drawn to a technique called relaxation induced dipolar modulation enhancement (RIDME).<sup>33-37</sup> It should be noted that for simplicity all pulses are displayed as rectangular pulses. However, recently the

possibility to create shaped pulses using commercially available arbitrary waveform generators (AWG) became a focus in EPR research. Drastic enhancement of sensitivity could be shown for pulsed EPR techniques including distance measurements.<sup>38-47</sup> While rectangular pulses result in an excitation profile represented by a sinc-function, adiabatic pulses cause broadband inversion of the magnetization as shown in Figure 2-3 (adapted from ref <sup>45</sup>).

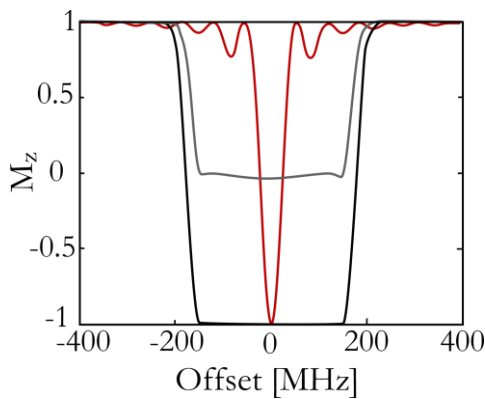


**Figure 2-3: Excitation Profiles of Rectangular vs. Adiabatic Pulses**

*This figure is adapted from reference<sup>45</sup> in which SCHÖPS et al. simulated the profile of magnetization along quantized along  $z/B_0$  ( $M_z$ ) for an adiabatic inversion (black), a broadband  $\pi/2$  (grey) and a rectangular  $\pi$ -pulse of 16 ns length (red).*

The most widely applied PDS technique is the dual microwave frequency technique pulsed electron double resonance (PELDOR), also called double electron-electron resonance (DEER) using four pulses. After introducing the underlying concepts of the PELDOR/DEER experiment, the method will be compared to the single frequency techniques in § 2.2.4.

## 2.2 Pulsed Electron Double Resonance (PELDOR)

PELDOR/DEER was pioneered by MILOV *et al.* in the 1980's as a three-pulse sequence to probe inter spin distances.<sup>48</sup> As shown in Figure 2-4, a Hahn echo sequence with a long evolution time  $T$  between  $\pi$ - and  $\pi/2$ -pulses is used to monitor a spin echo at one microwave frequency  $\nu_A$ .

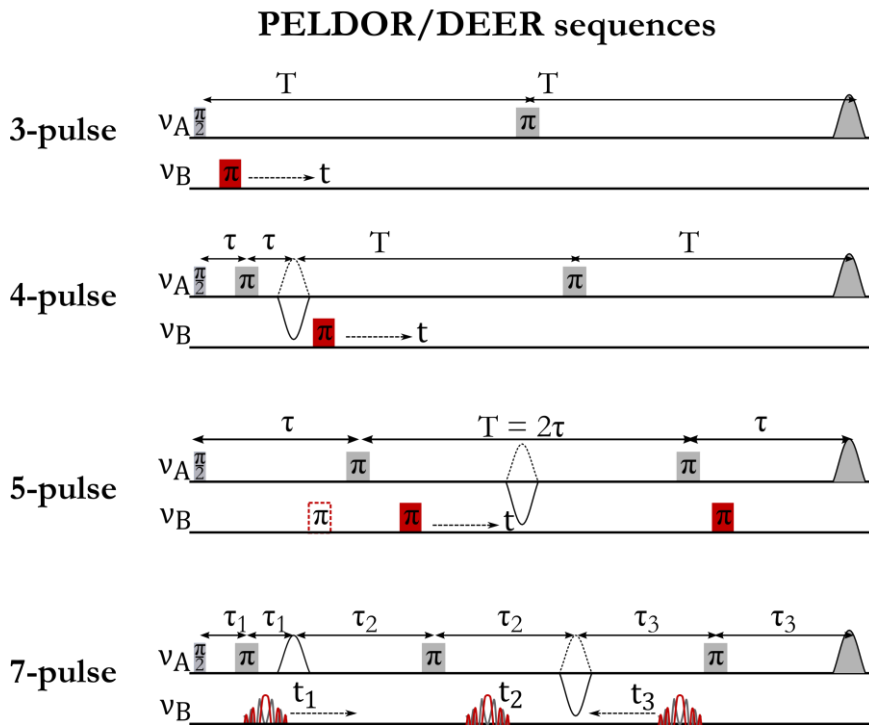


Figure 2-4: PELDOR/DEER Sequences

PELDOR/DEER sequences that have been proposed in literature. The most widely applied is the dead time free four-pulse sequence. Sequences including five or seven pulses have been proposed to increase the sensitivity of the experiment. The 7-pulse sequence relies on the application of adiabatic pulses at the pumping frequency  $\nu_B$  and cannot be realized with rectangular pulses as stated by the authors.

A  $\pi$ -pulse at a second microwave frequency  $\nu_B$  is applied to flip spins with a different resonance frequency, to probe the dipolar interaction between spins A and B, excited by  $\nu_A$  and  $\nu_B$ , as described below. This originally introduced sequence suffered from a dead time, as the  $\pi$ -pulse at  $\nu_B$  cannot be applied at zero time, which is the position of the  $\pi/2$ -pulse at  $\nu_A$ . To overcome this issue an additional pulse was introduced by MARTIN *et al.* to shift the zero-time of the experiment to the position of an echo rather than a pulse.<sup>49, 50</sup> Meanwhile different sequences consisting of five or seven pulses have been proposed to increase the sensitivity of the experiment.<sup>39, 47</sup> It is noteworthy that the use of shaped pulses at the pumping frequency  $\nu_B$  has been shown to increase the intensity of the PELDOR signal, in case of the seven-pulse PELDOR version pulse shaping is even mandatory. However, attention has to be drawn to the fact that currently the use of AWG comes with the price of coherence of the pulses applied at both frequencies. Additional coherence transfer pathways generate unwanted spin echoes, creating distortions in the recorded time trace.<sup>51</sup>

Among the PDS techniques introduced above, the four-pulse PELDOR/DEER is the most routinely used EPR-experiment to measure long-range distances in many applications.<sup>20, 21, 52</sup>

### 2.2.1 The Four-Pulse PELDOR/DEER Experiment

EPR distance measurements are typically performed on powder-like samples, usually frozen solution, hence molecules are statistically orientated with respect to the magnetic field. Since hyperfine and Zeeman interaction are anisotropic, each spin-carrying molecule will

contribute to the EPR line with its own resonance frequency leading to inhomogeneous broadening of the EPR line. The use of two microwave frequencies therefore enables separate excitation of the two coupled spins. Figure 2-5 illustrates the concept of the experiment.

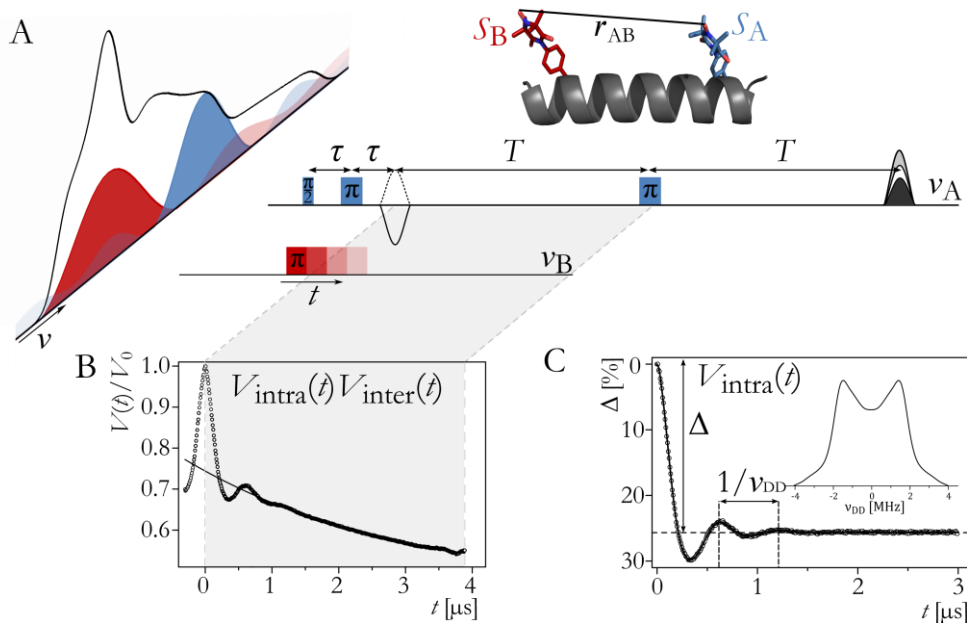


**Figure 2-5: Four-Pulse PELDOR/DEER Experiment**

*A: Echo detected field-sweep (left) of the TOPP labelled WALP24 (inset) as representative nitroxide spectrum and four-pulse PELDOR sequence with typical excitation conditions. A single  $\pi$ -pulse is applied, at the frequency  $\nu_B$  for exciting B-spins, to the maximum of the EPR line (red). The frequency for detection (blue) is set to a lower frequency (in this example 90 MHz). The signal of the detected echo  $V(t)$  is oscillating as a function of the position  $t$  of the pump-pulse. The experimental time trace (B) includes the oscillation arising from the dipolar interaction of A- and B-spins ( $V(t)_{intra}$ ) and a decay arising from intermolecular spin-spin-interactions  $V(t)_{inter}$ . After background correction only the intramolecular contribution is obtained (C). It reflects the dipolar frequency  $\nu_{dd}$  ( $\omega_{dd}/2\pi$ ) and its angular and distance dependence. Fourier transformation of the time trace results in the Pake pattern (C, inset) as described in chapter 2.1.1.*

One microwave frequency  $\nu_A$  is used to detect one of the partners, called A-spins. The sequence used for detection consists of a Hahn-echo



sequence followed by an evolution time  $T$  during which the A-spins precess in the transversal plane until they are refocused with a  $\pi$ -pulse. The intensity of the echo refocused by this last pulse is monitored in the PELDOR/DEER experiment. Note that during the evolution time  $T$ , the amount of magnetization, arising from the A-spins, that is refocusable by the third detection-pulse, will decrease due to relaxation. The maximum evolution time applicable in the experiments will therefore depend predominantly on the relaxation time  $T_m$  of the respective system. B-spins are excited with a selective  $\pi$ -pulse at a second microwave frequency  $\nu_B$ . This stimulated flip of B-spins will suddenly alter the Larmor-frequency of the A-spins by the dipolar frequency. The change in precession frequency of the A-spins will lead to a different amount of spin packages refocused with the third pulse of the detection sequence. As the position  $t$  of the pump-pulse is varied in time over the evolution time  $T$ , the detected echo intensity  $V(t)$  will oscillate according to the dipolar frequency. It is important to note here that the two microwave frequencies are not phase coherent and that the separation between them has to be large enough to avoid overlapping of their excitation bandwidth. This condition reduces artefacts from nuclear modulation effects (electron-spin-echo envelope modulation (ESEEM)).<sup>53</sup> In case any residue ESEEM modulation is observed, it can be strongly reduced by averaging several experiments using different  $\tau$  values, as the ESEEM, in contrast to the dipolar oscillation, is  $\tau$  dependent. Additionally, incoherence of the pulses applied at the two frequencies suppresses artefacts arising from echoes that are created by the pump pulse and the observer pulses. These echoes will appear at time points varying with the position of the pump pulse and will cause

large distortions in the recorded time trace.<sup>51</sup> The resulting experimental PELDOR/DEER signal has two contributions. A background arising from intermolecular spin-spin interactions called  $V_{\text{inter}}(t)$ , and the desired signal originating from intramolecular interactions of A- and B-spins  $V_{\text{intra}}(t)$ .

$$V(t) = V_{\text{intra}}(t) V_{\text{inter}}(t) \quad (9)$$

The four pulse PELDOR/DEER signal arising from an isolated spin pair can be described by essentially the same expression as for the three pulse version.<sup>21, 50, 54, 55</sup>

$$V_{\text{intra}}(t) = V_0(1 - \lambda + \lambda \langle \cos(\omega_{\text{dd}}(r, \theta)t) \rangle_{r, \theta}) \quad (10)$$

Despite the term describing the dipolar interaction, equation (10) includes two amplitude factors  $V_0$  and  $\lambda$ .  $V_0$  is the initial signal intensity of the detected echo at zero-time ( $t = 0$ ) and mainly depends on the excitation achieved by the detection pulses at  $\nu_A$  and the evolution times  $\tau$  and  $T$  (Figure 2-5, A) as follows: The amount  $\langle \hat{S}_z \rangle$  available in the experiment is determined by the spin concentration of the sample and the polarization created by the experimental conditions (field strength and temperature). The effect of the applied pulses can be described by the probability  $p$  to flip a spin with a resonance-offset  $\Delta\omega$  from the frequency of the pulse. Equation (11) gives  $p$  for a pulse of a nominal flip angle  $a$  and microwave field strength  $\mathbf{B}_1$ .<sup>21</sup>

$$\begin{aligned}
p &= \sin^2(\alpha u/2)/u^2 \\
u^2 &= 1 + \frac{\Delta\omega^2}{\omega_{mw}^2} \\
\omega_{mw} &= \gamma_e \mathbf{B}_1
\end{aligned} \tag{11}$$

Additionally the signal decay due to relaxation in the transversal plane (phase memory time  $T_m$ ) during the time  $2(\tau + T)$  has to be taken into account. In the easiest case the decay can be described by an exponential decay (general form:  $V(t) = V_0 \exp(-(2t/T_m))$ ). The amplitude  $\lambda$  is called modulation depth parameter and describes the fraction, of spin pairs contributing to the signal, meaning the fraction of B-spins flipped by the pump pulse at  $\nu_B$  that are coupled to A-spins. The probability of flipping a spin with the pump-pulse follows equation (11). Additionally  $\lambda$  will depend on the labelling efficiency of the macromolecule. The contribution of spin pairs not affected by the pulse applied at  $\nu_B$ , meaning A-spins are detected but corresponding B-spins are not flipped by the pump-pulse, are encoded in equation (10),  $V_0(1 - \lambda)$ . The experimentally observed modulation depth, which is dependent on conditions such as pulse length (excitation bandwidth) is denoted  $\Delta$  in this work. Angular brackets denote averaging of  $\omega_{dd}$  over all distances  $r$  and orientations  $\theta$ . It is important to note that equation (10) holds only in the absence of spectral overlap of the excitation profiles of the pulses applied at  $\nu_A$  and  $\nu_B$ . If this condition is not fulfilled additional coherence pathways are opened and further terms contribute to the PELDOR/DEER signal, corresponding to overall eight different dipolar signals (number of possible pathways for an N-pulse sequence =  $2^{N-1}$ ). A detailed description can be found in reference<sup>2f</sup>. The intermolecular contribution is a decaying signal arising from the dipolar interaction of a spin  $i$  with all surrounding spins  $j$  and can be written as a product:

$$V_{\text{inter}}(t) = \left\langle \prod_{j \neq i}^{N-1} [1 - \lambda_{ij}(1 - \cos(\omega_{dd}(r_{ij}\theta_{ij})t))] \right\rangle \quad (12)$$

So far only the case of an isolated pair of spins has been discussed. In structural biology however, the studied object can also be a multi-spin system. Proteins may have an active state that is represented by an oligomer, membrane embedded peptides or proteins may aggregate. The PELDOR/DEER signal arising from intramolecular dipole-dipole coupling will take a more complex form than in equation (10) in this case, the sum of the products of the individual two spin interactions. For a system having  $k=1, \dots, N$  spins,  $V_{\text{intra}}(t)$  takes the form of:<sup>20, 21</sup>

$$V_{\text{intra}}(t) = V_0 N^{-1} \left\langle \sum_{i=1}^N \prod_{k \neq i} [1 - \lambda_{ik}(\cos(\omega_{dd}(r_{ik}, \theta_{ik})t))] \right\rangle_{r_{ik}} \quad (13)$$

Equation (13) is the sum of the products of the dipolar signals arising from detection on spin  $i$ , when pumping on the partner spin  $k$ . This dependence offers a possibility to extract the number of spins coupled in a biomolecular ensemble, as already suggested by MILOV *et al.* and applied to study the self-assembly of peptides in glassy solutions.<sup>48, 54, 56</sup> BODE *et al.* used synthetic polyradicals of defined geometry to systematically investigate multi-spin systems. They claim that the error in the number of spins extracted from a PELDOR experiment can be as low as 5 %.<sup>57</sup>

### 2.2.2 Orientation Selection in PELDOR

Chapter 2.2.1 described the PELDOR experiment for the case of flexible labels, lacking geometrical correlation between the two magnetic

moments. If rigid paramagnetic centres are investigated by PELDOR spectroscopy an additional effect will contribute to the experiment. As the dipolar coupling is an anisotropic interaction, the resulting frequency distribution will also depend on geometry of the observed system (called orientation selective PELDOR), as already discussed by LARSEN and SINGEL in 1993.<sup>58</sup> Even if rigid labels are used, orientation selection may or may not be observed depending on the experimental setup, i.e. experimental field and microwave frequency and excitation conditions (available microwave power). It can be considered as an artefact as it strongly aggravates accurate distance determination. On the other hand, it can be exploited for investigating the mutual orientation of two spin labels with orientation selective PELDOR/DEER. Examples of such studies are natural occurring radicals or rigid labels in proteins and nucleic acids.<sup>59-62</sup> To understand orientation selection, the EPR line of a nitroxide in frozen solution has to be described, as it is dominated by anisotropic contributions. If, for simplicity, only Zeeman and hyperfine interaction to one coupled nitrogen nucleus are considered the Hamiltonian has three contributions: the electron-Zeeman  $\mathcal{H}_{\text{EZ}}$ , the nuclear-Zeeman  $\mathcal{H}_{\text{NZ}}$  and the hyperfine interaction between the unpaired electron and the nucleus  $\mathcal{H}_{\text{HF}}$ .

$$\begin{aligned}\mathcal{H} &= \mathcal{H}_{\text{EZ}} + \mathcal{H}_{\text{NZ}} + \mathcal{H}_{\text{HF}} \\ &= \mu_B \cdot \mathbf{S} \cdot \mathbf{g} \cdot \mathbf{B} + \mu_N g_N \mathbf{I} \cdot \mathbf{B} + \mathbf{I} \cdot \mathbf{A} \cdot \mathbf{S}\end{aligned}\tag{14}$$

The nuclear-Zeeman term is described with the nuclear magneton  $\mu_N$ , the nuclear  $\mathbf{g}$ -factor  $g_N$  and the nuclear spin vector operator  $\mathbf{I}$ , and can be neglected at this point. Anisotropy of the electrons Zeeman interaction is reflected in the  $\mathbf{g}$ -matrix ( $\mathbf{g}$ -tensor with principal axis

values  $g_1, g_2, g_3$  also  $g_x, g_y, g_z$ ). The hyperfine coupling between electron and nuclear spin has an isotropic ( $a_{iso}$ ) and an anisotropic ( $\mathbf{T}$ ) contribution,  $\mathbf{A} = a_{iso} + \mathbf{T}$ . In analogy to the  $\mathbf{g}$ -tensor, the principal axis values of the  $\mathbf{A}$ -tensor are called  $A_1, A_2$  and  $A_3$  (also  $A_x, A_y, A_z$ ). Each resonance position in the EPR spectrum reflects a defined orientation of the two tensors with respect to the external magnetic field. In a nitroxide label  $\mathbf{A}$ - and  $\mathbf{g}$ -tensors are collinear and connected to the molecular frame as depicted in Figure 2-6, inset. Due to the  $\mathbf{g}$ -tensors anisotropy, the largest Zeeman splitting is observed when  $\mathbf{B}$  is aligned along the N-O axis of the molecule ( $g_x, A_x$ ), the smallest when  $\mathbf{B}$  is perpendicular to the ring-plane ( $g_z, A_z$ ).  $g_y$  and  $A_y$  are perpendicular to these two directions. Application of pulses with a bandwidth smaller than the overall spectrum will now lead to excitation of only a certain fraction of nitroxide molecules, depending on their orientation with respect to the magnetic field, this is called orientation selection. The resolution of orientation selectivity strongly depends on the applied magnetic field strength. The effect is illustrated in Figure 2-6 displaying the echo detected field-sweeps of a doubly  $^{15}\text{N}$  labelled RNA (compare chapter 3.3.1). At low fields and frequencies (X band, 0.35 T/9 GHz) the EPR line is dominated by A-anisotropy of the two hyperfine lines ( $m_I = -1$  and  $m_I = +1$ ). Orientation selection can only be achieved via hyperfine anisotropy if soft pulses are used. As the resolution of the  $\mathbf{g}$ -tensor increases with increasing field strength, the EPR spectrum is dominated by g-anisotropy at high fields and frequencies (3.4 T/94 GHz, 9 T/263 GHz), leading to increased orientation selectivity. Q band (34 GHz/1.2 T) is an intermediate frequency where g- and A-anisotropy are comparable in their amplitude. According to equation (6) the g-values selected for pumping and detection will have an impact on the  $\omega_{dd}$

observed in the experiment, if the mutual configuration of the labels is fixed or displays only limited variation.

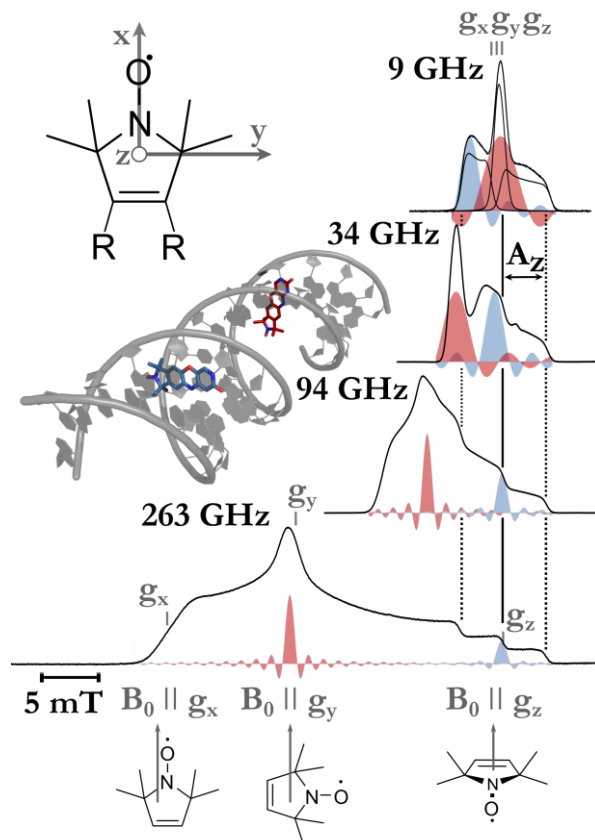
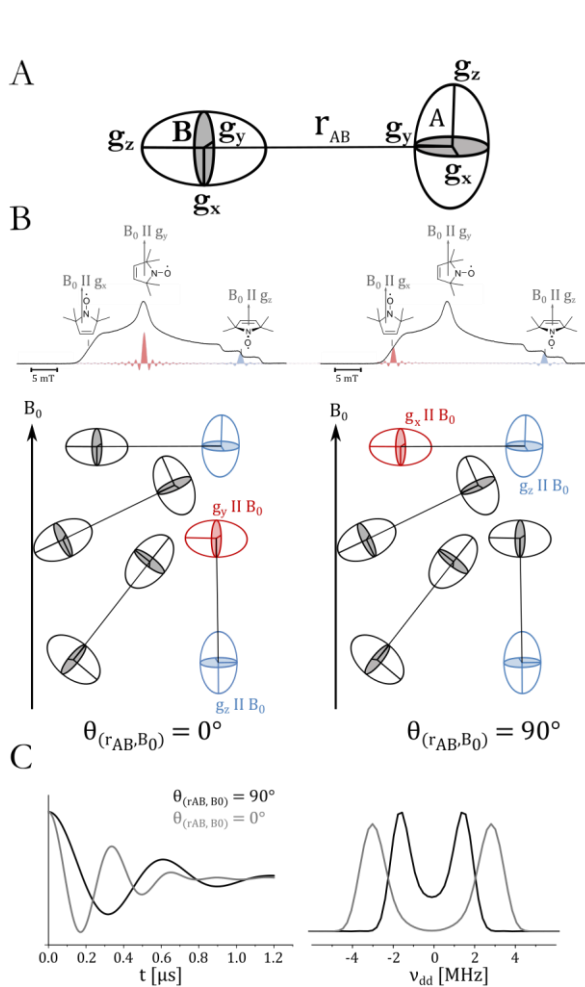


Figure 2-6: *g*-Tensor Resolution and Orientation Selection

Experimental field-sweeps (black lines) of a representative nitroxide spin label **Çm** (3.3.1) recorded at four different frequencies illustrating the enhancement of *g*-tensor resolution with increasing fields and frequencies. The spin label (shown in blue and red) was attached to a 20 base-pair duplex RNA as illustrated in the Pymol model, of a standard A-form RNA structure (shown in grey). The orientation of *g*- and *A*-tensor, which are collinear in the nitroxide, are shown as inset. Blue and red lines in the experimental ESE spectra show typical excitation profiles of the pulses used for pumping (red) and detection (blue) in a PELDOR/DEER experiment. While at 9 GHz/0.35 T all orientations of the nitroxide towards the external magnetic field are excited, at 263 GHz/9 T only a fraction of the nitroxide's orientations is excited. Both detection and pumping pulses become orientation selective.

However this effect is rather small in nitroxide labels. More importantly, the selection of nitroxide orientations will ultimately lead to a selection

of biomolecules and orientations of the interconnecting vector  $r_{AB}$ , as depicted in Figure 2-7. Orientation selection of the detected molecules will lead to a non-random choice of detected spin pairs. In the example of Figure 2-7, only molecules where one of the partners has its  $g$ -tensor  $z$ -Axis oriented parallel to the magnetic field, depicted in blue, are detected.



**Figure 2-7 Orientation Selection in PELDOR**

*A: A pair of spin labels A and B, represented by their  $g$ -tensor, with rigid connection to the inter-spin vector  $r_{AB}$ . B: Setup for a PELDOR/DEER experiment with  $\nu_A$  (blue) applied at  $g_x$ . If  $\nu_B$  is applied at  $g_y$  only molecules with the interconnecting vector parallel to the external magnetic field will be probed (left). If  $\nu_B$  is applied at  $g_x$ , only spin pairs with  $r_{AB}$  perpendicular to the static magnetic field will contribute to the dipolar oscillation. (right) C: The frequency distribution observed in the time traces and their Fourier transformation, will not display a full frequency distributions as shown in Figure 2-1, but will reflect the orientation of  $r_{AB}$  towards the external magnetic field with  $\nu_{dd}(\theta=0^\circ) = 2 \nu_{dd}(\theta=90^\circ)$ .*

On the left of Figure 2-7, B,  $\nu_B$  is chosen to excite only nitroxide molecules having their  $g_y$ -axis parallel to the magnetic field (red), the spin pair probed by this setup has its inter-spin vector aligned parallel to the



static magnetic field. While if  $\nu_B$  excites nitroxide molecules with  $g_x$  parallel to the magnetic field, the spin pair's inter-spin vector is perpendicular to the field (Figure 2-7, B, right). According to the angular dependence of the dipolar interaction (§ 2.1.1), the dipolar frequency observed for  $\vec{r}_{AB} \parallel \vec{B}_0$  will be  $2\nu_{dd}$  (Figure 2-7, C). These are the two limiting cases, all intermediate situations can be observed in the experiment. Additionally, spin pairs can only contribute to the dipolar oscillation if the spectral position  $\nu_B$  is applied at a spectral position that corresponds to the orientation of the coupled B-spin (also the observed modulation depth becomes a function of the experimental setup). The conversion of time traces affected by orientation into distances is ambiguous, if the relative orientation of the two labels is unknown. To avoid orientation selection artefacts hard pulses that cover a large part of the EPR spectrum are required when paramagnetic centres with reduced mobility are probed. However, at high fields and frequencies orientation selective experiments can be used to investigate the mutual orientation of two rigid paramagnetic centres, with increasing resolution.<sup>63</sup>

### 2.2.3 Analysis of Experimental Data

The extraction of distance distributions  $P(r)$  is performed by fitting of the intramolecular  $V_{intra}(t)$  (chapter 2.2.1) part of the experimental time trace after removal of  $V_{inter}(t)$ . The program used for analysis in this work is the well-known DEERanalysis developed by JESCHKE *et al.*<sup>64</sup> The accuracy of the extracted distances will depend on the quality of the experimental data. Therefore experimental conditions will have a major impact on the accessible distance range and reliability of the data analysis. The setup has to be chosen in a way to best suppress artefacts

like orientation selection or ESEEM as discussed earlier. The choice of the evolution time  $T$ , and therefore the trace length, will determine the accessible distance range, as the modulation period is increasing with decreasing dipolar frequency. According to equation (7) the perpendicular frequency  $\nu_{dd,\perp}(\theta = 90^\circ)$  can be calculated for a given distance  $r$ . For precise distance determination at least 1.5 modulations should be observed. The trace length required to match this condition is

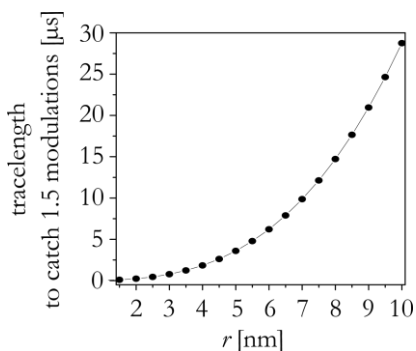


**Figure 2-8: Trace Length vs. Experimental Distance**

*Trace length required to observe 1.5 full modulations of a given distance, calculated using the relation (§ 2.1.1):  $\nu_{dd,\perp} [\text{MHz}] \approx 52.18/r^3$ . One full modulation is observed at the time  $t = 1/\nu_{dd,\perp}$ .*

plotted in Figure 2-8. With this consideration it can be estimated that for a distance of 8 nm, a traces length of 15  $\mu\text{s}$  is required, while for 10 nm already an evolution time  $T$  (time between the first Hahn echo and the third detection pulse, Figure 2-5) of around 30  $\mu\text{s}$  would be necessary to fulfil this criterion. With increasing trace length the detected signal will decrease strongly compromising the signal-to-noise ratio. Increasing the phase memory time  $T_m$  therefore is one key to good data quality. Usually

PELDOR/DEER experiments using nitroxide spin labels are performed at 50 K where the relaxation is already slowed down to several  $\mu\text{s}$ , due to decreased mobility of substituents (usually methyl groups in spin labels) in close proximity to the radical function, but the longitudinal relaxation time is still sufficiently short to allow for fast averaging. Adding of glycerol to further decrease the mobility and use of deuterated solvents to decrease spin-spin interactions can drastically improve the situation.

Very long traces (25  $\mu$ s) were performed on deuterated proteins.<sup>65</sup> So far the trace length has only been discussed in connection to the distance range, neglecting the fact that the experimental signal will have a background from the intermolecular dipole-dipole interaction. The background can be drastically reduced by using strongly diluted samples (spin concentration  $c_{\text{spin}} < 100 \mu\text{M}$ ). However even very large dilutions will result in PELDOR/DEER traces having a background that needs to be removed before extracting distances. The most accurate way to determine an experimental background is measuring singly labelled samples under the same conditions for both label positions.  $V_{\text{inter}}(t)$  will be the product of the signal detected from samples with a single label at position 1 and 2 ( $V_{\text{inter},1}(t)$  and  $V_{\text{inter},2}(t)$ , respectively):

$$V_{\text{inter}}(t) = V_{\text{inter},1}(t)V_{\text{inter},2}(t) \quad (15)$$

If this procedure is not performed the background has to be fitted to the experimental trace. This is best done at a part of the signal where the oscillation has decayed. This is why a trace should be recorded sufficiently long to cover enough signal after the oscillation has decayed. Several options for a background model are possible. If the spin concentration, giving rise to the background, is uniformly distributed in space ( $c = c(\mathbf{r}=0) = c(\mathbf{r}) = \text{const.}$ ), the background can be described by a simple exponential decay.

$$V_{\text{inter}}(t) \cong \exp(-\lambda k_0 ct) \quad (16)$$

It should be noted that the background will often take more complicated forms. Reasons for the deviation include excluded volume effects due to

the large size of the studied macromolecule or repulsion due to charges (like for instance in case of nucleic acids), leading to  $c(r=0) \neq c(r)$ . Layered environments like lipid bilayers will reduce the available space for intermolecular interactions from 3 to 2 dimensions. In this case higher order polynomials are a reasonable model for the background. After background removal distance distributions can be extracted from fitting of the experimental time trace. Simulation of a dipolar evolution, ( $V_{\text{inter, sim}}(t)$ ), can be achieved through multiplication of a given distance distribution  $P(r)$  with a kernel function  $K(t, r)$ , given analytically by equation (10).

$$V_{\text{intra, sim}}(t) = K(t, r)P(r) \quad (17)$$

Calculation of  $P(r)$  from a given dipolar evolution in contrast is an ill-defined problem, very subtle changes in the fit lead to substantial changes in the extracted distribution. To address this problem fitting is performed with a numerical algorithm called Tikhonov regularization.<sup>66</sup> The distance distribution best represented by the experimental time trace, which is found by minimization of the following function to find the optimal compromise between artefact suppression and resolution of the distance distribution.

$$G_{\alpha} = \|V_{\text{intra, sim}}(t) - V_{\text{intra, exp}}(t)\|_{\alpha}^2 + \alpha \left\| \frac{d^2}{dr^2} P(r) \right\|_{\alpha}^2 \quad (18)$$

The first term on the right hand side describes the root mean square deviation (r.m.s.d.)  $\rho(\alpha)$  between experimental ( $V_{\text{inter, exp}}(t)$ ) and simulated ( $V_{\text{inter, sim}}(t)$ ) dipolar evolution function. The second term is the product

of a regularization parameter  $\alpha$  and the norm of the second derivative of the distance distribution, describing the smoothness  $\eta(\alpha)$  of the fit. Small values of  $\alpha$  will lead to a simulated dipolar evolution reproducing parts of the experimental noise and lead to distance distributions consisting of unrealistically narrow peaks. If in contrast  $\alpha$  is chosen too large, the distribution will be very smooth; the dipolar evolution however will deviate strongly from the experimental data. The optimal  $\alpha$ , meaning the best compromise between smoothness and r.m.s.d., can be found by plotting  $\ln \eta$  vs.  $\ln \rho$  (Figure 2-9). As for small  $\alpha$ ,  $\ln \eta$  is large and strongly dependent on  $\alpha$ , but  $\ln \rho$  is small and will not change significantly with  $\alpha$ , there is a steep decaying branch at the beginning of the plot.

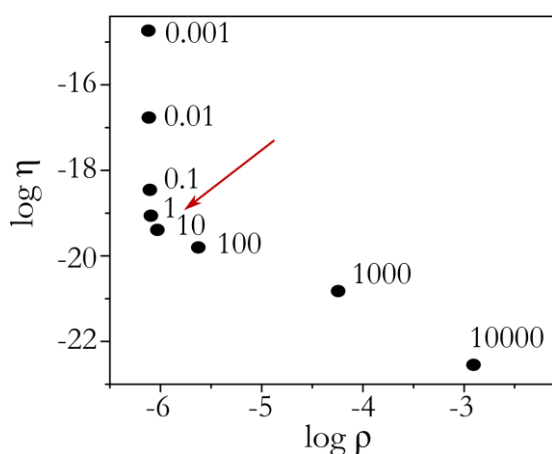


**Figure 2-9: L-Curve**

*A plot of the  $\log \rho$  (root mean square deviation r.m.s.d. between experimental and simulated time trace) vs. the  $\log \eta$  (second derivative of the distance distribution) for  $\alpha$ -values between 0.0001 and 10,000 gives rise to a characteristic curve, called L-curve. The best compromise between r.m.s.d. of the fit and smoothness/width is found for the  $\alpha$ -value in the corner of the curve (marked by red arrow).*

For large  $\alpha$  however,  $\ln \rho$  will increase with increasing  $\alpha$  and the smoothness will only weakly depend on  $\alpha$ , leading to an only weakly decaying branch of the plot. Optimal  $\alpha$  is chosen at the corner as point of the best compromise between smoothing of the distance distribution and quality of the fit. In addition to distance distributions, the number of spins within a macromolecule can be determined according to

equation (13). Since the experimental modulation depth  $\Delta$  is not only dependent on the number of coupled spins, but also on excitation conditions, calibration is required to accurately determine the number of spins. To do such a calibration, PELDOR/DEER traces on systems with known number of spins within the macromolecule, have to be recorded under conditions used in the experiment.

All obtained distance distributions can only be interpreted reliably if the experimental data are suited. Analysis of traces with low signal to noise, short evolution times or artefacts like modulations from hyperfine interactions (ESEEM) or orientation selection should be treated conservatively and discussion of the distribution may lead to over interpretation of the experimental data.

#### **2.2.4 PELDOR vs. Other Techniques of Pulsed Dipolar Spectroscopy**

Although several pulsed EPR techniques have been proposed (§ 2.1.2) PELDOR is by far the most applied pulse sequence for good reasons. A sequence known as “2+1” introduced by KURSHEV *et al.* in 1988 is the single frequency equivalent to the three pulse DEER. It is less demanding in terms of instrumentation as only a single microwave source is required and the Q-value of the used resonator does not have to be lowered to increase the bandwidth as for PELDOR/DEER. Nonetheless, it has been driven out by the dual frequency technique. The main drawback is the dominance of modulations arising from hyperfine interactions, which strongly interfere with the dipolar oscillations, aggravating data analysis.<sup>28, 53</sup> Another single frequency method, mainly developed and applied by the group of FREED is using double-quantum

coherences (DQC) to detect the dipolar coupling.<sup>29, 30</sup> They introduced a six-pulse sequence shown in Figure 2-2. In contrast to PELDOR/DEER, full excitation of the EPR line is required for DQC experiments leaving high demands in terms of instrumentation, as high microwave power is required. DQC experiments do not encode the number of coupled spins or the mutual orientation between the labels, leaving the experiment less prone to artefacts but reducing the information content at the same time. SIFTER is a technique that refocuses instantaneous diffusion and is thereby increasing the resolution especially for distances longer than three nanometres.<sup>32</sup> Adversely, the experiment requires excitation of the whole EPR line for ideal performance. Non-ideal excitations, which are commonly achieved, will open unwanted coherence pathways, which will be reflected in the detected signal. SCHÖPS *et al.* could show in a recent publication, that broadband SIFTER, performed with adiabatic pulses generated by an arbitrary wave generator, delivers artefact free time traces, potentially making the sequence a competitor for PELDOR/DEER.<sup>45</sup> RIDME is also a stimulated echo sequence delivering time traces with the dipolar coupling encoded as an oscillation. The technique has the potential to cover a weak spot of the PELDOR/DEER sequence, distance measurements involving paramagnetic metals with very short relaxation times and strong g-anisotropy like iron(III)- or manganese(II)-ions. PELDOR/DEER experiments on these systems suffer from low signal-to-noise ratio and orientation selection artefacts. In RIDME modulation of the observed echo (A spins) is induced by longitudinal relaxation of the B spins, making the technique particular powerful for experiments on species with large differences in relaxation properties like nitroxide-metal pairs. ABDULLIN *et al.* showed the superiority of RIDME over PELDOR

for distance measurements between  $\text{Fe}^{3+}$  and a nitroxide in the iron containing cytochrome P450cam protein.<sup>35</sup> However, the drawback of this promising technique is encoded in title of the original publication from KULIK *et al.* “*Electron dipole–dipole interaction in ESEEM of nitroxide biradicals.*” The technique suffers from a strong sensitivity for hyperfine modulations, raising the demand for suppression by additional experimental steps.



### 3. Chapter

## Introduction to Site-Directed Spin Labelling EPR

A number of biomolecules have intrinsic paramagnetic centres that can be studied by EPR. Examples include metalloenzymes carrying redox active transition metal ions, as well as proteins having organic radicals involved in catalysis. However, the majority of proteins is diamagnetic and therefore, in its native state, invisible to EPR techniques. In 1989 W. HUBBEL introduced a technique allowing the attachment of a spin-label to a biomolecule at a user-defined site.<sup>11, 67</sup> The technique of site-directed spin labelling (SDSL) had a significant impact breaking the limitation of EPR application to biological relevant molecules. An overview of labelling strategies and labels will be given in this chapter.

### 3.1 Strategies for Site-Directed Spin Labelling

Since the introduction SDSL 25 years ago, the method has been pushed forward by several developments, up to recent success in *in vivo* spin labelling.<sup>68, 69</sup> Figure 3-1 displays several strategies for spin labelling a protein. The choice of labelling method will be influenced by properties of the label and target protein, also questions of labelling efficiency should be considered. The most commonly used approach up to date is still the chemical conjugation of cysteines with the nitroxide label **MTSSL** ((1-oxyl-2,2,5,5-tetramethylpyrroline-3-methyl) methanethio-sulfonate). The method is convincing due to its technical simplicity and high labelling efficiency.

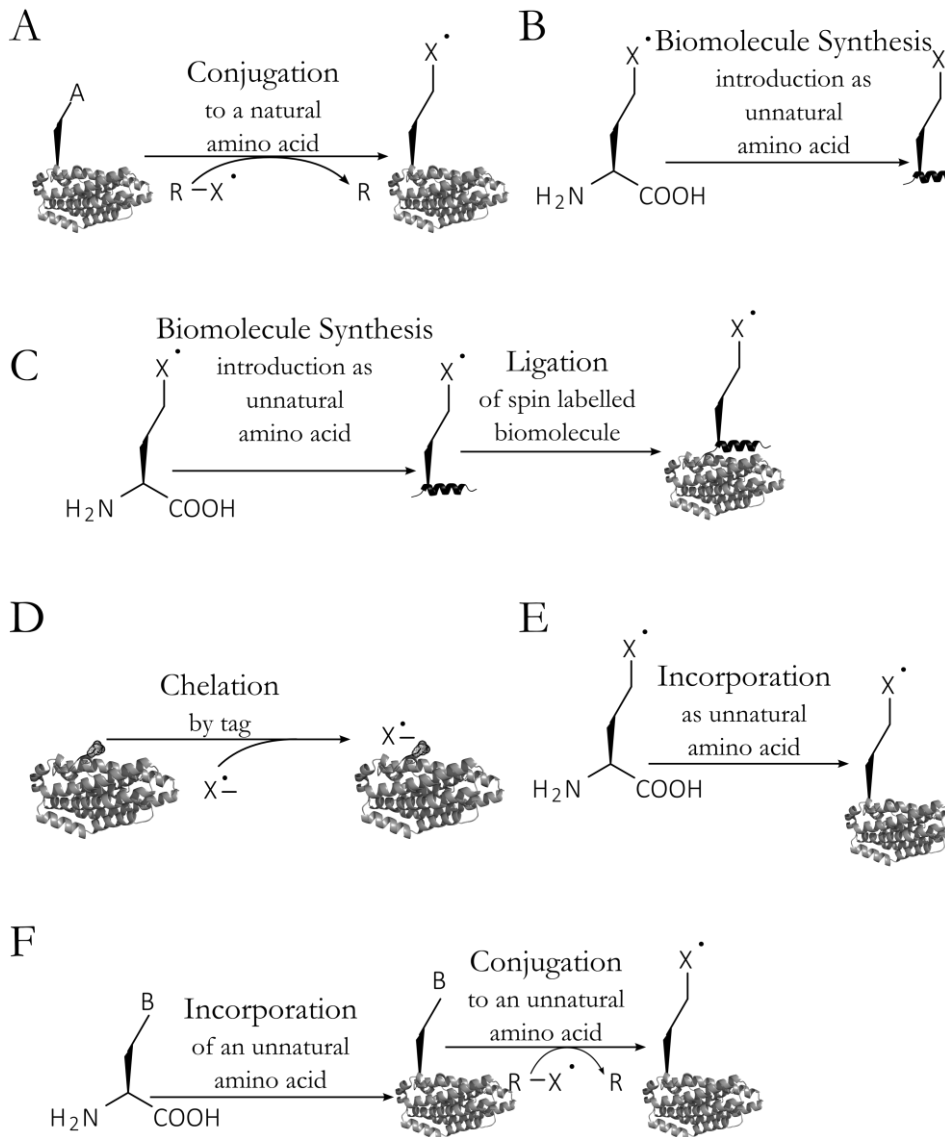


**Figure 3-1: Strategies for Site-Directed Spin Labelling**

*Strategies for the incorporation of a spin label ( $X^\bullet$ ) into a biomolecule, adapted from reference<sup>69</sup> A: Conjugation to natural amino acids. B: Introduction as unnatural amino acid during synthesis of the biomolecule. C: B followed by ligation of the synthesized biomolecule to the studied biomolecule D: Spin labelling by chelation to genetically encoded tags. E: Incorporation as unnatural amino acid F) Incorporation of an unnatural amino acid, followed by labelling.*

However labelling of natural amino acids such as cysteine requires site-specific mutations that may influence the protein's structure and

function. This limits the applicability to proteins not affected by this interference. Alternative binding of a paramagnetic species can be realized using chelation. (Figure 3-1, D) Several chelate-tags have been proposed for coordination of metals like gadolinium or manganese.<sup>70, 71</sup> Synthesis of peptides carrying the spin label as an unnatural analogue (Figure 3-1, B and C) enables the introduction of a large variety of labels with specific chemical and spectroscopic properties, which are inaccessible by other labelling schemes. However, this procedure suffers from a limitation concerning size and natural folding of the biomolecule. This restriction can be broken down by ligation of the synthesized sequence to an expressed biomolecule, which requires large technical efforts and may not be applicable in every case. The most elaborate way is the introduction of genetically encoded unnatural amino acids into endogenous proteins, as it is the minimal intervention to the natural state.<sup>72</sup> The unnatural amino acid can serve as reaction partner having a unique chemical functional group that can be conjugated with a spin label in a subsequent step.<sup>73</sup> Recently the direct biosynthesis of a spin labelled biomolecule *in vivo* has been reported.<sup>74</sup> Strategies for nucleic acid sequences offer a comparable variety.<sup>75, 76</sup> In analogy to amino acids spin labels can be introduced during solid phase oligonucleotide synthesis, or post-synthetically conjugated to functional groups installed in this process. A large variety of convertible nucleosides is commercially available, making the post-synthetic labelling procedure preferable in terms of technical ease. Longer RNA strands mimicking natural occurring ones can be generated by ligation of synthesized sequences. A strategy for labelling of long natural RNAs can be performed by complementary-addressed SDSL.<sup>77</sup>

## 3.2 Spin Label Classes

Choice of the label for an EPR distance measurement will depend on demands with respect to the label in terms of rigidity and sensitivity, but also on the target biomolecule and the applicable labelling strategy. While nitroxide labels clearly dominate EPR distance measurements, several label classes have been proposed in the last years. Metal-based spin labels and carbon-centred organic radicals offer an alternative to nitroxides, and open up the possibility of orthogonal labelling.<sup>78</sup>

### 3.2.1 Metal-Based Spin Labels

In recent years a variety of metal-based spin labels have been proposed. Metals in general have spectroscopic properties very distinct from those of organic radicals. Additionally, the chemical stability of metal-based labels even under *in cell* conditions should be highlighted. The majority of metal-based labels are introduced via chelation, usually by ligate systems that are conjugated to an amino acid. Coordination by genetically encoded tags has been reported for manganese<sup>71</sup>, copper<sup>79</sup> and gadolinium<sup>70</sup>. Gadolinium (III) labels have been proposed for EPR distance measurements by RAITSIMRING *et al.* in 2007 for several rationales.<sup>80</sup> First,  $Gd^{3+}$  is a  $S=7/2$  system with a very narrow  $m_s = +1/2 \rightarrow m_s = -1/2$  transition, that is not broadened by g-anisotropy, as it is the case for nitroxides, leading to an increased sensitivity especially at high fields and frequencies. Orientation selection effects are usually suppressed by the broad distribution of transitions affected by the zero-field splitting (ZFS). Second, short longitudinal relaxation time of  $Gd^{3+}$  allows for very fast averaging. Distance measurements have been performed on gadolinium-labelled nucleic acids, trans-membrane

peptides and proteins *in vitro* and *in cell*.<sup>81-85</sup> The use of Cu<sup>2+</sup> for distance measurements has been reported in literature, however a lot of challenges arise when copper is used as spin probe. Due to strong g-anisotropy its EPR spectrum is very broad even at low fields and frequencies. As the excitation bandwidth in pulsed experiments is limited this leads to low sensitivity when compared to nitroxides and more pronounced orientation selective effects have to be considered. Another metal-based label having the potential for *in cell* PELDOR/DEER experiments is Mn<sup>2+</sup> coordinated to genetically encoded His-tags.<sup>71</sup> Manganese is endogenous to cells and, in contrast to copper, not toxic.

### 3.2.2 Carbon-Centred Organic Radicals

The most widely applied carbon centred radical is the tetrathiarylmethyl radical (TAM). When compared to nitroxides, TAM has a narrow EPR line and a long transversal relaxation time even at high temperatures. Especially the long phase memory time  $T_m$  is a very attractive property for EPR distance measurements. While standard nitroxide's  $T_m$  at room temperature is in the range of around 600 ns (in trehalose), making relaxation too fast at room temperature to allow for PELDOR/DEER experiments, TAM still has a relaxation time in the regime of microseconds.<sup>86-89</sup> A study performed by REGINSSON *et al.* on TAM-nitroxide labelled model compounds demonstrated increased sensitivity, in terms of higher modulation depth, when compared to nitroxide-nitroxide label analogues.<sup>90</sup> YANG *et al.* could show the labels potential for pulsed EPR distance measurements close to physiological temperatures.<sup>91</sup> However, the large size of TAM may lead to distortions of a biomolecules structure and is therefore limited in application.

### 3.3 Nitroxide Spin Labels

Spin labelling using nitroxides is the most dominant approach in EPR spectroscopy. During the last decade a vast selection of radicals has been proposed and applied in numerous studies.<sup>92</sup> Development was driven by improving nitroxide properties in terms of chemical stability<sup>93</sup>, relaxation times<sup>88</sup> and diversification of labelling strategies.<sup>74, 94</sup> Nitroxide spin probes may be classified by parent structures (Figure 3-2, A), most commonly: five-membered rings (pyrrolidines, pyrrolines), six-membered rings (piperedines) and systems of fused rings (isoindolines).

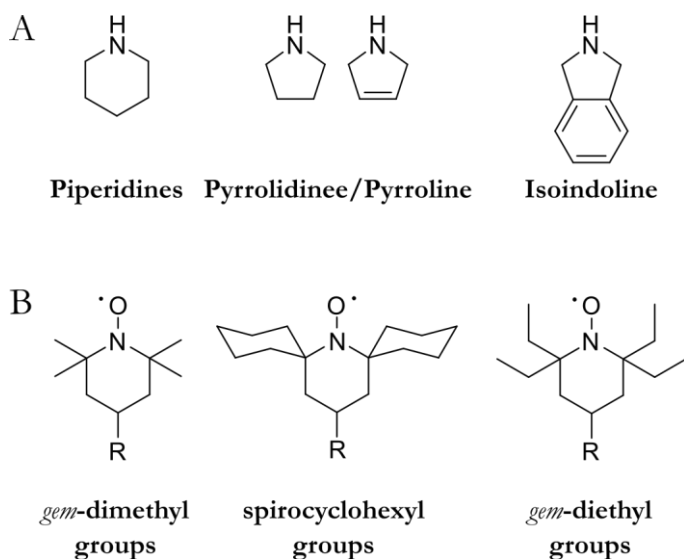


Figure 3-2: Examples for Nitroxide Parent Structures and Steric Groups

A: Examples for nitroxide parent structures for Six-membered rings (piperidine), five-membered rings (pyrrolidinepyrroline) and fused ring systems (isoindoline) B: Examples for steric groups at 2 and 5-positions of piperidine derived spin labels: most commonly used are *gem*-dimethyl groups (giving **TEMPO** (2,2,5,5-tetramethyl-pyrrolin-1-oxyl-3-acetylene)) or more bulky substituents to increase relaxation times and stability of the radical function, such as spirocyclohexyl and *gem*-diethyl groups.

To increase the stability of the radical, additional groups are introduced adjacent to the N-O moiety, sterically shielding the radical group. The most abundantly are *gem*-methyl groups (Figure 3-2, B). However, the increased lifetime of the radical comes with the price of significantly shorter relaxation time  $T_m$  due to rotation of the methyl groups at rates that are comparable to the anisotropy of the hyperfine coupling between the electron and the protons of the methyl groups, at temperatures above 60 K.<sup>95</sup> In the last years derivatives carrying more bulky groups (Figure 3-2, B), such as spirocyclohexyl- or *gem*-diethyl-groups, have been proposed to increase both, relaxation time and chemical stability towards reduction, to enable EPR experiments at more physiological conditions, namely room temperature and *in cell*. In 2010, KATHIRVELU and co-workers suggested that the use of a spirocyclohexyl nitroxyl radical would enable inter-spin distance measurements at temperatures up to 125 K, eliminating the need to work at liquid helium temperatures.<sup>96</sup> Five years later the group published the first room temperature PELDOR/DEER using a nitroxide label.<sup>89</sup> The authors presented a 1.4  $\mu$ s long time trace (3.2 nm) recorded on T4 lysozyme doubly labelled with a spirocyclohexyl substituted nitroxide label, which was immobilized in trehalose to avoid isotropic tumbling of the protein that would average the dipolar interaction to zero. A large variety of bulky substituents increasing the relaxation time can be found in literature for nitroxides, enlarging the scope of spin probes suited for room temperature distance measurements.<sup>88</sup> The major limitation, compared to trityl- or gadolinium-based spin labels, when it comes to *in cell* EPR experiments, is the liability of nitroxide radicals towards reduction. It could be shown, that next to other structural properties, sterical shielding by bulky substituents has a positive impact on the redox potential and

increases the nitroxide stability under *in cell* conditions.<sup>93, 97</sup> However an appreciable advantage of nitroxides is their small size, when compared to other spin labels for EPR (§ 3.2.1 and 3.2.2) or reporter groups employed in other spectroscopic techniques (e. g. fluorophores). The introduction of bulky substituents calls for more caution in ensuring a non-perturbing character of the reporter.

### 3.3.1 Nitroxide Spin Labels for Nucleic Acids

Nucleotides in general offer three different labelling sites for post-synthetic spin labelling, namely the phosphate-backbone, the sugar-backbone and the nucleobase itself (Figure 3-3, inset). QIN *et al.* proposed the attachment of a nitroxide label to the RNA-backbone via a phosphorothioate scheme, to enable sequence independent labelling.<sup>98, 99</sup> This so-called **R5** (Figure 3-3, C) was employed for PELDOR/DEER studies on DNA 12mer duplex as model system for distances up to 3.9 nm,<sup>100</sup> as well as for distance measurements to elucidate “*conformations of a human telomeric G-quadruplex*”.<sup>101</sup> However, the three single bonds linking the nitroxide to the phosphate backbone give rise to a rather large conformational space occupied by **R5**, making intensive computational modelling a constant accompanist for data analysis.<sup>102</sup> To address this issue the author introduced a new generation of the label, now called **R5c** (Figure 3-3, C). **R5c** is a bifunctional analogue of **R5**. Its reduced mobility could be confirmed by cw-EPR.<sup>103</sup> In 2001 EDWARDS *et al.* published labelling of the sugar backbone, allowing the attachment of a TEMPO-derivative to the 2'-position of internal base-paired RNA nucleotides of RNA.<sup>104, 105</sup> The label (Figure 3-3, B) was used for EPR



distance measurements on a “distance ruler” series of doubly labelled DNA, for distances up to 6.8 nm.

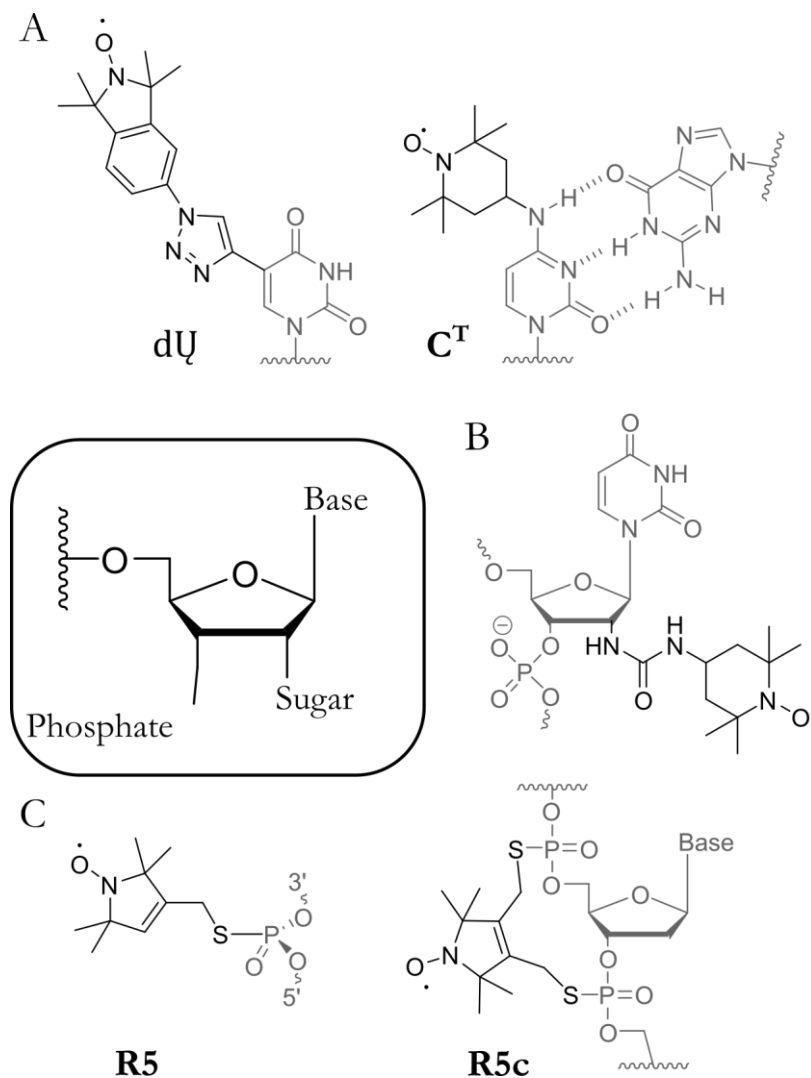


**Figure 3-3: Nitroxides for Post-Synthetic Nucleic Acid Labelling**

*Examples for nitroxide spin labels that can be attached post-synthetically to functionalized nucleotides of an oligonucleotide. The inset shows the three positions a label may be attached to: the phosphate- or sugar-backbone or the nucleobase. A: Examples for spin labels attached to the nucleobase: TEMPO attached to Cytosine ( $C^T$ ) and the isoindoline derived spin label conjugated to Uridine via “click” chemistry giving the fairly rigid  $dU$ . B: TEMPO label attached to the 2'-position of the sugar-backbone. C:  $R5$  and its bifunctional analogue  $R5c$ , which can be attached to the phosphate backbone.*

As the label is positioned at the backbone of the DNA duplex it is pointing away from the helix axis, therefore the distance variation with base-pair separation between the two labels, will not be a linear relationship.<sup>106</sup> The largest variety of nitroxide labels is available for conjugation to the nucleobase or nucleobase analogues. Some allow for post-synthetic attachment of the nitroxide radical to a unique functional group, others are incorporated

during automated chemical synthesis. One example is a label that is conjugated to 4-thio-Uridine, however the linker connecting the nucleobase to the label employs 5 rotatable

bonds.<sup>107</sup> DING *et al.* suggested the use of the azide-alkyne (CuAAC) “click” reaction,

delivering a piperidine-derived spin label linked to the 7'- and 5'-position of adenosine and uridine, respectively by a triazole, as a possibility for post-synthetic modification of nucleobases.<sup>108</sup> The same approach was used to attach an isoindoline derived label to Uridine (**dU**, Figure 3-3, A).<sup>109, 110</sup> The authors note that, although **dU** has two rotatable single bonds, giving rise to mobility of the nitroxide moiety at room temperature, but that the label takes an almost planar conformation upon freezing. They could show that the rigidity gives rise to orientation selectivity in PELDOR experiments at Q-band frequencies, only slightly less pronounced than the one observed when working with **Çm** (Figure 3-4).<sup>110</sup> This finding makes **dU** a potential candidate for orientation selective PELDOR/DEER experiments. Accurate distance

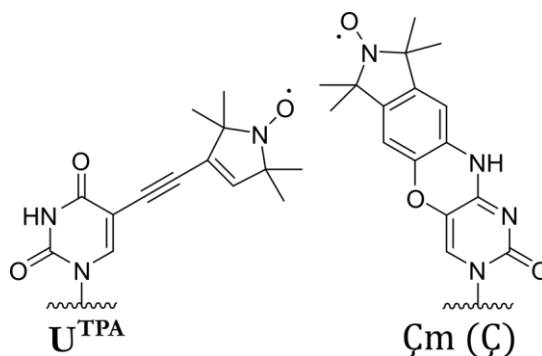


Figure 3-4: Nitroxides Introduced During Oligonucleotide Synthesis

Chemical structures of **UTPA** and **Çm**

measurements however are compromised by orientation selection. Almost 30 years ago SPALTENSTEIN *et al.*, labelled the commercially available 5-iodo-2'-deoxyuridine with TPA and introduced the thymidine analogue into a DNA sequence.<sup>111, 112</sup> The approach was extended to RNA giving analogues for uridine (**UTPA**, Figure 3-4), cytosine and adenosine.<sup>113, 114</sup> The authors highlighted that TPA's advantages for EPR spin labelling in general and PELDOR/DEER in particular: the label offers a broad range of labelling sites (RNA or DNA, minor or major groove) and introduces only minor local perturbations to the structure. Additionally the short and rigid linker would enable the observation deep modulations in PELDOR/DEER experiments and translation of experimental distances into structure would be less ambiguous. Following an approach for DNA, HÖBARTNER *et al.* introduced post-synthetic spin labelling of the RNA nucleobases guanine, adenine and cytosine with TEMPO (**CT**, Figure 3-3, A) using convertible nucleosides.<sup>115</sup> X-band PELDOR spectroscopy in combination with the TEMPO-labelled nucleotides on different secondary structures, including the equilibrium between duplex and hairpin structure of a self-complementary sequence as well as a quadruplex structure, resulted in narrow distance distributions for a distance range between 2 and 4 nm.

### 3.3.2 Nitroxide Labels for Proteins

Conjugation of the fairly famous methanethiosulfonate spin label (MTSSL) to cysteines through formation of a disulphide bond (**R1**, Figure 3-5, A) is the most widely used approach.<sup>116, 117</sup> The labelling procedure convinces through great technical ease, and the label itself is known to have minimal impact on the protein's secondary structure.

However, the long linkage offers several rotatable bonds between the proteins backbone in the NO moiety. This leads to a large conformational space for the spin density. A lot of effort had been made to account for the spin labels dynamic, as this knowledge is crucial for interpretation of experimental inter-spin distances in terms protein structure.<sup>118</sup> Rotamer libraries have been created for several macromolecular structures.<sup>119, 120</sup> In more specific cases interpretation of inter-spin distances can be supported by molecular dynamic (MD) simulations or Monte Carlo conformational searches. To avoid ambiguity arising from MTSSL's large conformational space developments have been pursuit aiming at more rigid spin labels. In analogy to the development of **R5c** from **R5** (Figure 3-3) the so-called **Rx** has been developed from **R1** (Figure 3-5, A). It is a bifunctional analogue to **R1**, linked to two cysteines being direct neighbours ( $\beta$ -sheets) or three to four positions apart (helical structures).<sup>121</sup> **Rx** was successfully employed to study membrane proteins and its performance to deliver narrow distance distributions in comparison to **R1** was shown experimentally and supported by MD simulations.<sup>122, 123</sup> STEVENS *et al.* discussed **Rx**'s feasibility for orientation selective PELDOR/DEER studies at W-band fields and frequencies.<sup>124</sup> In cases were cysteines are essential for the proteins structure, by providing disulphide bonds or offering binding sites for cofactors, or function, alternative target amino acids for conjugation are required. Labels for arginine, serine and tyrosine have been proposed.<sup>125-128</sup> The latter is the target for a spin label called **Nox** (Figure 3-5, A).<sup>129</sup> The isoindoline-based nitroxide radical is attached to tyrosine via Mannich bioconjugation. Up to now, the label has been mainly used as reporter for side chain mobility in intrinsically disordered proteins.<sup>130, 131</sup>

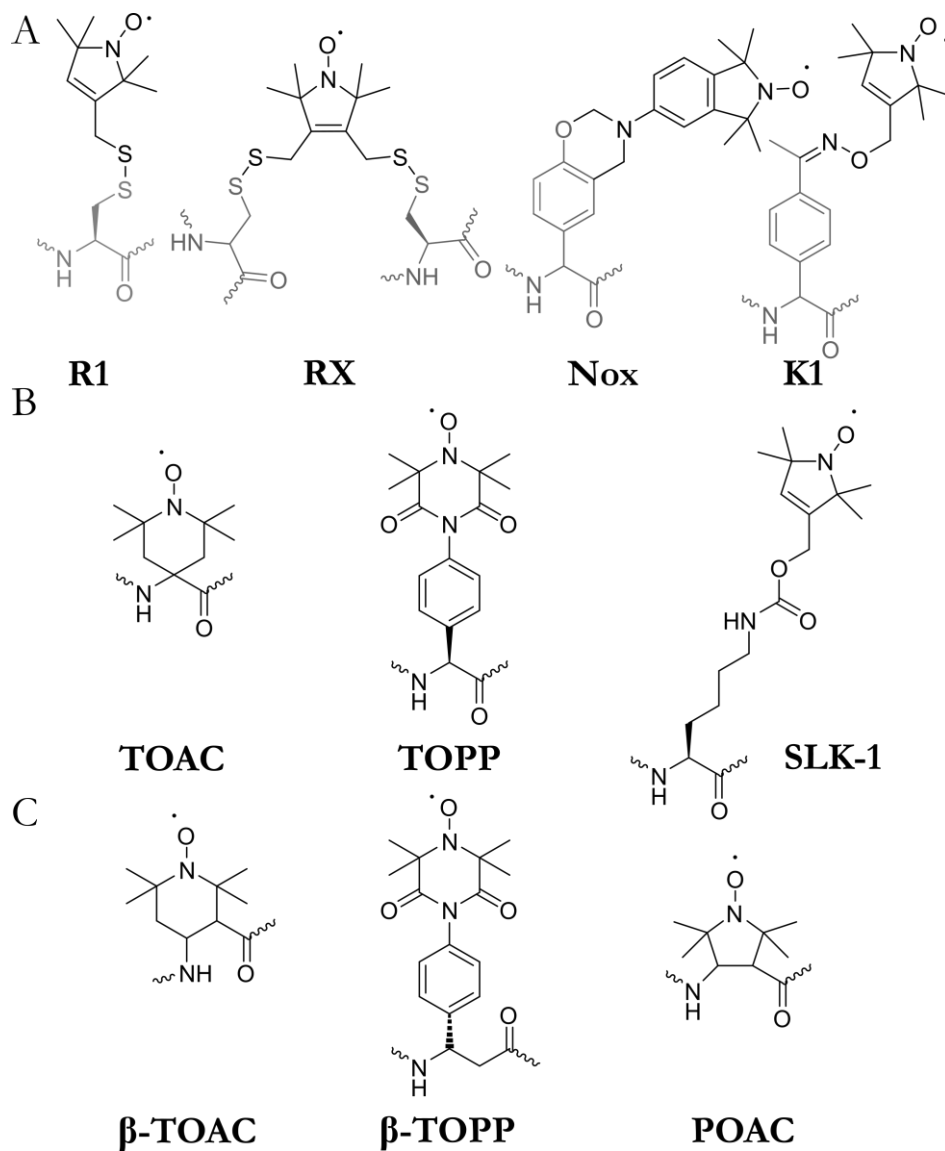


**Figure 3-5: Nitroxides for Labelling of Amino Acids**

*A: Spin labels for amino acids (displayed in grey) with the cysteine labels **R1** and **Rx**, the tyrosine label **Nox** and **K1** as a nitroxide attached to the unnatural amino acid para-acetylphenylalanine (*pAcF*). B: Spin labels that are introduced as unnatural amino acid e.g. **TOAC**, **TOPP** and **SLK-1**. C: Spin labels that are introduced as unnatural  $\beta$ -amino acid e.g.  **$\beta$ -TOAC**,  **$\beta$ -TOPP** and **POAC***

In 2009 FLEISSNER *et al.* suggested the use of an unnatural amino acid (acetylphenylalanine), which can be genetically encoded, for providing a

keto-group as, among the natural amino acids, unique chemical group. Reaction with a hydroxylamine functionalized nitroxide yields the spin labelled side chain designated **K1** (Figure 3-5, A).<sup>73</sup> The use of a non-canonical amino acid reduces the number of point mutations required for a doubly labelled sample to two, which is advantageous especially when working on cysteine rich sequences.<sup>132</sup> An alternative to conjugation of the spin label to natural or unnatural amino acids is the introduction of unnatural amino acids as spin labels. This approach in general offers more possibilities for label-design, especially the absence of a need for linkers to functional groups of the amino acid sequence facilitated development of rather rigid spin labels. The potential of breaking the limitation to synthesized sequences could be shown in recent years. In 2014 genetically encoding of a spin labelled amino acid, **SLK-1**<sup>74</sup> (Figure 3-5, C) was published. The *in vivo* biosynthesis of spin labelled proteins enables EPR distance measurements on native, endogenous proteins for structural studies.<sup>133</sup> **SLK-1**, however is a flexible label giving rise to a large conformational space and distance distributions comparable to **R1**. The first label introduced into a peptide backbone rather than the side chain was **TOAC** (2,2,6,6-tetramethyl-N-oxyl-4-amino-4-carboxylic acid, Figure 3-5, B) in 1981.<sup>134</sup> The label was used in numerous studies to investigate peptide's backbone dynamic and secondary structure, especially in trans-membrane systems.<sup>135</sup> In 2007 INBARAJ *et al.* demonstrated the use of cw-EPR in conjunction with **TOAC** for the determination of a peptide's (analogue of the nicotinic acetylcholine receptor trans- membrane helical domain) tilt angle in a mechanical aligned membrane.<sup>136</sup> This study was enabled as **TOAC** has a, despite admittedly present ring conformations, rather rigid orientation with respect to the peptide backbone. A conformational restriction also

is a favourable condition for EPR distance measurements. However, **TOAC** is a C $\alpha,\alpha$ -disubstituted amino acid potentially disturbing secondary structure.<sup>135, 137, 138</sup> Following TOAC's example the unnatural  $\beta$ -amino acids  **$\beta$ -TOAC**<sup>139</sup> and **POAC** (2,2,5,5-tetramethylpyrrolidine-*N*-oxyl-3-amino-4-carboxylic acid)<sup>140, 141</sup>, (Figure 3-5, C) have been introduced into peptides. With the objective of a conformational rigid spin label having less potential for structural disturbance, STOLLER *et al.* developed a regular chiral  $\alpha$ -L-amino acid called **TOPP** (4-(3,3,5,5-tetramethyl-2,6-dioxo-4-oxypiperazin-1-yl)-L-phenylglycine).<sup>142</sup> As shown in Figure 3-5, B the label's N-O bond is aligned to the same axis as the C $\alpha$ -C $\beta$  connection. Density functional theory (DFT) calculations of the **TOPP** fragment backed up the molecular geometry with the nitroxide moiety fastened collinear to the C $\alpha$ -C $\beta$  bond. To investigate the label's capacity for EPR distance measurements the authors performed an X band (9 GHz) PELDOR/DEER study on an alanine rich transmembrane model peptide doubly labelled with **TOPP**. Experiments on the **TOPP**-labelled peptide yielded time traces showing clear modulations, meaning narrow distance distributions, and were not affected by orientation selection artefacts. Due to its rigid design the label could be used for an orientation selective PELDOR study performed at W band.<sup>62</sup> Analysis of the experiments unveiled the mutual orientation between the two labels. Concededly a libration of  $\pm 20^\circ$  around the two single bonds was required to fit the experimental data, indicating some rotational freedom around these bonds. It is worth highlighting, that this libration does not alter the position of the NO moiety in space, hence is not increasing the width of the distance distribution. To enable the insertion of the label into  $\beta$ -peptides a  $\beta$ -amino acid analogue ( **$\beta$ -TOPP**, Figure 3-5, C) has been developed (unpublished).

## 4. Chapter

### Scope of the Thesis

#### 4.1 High-Power PELDOR at Q band - Motivation

This thesis is investigating the performance of PELDOR/DEER, taking advantage of some recent advances in pulse EPR instrumentation, more specifically the availability of PELDOR/DEER at Q-band fields and frequencies (1.2 T/34 GHz) with high microwave power (170 W). This setup is offering two advantages: increased sensitivity and suppression of orientation selection artefacts. Q band is advantageous over the standard X-band in terms of sensitivity,<sup>143, 144</sup> as in general the absolute sensitivity (spins/mT or spins/GHz) increases with field and frequency for several reasons. One contribution is an increase in population difference between the two spin states, due to an increased Zeeman splitting. Additionally the shorter wavelength of higher frequencies reduces resonator dimensions, leading to smaller sample volumes still having a high filling factor.<sup>145</sup> The signal-to-noise ratio (S/N) scales with the microwave frequency  $\omega$  according to<sup>143</sup>

$$S/N \propto \frac{\sqrt[2]{\omega^3} Q_L N}{\sqrt{F_N} \sqrt{V_c}} \quad (19)$$

$N$  is the number of spins and  $V_c$  the effective sample volume, which is defined by the sample volume  $V_s$  and the filling factor  $\eta$  ( $V_c = V_s/\eta$ ).  $F_N$  denotes the receiver noise. The quality factor of the resonator  $Q_L$  increases proportionally to  $\omega$ , excitation bandwidth is assumed to be the



same at the different microwave frequencies. Further assuming a negligible microwave dependence of  $F_N$  and the same number of participating spins the signal-to-noise-ratio can be estimated to scale with  $\omega^2$ . With 9.5 and 34 GHz for X and Q-band frequency, respectively an enhancement of 12.5 can be predicted.

$$\frac{S/N (34 \text{ GHz})}{S/N (9.5 \text{ GHz})} \approx 12.8 \quad (20)$$

In experiments comparing the performance of PELDOR/DEER experiments at X and Q band an increase in signal-to-noise ratio of 13 and 10 to 20 were measured.<sup>144, 146</sup> The use of high microwave power allows the application of harder pulses, comparable to those applied at X-band frequencies. The larger excitation bandwidth provides another advantage. While employing spin labels with reduced mobility is preferable to achieve narrow distance distributions it also potentially introduces orientation selection artefacts that hamper with data analysis. Adversely PELDOR experiments at Q band are more prone to orientation selection artefacts, when compared to X band, due to partial resolution of g-anisotropy. High power microwave irradiation allows for application of short pulses (large excitation bandwidth), potentially allowing to suppress orientation selection.<sup>146</sup>

These advantages will be exploited to evaluate the capability of PELDOR/DEER experiments at Q-band fields and frequencies in conjunction with semi-rigid spin labels for accurate distance measurements, in two challenging cases: measuring very long distances (up to 8 nm) and distance measurements in systems with enhanced relaxation (in lipid bilayers).

### 4.1.1 Ribonucleic Acids (RNA)

Since the first report of catalytic active RNA in 1982<sup>147</sup>, it has been recognized that RNAs are more than just a transporter of information from deoxyribonucleic acid (DNA) to the protein machinery of the ribosome. In fact 98 % of RNAs are non-coding (nc),<sup>148</sup> and their functions include numerous regulatory purposes.<sup>149-151</sup> Riboswitches regulate gene expression by conformational change dependent on temperature or upon metabolite binding. Protein binding sRNAs can modulate their cognat proteins activity in an antagonistic fashion; or play an essential role for activity. A cell defence mechanism against bacteriophages and plasmids based on RNA is performed by the clustered, regularly interspaced short palindromic repeats (CRISPR), which are direct protein nucleases against intruding DNA.<sup>152</sup> Transcriptomic studies piled up a tremendous amount of ncRNAs, without any idea about their structure or function, as RNAs pose quite a challenge for structural investigations. They intrinsically contain lots of flexible elements like loops, linkers or termini, making crystallization particular difficult; even close to impossible. Truncation may help the formation of crystals suited for x-ray structures but strongly hampers with the meaningfulness of the obtained structure. Additionally their function is connected to a large conformational dynamic, which cannot be captured by x-ray crystallography. The method of choice for probing dynamical structures is NMR spectroscopy. However functional RNAs can be several thousand nucleotides long,<sup>153</sup> and therefore a lot of biological relevant RNAs or complexes are exceeding the techniques size limitation. EPR is an attractive complementary approach, as shown by several studies using EPR distance measurements to follow

conformational changes of RNAs.<sup>102, 154-156</sup> PELDOR spectroscopy has been applied to monitor magnesium dependent folding of a hammerhead ribozyme<sup>157</sup> as well as conformational changes of aptamers upon binding of broad-spectrum antibiotics.<sup>158, 159</sup> In 2014 a study of the assembly of a 70 kDa ribonucleoprotein showed the power of combining NMR with EPR long-range distance constraints.<sup>160, 161</sup> A strategic placement of spin labels allowed to observe a large change of experimentally observed distances during annealing of mini TAR-DNA to mini TAR RNA upon interaction with HIV-1 nucleocapsid protein NCp7.<sup>162</sup> Furthermore large multicomponent supramolecular assemblies as the ribosome could be studied upon building a complex with a doubly spin labelled mRNA analogue.<sup>163</sup> In spite of these beautiful examples, the availability of spin-labelled RNA and the properties of the spin label itself place the limitations of PELDOR experiments.

A 34 nucleotide long RNA sequence doubly labelled with **C<sup>T</sup>** (Figure 3-3) at various positions, serves as a ruler to examine PELDOR experiments for measuring increasingly longer distances in RNA. The signal intensity of the detected echo is strongly reduced with increasing distance, due to the requirement of very long evolution times  $T$ , in the PELDOR experiments. As the **C<sup>T</sup>** label preserves the base-pairing capability its mobility is reduced, promising narrow distributions but potentially giving rise to some orientation selection.

#### **4.1.2 Transmembrane Helices (WALP)**

Integral membrane proteins represent 25-30 % of proteomes and manage numerous membrane related biological functions, such as signalling, transport and defence.<sup>164</sup> In spite of this fundamental biological

relevance, high-resolution structures of transmembrane (TM) proteins are scarce good. In June 2016 only 2.4 % of the protein structures available in the protein databank represent TM proteins. This dramatic mismatch is due, as the bottlenecks, of poor expression, limited extraction success and low purification yields, are narrower than for their soluble relatives.<sup>165, 166</sup> The first TM protein could be crystallized only 30 years after myoglobin,<sup>167</sup> and x-ray structures are still demanding due to the shortage on well-ordered 3D crystals.<sup>165</sup> The first sentence of a review from 2008 brings the extra challenge right to the point: “*Membrane proteins do not work alone.*”<sup>168</sup> TM proteins interact with their lipid environment; in fact the right interaction quite often is indispensable for structural and functional integrity. The lipids may assist folding and insertion; stabilize the structure, mediate oligomerization or segregate the proteins into distinct membrane domains.<sup>169-171</sup> Techniques like NMR, EPR and fluorescence spectroscopy that allow studying the proteins in its natural environment, a lipid, are powerful approaches to the field of TM protein structure.<sup>172-174</sup> Recent EPR distance measurements include monitoring the assembly of the TM domain of a protein from influenza A virus and structural transitions of *E. coli*'s integral membrane sulfurtransferase upon substrate binding.<sup>175, 176</sup> Despite studies of specific TM proteins, the investigation of the nature of protein-lipid interaction itself is fundamental to understand the complex interplay fostering TM protein function. Structurally, TM domains can be described by mainly two classes:  $\beta$ -barrels and  $\alpha$ -helices, with the latter being more abundant.<sup>177</sup> TM helices are typically 20-30 amino acids long, majorly composed of hydrophobic residues alanine, valine, isoleucine and most abundantly leucine.<sup>178</sup> In 1984 BLOOM *et al.* introduced a model for describing one aspect of the lipid-protein

interaction, based on the thermodynamics of the relation between the hydrophobic thickness of the membrane and the hydrophobic length of the protein, named hydrophobic matching (HM) or mismatching (HMM). Figure 4-1 illustrates the concept for an  $\alpha$ -helical structure embedded in a lipid bilayer, for the case of the helix's hydrophobic length exceeding the hydrophobic thickness of the bilayer (positive HMM). To counteract the unfavourable interaction between the hydrophobic core of the helix and the hydrophilic head groups of the lipids, several adaption mechanisms may occur (adapted from reference<sup>179</sup>). The lipids may match the helix length by stretching of their acyl-chains (Figure 4-1, A).

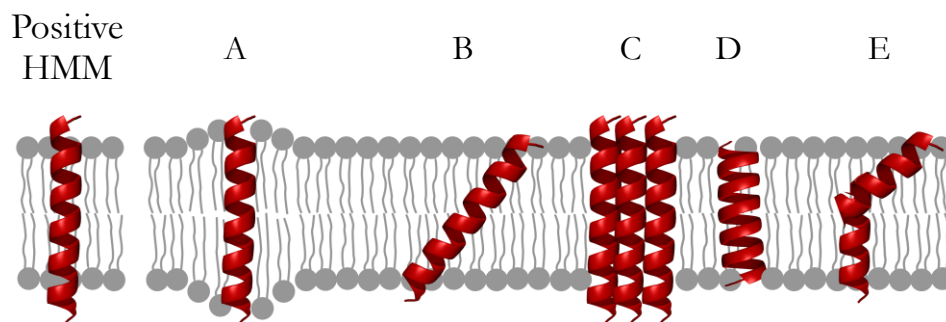


**Figure 4-1: Illustration of Possible Reactions to Hydrophobic Mismatch**

*Illustration of possible reaction mechanisms for the case when the helix's hydrophobic length is exceeding the hydrophobic thickness of the lipid bilayer, also known as positive hydrophobic mismatch (HMM), adapted from reference<sup>179</sup> A: Stretching of the lipids acyl chains. B: Tilting of the helix. C: Aggregation of helices. D: Distortion/deformation of the helix backbone E: Kinking of the backbone*

Alternatively, the helix can minimize the contacts between hydrophobic and hydrophilic elements by tilting, aggregation, compression or kinking (Figure 4-1, B-E). As natural membranes have a very complex composition of lipids varying in their hydrophobic length, helices or

lipids may also migrate to regions of hydrophobic matching. This concept has been a target for biophysical studies ever since,<sup>169, 171, 180</sup> including FRET, EPR and NMR spectroscopy studying transmembrane helices organization, revealing tilt angles, as well as folding and oligomerization processes of transmembrane peptide under HMM conditions.<sup>172, 181, 182</sup>

For studying the fundamental principles of this interaction several model systems have been developed. KILLIAN *et al.* introduced a model transmembrane peptide class called WALP (tryptophan (W) alanine (A) leucine (L) peptides).<sup>183</sup> The peptides are composed of a hydrophobic central stretch, of alternating alanines and leucines, which is flanked by tryptophans, serving as an anchor to the hydrophobic-hydrophilic lipid interface.<sup>184, 185</sup> Membrane embedded WALPs have been targeted by numerous studies, including fluorescence and NMR for determination of their tilt angles.<sup>186, 187</sup> WALP peptides have also been shown to be a valuable model system for distance measurements in lipid bilayers. EPR distances measurements showed the stability and good adaptation in lipid bilayers of WALP peptides in conjunction with nitroxide spin labels and also with more bulky labels such as lanthanide chelates.<sup>188, 189</sup> However it should be noted that the data quality of PELDOR experiments performed in lipid bilayers is usually fairly poor, when compared to solution. Fast relaxation, due to high local spin concentrations leads to low signal intensity, and interactions between the spin label and the lipid environment may alter the observed distance distribution. Hence suited spin labelling and experimental setup are fundamental to improve the applicability of PELDOR/DEER experiments in lipid bilayers.<sup>190</sup>

A WALP24 transmembrane peptide spin labelled with **TOPP** or **MTSSL** (Figure 3-5) for comparison is used to measure inter-spin distances in lipid bilayers. The signal intensity of the detected echo is strongly reduced due to the enhanced relaxation, triggered by spin-spin interactions, within the lipid bilayer. Additionally interactions between lipids and the nitroxides might influence the experimental distance distribution. TOPP's rigidity can potentially overcome the latter, but leaves the experiments prone to orientation selection.

## 5. Chapter

### General Experimental Setup for PELDOR Experiments Reported in this Thesis

A simplified scheme of a pulsed EPR spectrometer is given in Figure 5-1. Continuous wave microwave irradiation in the mW range is generated by the microwave (mw) source (Gunn diode). Figure 5-1 displays two sources (1 and 2) enabling the performance of double frequency experiments like PELDOR/DEER. The irradiation generated by the sources is passing the pulse-forming unit (PFU). Source 1 additionally feeds the reference arm, which serves as a bias and as a reference for frequency and phase in the mixer-based detection unit (quadrature detector and video amplifier). High microwave power is essential in pulse EPR as, in contrast to cw-EPR, excitation is non-selective. The available microwave power will also determine the microwave field  $B_1$  generated at the sample and therefore the pulse length  $t_p$  required for flipping the magnetization according to:  $\alpha = -\gamma_e |B_1| t_p$  ( $\alpha$  is the flip angle and  $\gamma_e$  the gyromagnetic ratio).<sup>191</sup> Therefore pulse sequences generated by the PFU are combined and send to an amplifier. The microwave power can be adjusted to the experimental needs by attenuation before entering the resonator. The echo-signal generated in the resonator is amplified again before entering the double balanced mixer-based quadrature detector that ensures a matching of the reference microwave phase to the phase of the signal. In case of a dual frequency experiment like PELDOR/DEER, detection is adjusted only



to the phase of the microwave generated in mw source 1, while pulses generated by the second source exhibit a random phase.

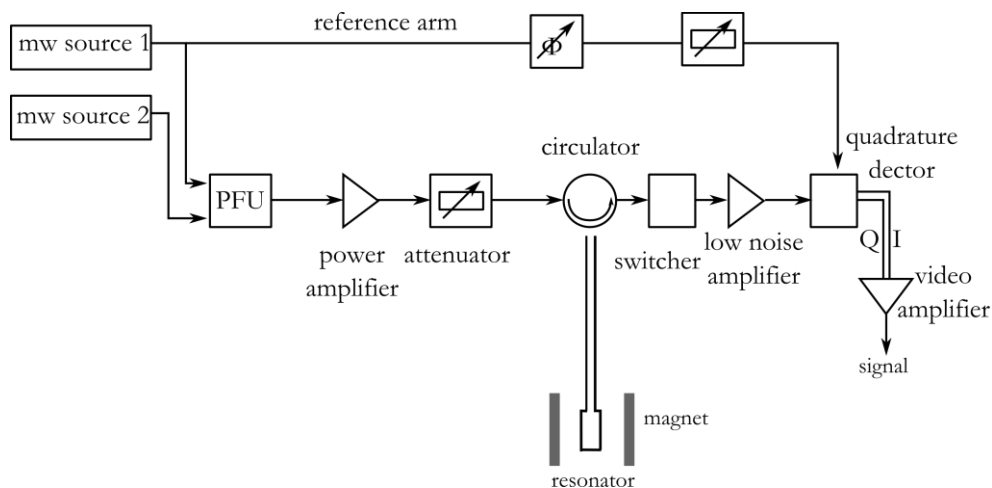


**Figure 5-1: Simplified Scheme of a Pulsed EPR Spectrometer**

*Adapted from<sup>191</sup>. Scheme of a pulsed EPR spectrometer with two microwave sources 1 and 2.*

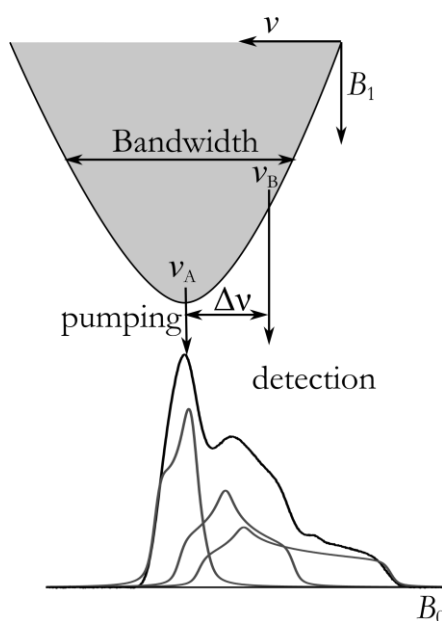
This incoherence is essential to suppress artefacts as explained in § 2.2.1. In the last step a video amplifier adjusts the signal to the input range of the analog-to-digital converter. To avoid damaging the receiver by the high power of reflected pulses a pin diode switcher blocks the pulses for the time until the so-called ringing appearing after pulse excitation of the pulse has decayed (defence pulse).

In this thesis all distance measurements were performed on a commercial Bruker ElexSys E580 pulse X/Q-band spectrometer. The instrument was initially equipped with a 3 W Q-band solid-state amplifier and later upgraded with a pulsed 170 W Q-band travelling-wave tube (TWT) amplifier (Model 187Ka, Applied Systems Engineering Inc.). However due to losses the power output of the microwave bridge was

measured to be around 50-55 W with the high power TWT amplifier. In measurements performed with the 3 W amplifier, the standard Q-band Bruker resonator (EN5107D2) was employed, which allows for insertion of EPR tubes with 2 mm outer diameter. Under strong overcoupling condition the resonator usually gave a bandwidth of around 100 MHz. At the centre of the dip,  $\pi$ -pulse length was typically 48 ns. 50 MHz frequency separation  $\Delta\nu$  between pump and detection frequencies could be achieved, without a critical loss of sensitivity, giving a  $\pi$ -pulse length of 56 ns. The same EN5107D2 Bruker resonator delivered a typical  $\pi$ -pulse length of 12 ns at the centre of the dip, when high power microwave irradiation was used. For distance measurements where sensitivity was crucial (small signal intensity), the Bruker ER5107QT-II resonator was employed.

**Figure 5-2: Resonator Dip and PELDOR Setup**

The top shows the schematic representation of a resonator dip (grey). The highest  $B_1$  is achieved in the centre. The bandwidth (full width at half maximum) of the resonator determines the maximum frequency separation available for the PELDOR/DEER experiment. Strong overcoupling was performed to increase the possible frequency separation. For maximum modulation depth PELDOR/DEER experiments are generally performed with the centre of the dip tuned for pumping at the maximum of the EPR spectrum (nitroxide EPR spectrum is plotted at the bottom). Detection is chosen at higher  $B_0$  values (lower frequencies).



The high-power setup with this resonator allows for measurements on larger sample volumes (3 mm outer diameter), thus increasing the

sensitivity. The Bruker ER5107QT-II resonator gives a typical  $\pi$ -pulse length of 16-18 ns when frequency was tuned in the dip centre of the microwave resonator. In this case pulse length of 26-28 ns were achieved when the frequency was set 90 MHz lower. Experimental temperature was adjusted to 50 K using a continuous flow cryostat (CF95550, Oxford Instruments). Figure 5-2 displays the echo-detected EPR spectrum of a representative nitroxide ( $C^T$  in RNA) recorded at 34 GHz and corresponding EasySpin simulations displaying the individual hyperfine lines.<sup>192</sup> The  $m_I = +1$  hyperfine line (low field side) results in the smallest anisotropy (highest intensity). For maximum excitation, normally the pumping frequency was set in the resonator dip centre and at the maximum of the EPR spectrum as also proposed by others.<sup>144, 146, 193</sup> The PELDOR/DEER setup was chosen for detection as close as possible to the pump frequency to reach optimal signal-to-noise but guarantying minimal spectral overlap of the pulses, resulting in a shift  $\Delta\nu$  of 50 or 90 MHz for the low and high power setup, respectively. The four-pulse PEDLOR/DEER sequence was employed for all PELDOR/DEER experiments. Figure 5-3 displays the general pulse setting generally employed in this work. All PELDOR/DEER experiments were run from tables that allow to adjust the timing for every pulse. The time delays  $\tau$  (250–400 ns) and  $T$  were adjusted for each experiment and are given in § 6 and 7. Independent from these two time delays the first pump pulse was always applied 60-98 ns after the second detection pulse, with the last pulse applied at 60-98 ns before the third detection pulse. For an unresolved reason, artefacts are introduced if this delay is chosen larger than 100 ns. The acquisition window was adjusted to the signal intensity of the detected echo.

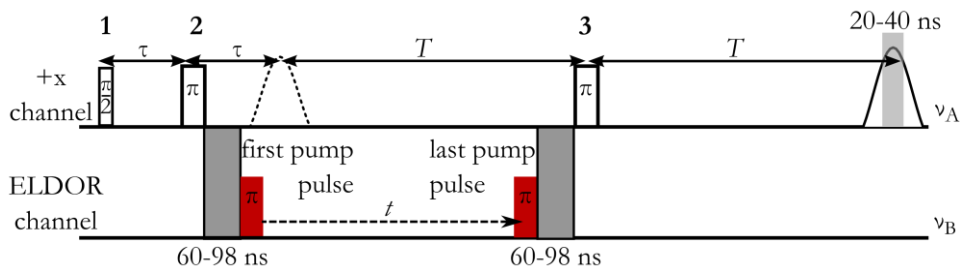


**Figure 5-3: General Pulse Sequence for PELDOR/DEER Experiments**

*Four-pulse PELDOR/DEER sequence as applied in this thesis. The detection pulses 1-3 are set in the  $+x$  channel. Time delays  $\tau$  and  $T$  are adjusted for each experiment. The pump pulse is set in the ELDOR channel, making sure that the spacing between detection pulse 2 and the first ELDOR pulse as well as the between the last pump pulse and detection pulse 3, does neither exceed 100 ns nor is too small, avoiding the simultaneous application of pulses.*

While around 40 ns of echoes of large intensity were integrated, this window was reduced to around 20 ns when the echo was weak in intensity to reduce noise. It turned out, that the incoherence of the ELDOR channel was sufficient to suppress artefacts from additional echoes and phase cycling is not required.

## 6. Chapter

### PELDOR on C<sup>T</sup>-Labelled Ribonucleic Acid

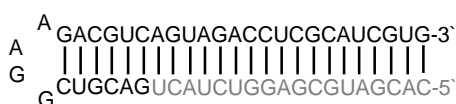
#### – Measurement of Long Distances

The following chapter will analyse the results obtained in the experiments on C<sup>T</sup>-labelled RNA. Not only the experimental distances and their distributions but also an investigation of orientation selectivity will be presented. Additionally, the influence of uncertainties in the background correction on the error of the extracted distances will be discussed. The results are published in *chemical science* and some of the figures are adapted from the publication.<sup>194</sup>

### 6.1 Materials and Methods

The RNA sequence for labelling is shown in Figure 6-1 (black), with its complementary strand being displayed in grey.

hairpin conformation



duplex conformation

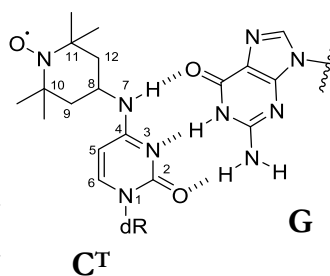


Figure 6-1: RNA Sequence and C<sup>T</sup> Spin Label

Left: The 34 base-pair RNA duplex and hairpin employed in this study. Right: Chemical structure of the N<sup>4</sup>-TEMPO-cytidine (C<sup>T</sup>) spin label illustrating the base pairing with guanine.

The N<sup>4</sup>-TEMPO-cytidine (**C<sup>T</sup>**) spin label preserves the base-pairing capability of cytosine (**C**) to guanine (**G**), as shown in Figure 6-1. Samples for EPR spectroscopy were received from Jan Seikowski from the laboratory of Professor Claudia Höbartner (Georg August University, Göttingen) in the following form: Spin-labelled 34 nucleotide RNA strands were annealed with 1.5 equivalents of the 34 nucleotide complementary strand to form the duplex samples. To form a hairpin containing a GGAA tetra loop and a nicked extended stem, 1.5 equivalents of the 18 nucleotide long RNA complement to the 3'-part were added. Annealing was performed in 10 mM potassium phosphate/D<sub>2</sub>O buffer pH 7.0, containing 150 mM NaCl. Overall 8 samples differing in label positions were investigated.

**Table i**

*Sequences of the RNA strands with C<sup>T</sup> marked as bold. Sample numbering, number of base pairs Δbp between the labels*

Sample	Δbp	Sequence
<b>1</b> Duplex [6,16]	10	GACGUC <b>C<sup>T</sup></b> GGAAGACGUC <b>C<sup>T</sup></b> AGUAGACCUCGCAUCGUG
<b>2</b> Duplex [13,28]	15	GACGUCGGAAGAC <b>C<sup>T</sup></b> GUCAGUAGACCUCG <b>C<sup>T</sup></b> AUCGUG
<b>3</b> Duplex [16,31]	15	GACGUCGGAAGACGUC <b>C<sup>T</sup></b> AGUAGACCUCGCAUC <b>C<sup>T</sup></b> GUG
<b>4</b> Duplex [6,24]	18	GACGUC <b>C<sup>T</sup></b> GGAAGACGUCAGUAGACC <b>C<sup>T</sup></b> UCGCAUCGUG
<b>5</b> Hairpin [6,28]	18	GACGUC <b>C<sup>T</sup></b> GGAAGACGUCAGUAGACCUCG <b>C<sup>T</sup></b> AUCGUG
<b>6</b> Duplex [6,28]	22	GACGUC <b>C<sup>T</sup></b> GGAAGACGUCAGUAGACCUCG <b>C<sup>T</sup></b> AUCGUG
<b>7</b> Duplex [6,31]	25	GACGUC <b>C<sup>T</sup></b> GGAAGACGUCAGUAGACCUCGCAUC <b>C<sup>T</sup></b> GUG
<b>8</b> Duplex [3,31]	28	GAC <b>C<sup>T</sup></b> GUCGGAAGACGUCAGUAGACCUCGCAUC <b>C<sup>T</sup></b> GUG

### 6.1.1 Preparation of EPR Samples

#### *Determination of Labelling Efficiency*

For characterizing the spin-labelling efficiency cw-EPR spectra were recorded at X-band frequencies. Experiments were performed at room temperature in a Bruker Elexsys E500 spectrometer equipped with a Bruker super high Q resonator ER4122SHQE. 20  $\mu\text{L}$  of RNA sample were filled into EPR glass capillaries of 2 mm outer diameter (OD).

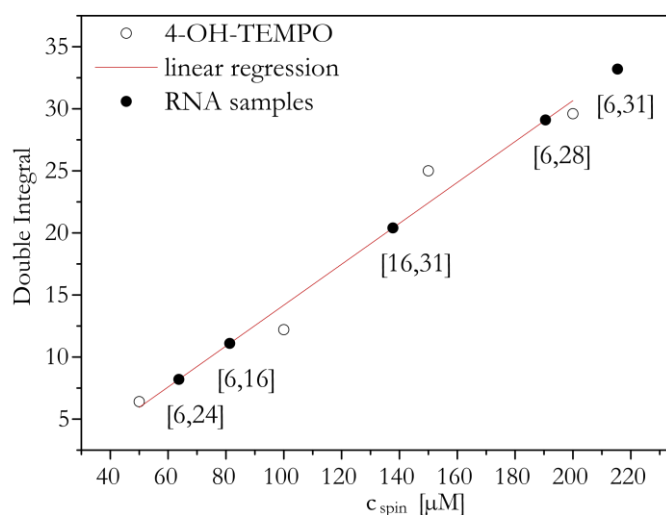


**Figure 6-2: Determination of the RNA Samples' Spin Concentration**

*Double integral was calculated from cw-EPR spectra recorded at X-band microwave frequencies (9,7 GHz). A calibration curve was obtained from measuring 4-hydroxy TEMPO in the RNA samples' buffer at concentrations between 50 and 200  $\mu\text{M}$  (open dots). Linear regression (red line) of the calibration curve enabled the calculation of the spin concentrations from double integrated EPR spectra of the RNA samples (black dots).*

Comparison of the doubly integrated EPR signal with a calibration curve, recorded with 4-hydroxy TEMPO at concentrations between 50 and 200  $\mu\text{M}$ , was used to calculate the spin concentration (Figure 6-2).

Comparison of the measured spin concentration with the nominal RNA concentration determined by UV absorbance revealed labelling efficiencies between 80 and 100 % for all samples.

### *EPR Sample Preparation*

Glycerol was added (20-50 % of the final volume) to samples for PELDOR/DEER yielding a final concentration of spin-labelled RNA between 40 and 60  $\mu\text{M}$  (Table ii). Samples with long inter spin distances ( $r \geq 5$  nm) contained D8-glycerol, to increase the transverse relaxation time  $T_m$ .

**Table ii**

*Concentration of spin labelled RNA duplex for PELDOR*

<b>Sample</b>		<b>c [<math>\mu\text{M}</math>]</b>
<b>1</b>	Duplex [6,16]	40
<b>2</b>	Duplex [13,28]	50
<b>3</b>	Duplex [16,31]	50
<b>4</b>	Duplex [6,24]	60
<b>5</b>	Hairpin [6,28]	40
<b>6</b>	Duplex [6,28]	55
<b>7</b>	Duplex [6,31]	100
<b>8</b>	Duplex [3,31]	55

### **6.1.2 PELDOR/DEER Experiments**

PELDOR experiments were generally performed as described in § 5. Experiments using low power were performed using the EN5107D2



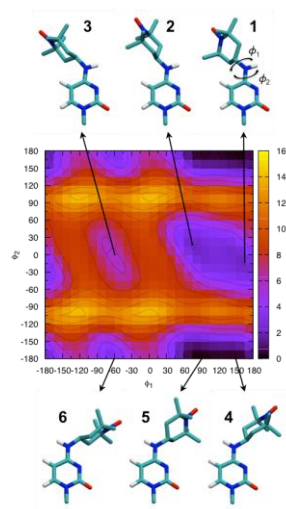
resonator (EPR tubes with 2 mm outer diameter) giving a  $\pi$ -pulse length of 48 ns for pumping at the dip centre and 56 ns for detecting 50 MHz lower in frequency. High power experiments on samples **1-6** were performed with the same resonator now giving a  $\pi$ -pulse length of 12 ns in the centre and 24 ns at 90 MHz lower frequency for pumping and detection, respectively. Sample **7** and **8** were measured using the ER5107QT-II resonator employing larger sample volumes (EPR tubes with 3 mm outer diameter). In this case  $\pi$ -pulse lengths were 16 ns in the dip centre and 24 ns or 26 ns at 90 MHz lower or higher frequencies, respectively. Experiments on sample **8** were performed with detection at the dip centre and at the maximum of the EPR line to increase the signal intensity. Pumping was performed at 90 MHz higher microwave frequency in this case. Experimental conditions that deviate from this setup are given in the figure captions. A time delay  $\tau$  of 400 ns was set between the first two pulses in the sequence. The dipolar evolution time  $T$  (spacing between second and third detection pulses) was set between 3.5 and 18  $\mu$ s, to enable recording at least 2.5 periods of dipolar oscillations for distances of up to 5 nm. Evolution time for longer distances was chosen to provide at least 1.5 modulations. The last 100 ns of the experimental time traces were removed as they usually contained artefacts from the pump pulse entering the third detection pulse. Acquisition time varied from  $\sim$  10 hours up to  $\sim$  24 hours, depending on the evolution time  $T$  of the PELDOR sequence. The intermolecular background was removed from dipolar traces, using a second order polynomial function for background correction. Tikhonov regularization, provided by the program DEERanalysis, was employed to derive distance distributions.

### 6.1.3 Construction of Molecular Model of C<sup>T</sup>-labelled RNA

Standard A-form RNA was constructed from the given sequence using the Web 3DNA server program.<sup>195</sup> Different conformations of the C<sup>T</sup> fragment arising from isomerization around the two rotatable bonds ( $\Phi_1$  and  $\Phi_2$ , Figure 6-3) were extracted from an *ab initio* scan of the C<sup>T</sup> fragment performed by Deniz Sezer.<sup>194</sup> As conformation 4-6 of Figure 6-3 interfere with the base pairing of C<sup>T</sup> to Guanine, only conformations 1 and 2 were considered as minimum structures.

**Figure 6-3: *Ab Initio* Scan of C<sup>T</sup> Conformations**

*Ab initio* scan of the dihedral ( $\phi_1$ - $\phi_2$ ) potential energy surface and conformations of the six local minima. Some hydrogen atoms are not shown for clarity. Taken from reference,<sup>194</sup> Although conformations 5 and 6 display the global energy minimum they were not considered in construction of the molecular model as they interfere with the base pairing.



The C<sup>T</sup> fragment in the desired conformation subsequently replaced cytosine in the modelled RNA duplex at the respective label positions (PyMOL, Delano Scientific LLC). Dihedrals ( $\Phi_1$  and  $\Phi_2$ ) of the six conformations are given in Table iii.

**Table iii**

*Energies and dihedral angles of the six optimal conformations of C<sup>T</sup> shown in Figure 6-3*

<b>Mimumum #</b>	<b>1</b>	<b>2</b>	<b>3</b>	<b>4</b>	<b>5</b>	<b>6</b>
Energy (kcal/mol)	1.96	1.96	5.49	0.00	0.00	2.55
Dihedral $\phi_1$ (degree)	162	77	-63	156	83	-63
Dihedral $\phi_2$ (degree)	-12	12	0	175	-175	180

#### **6.1.4 Simulation of Orientation Selective PELDOR Traces**

Simulations of orientation selective PELDOR/DEER traces for sample **2** were conducted using a home written program that takes into account orientation selection in PELDOR/DEER experiments.<sup>59, 62</sup> The simulations considered experimental parameters (pulse lengths, frequency separation, EPR detection frequency, nitroxide EPR parameters). The relative orientation between the two labels was extracted from C<sup>T</sup> labels, considering the two most populated states conformation **1** and **2** (Figure 6-3, Table iii), attached to position 13 and 28 in the standard A-form RNA as described in § 6.1.3. Time traces were simulated for the four pairs of label conformations arising from the combinations of the two conformations. The four pairs are denoted [13/1, 28/1], [13/2, 28/2], [13/1, 28/2] and [13/2, 28/1]. Relative population of the two conformations **1** and **2** was assumed as equal, for simplicity. The distance corresponding two the individual pair was

extracted from the ideal A-form RNA (each individual combination of conformations has a slightly different distance).

## 6.2 Results on $C^T$ -labelled RNA

This section will summarize the results of the PELDOR/DEER experiments on the  $C^T$ -labelled RNA. Not only results concerning long-range distance measurements between 3 and 8 nm in the RNA duplex will be presented, but also several experiments evaluating the accuracy of the extracted distances.

### 6.2.1 Examination of Orientation Selection

PELDOR/DEER measurements on samples **1-4** were performed under various conditions of pulse excitation bandwidths as well as excitation positions in the EPR line, to investigate the performance of the PELDOR/DEER experiment at Q-band frequency in conjunction with the  $C^T$  labels in terms of orientation selection. The full analysis will be presented for sample **2** as an example, which carries the  $C^T$  label at position 13 and 28 of the sequence. Figure 6-4 displays a comparison of PELDOR/DEER experiments on sample **2** performed with either the 3 W or the 170 W amplifier. The modulation depths  $\Delta$  observed in both experiments ( $\Delta \leq 0.1$  at low power vs.  $\Delta \leq 0.3$  at higher power) are consistent with narrow and wider excitation bandwidths. The trace recorded with selective pulses reflects frequency components due to orientation selection that give rise to an artificial peak in the distance distribution if not considered in analysis (marked by an arrow in Figure 6-4, A).

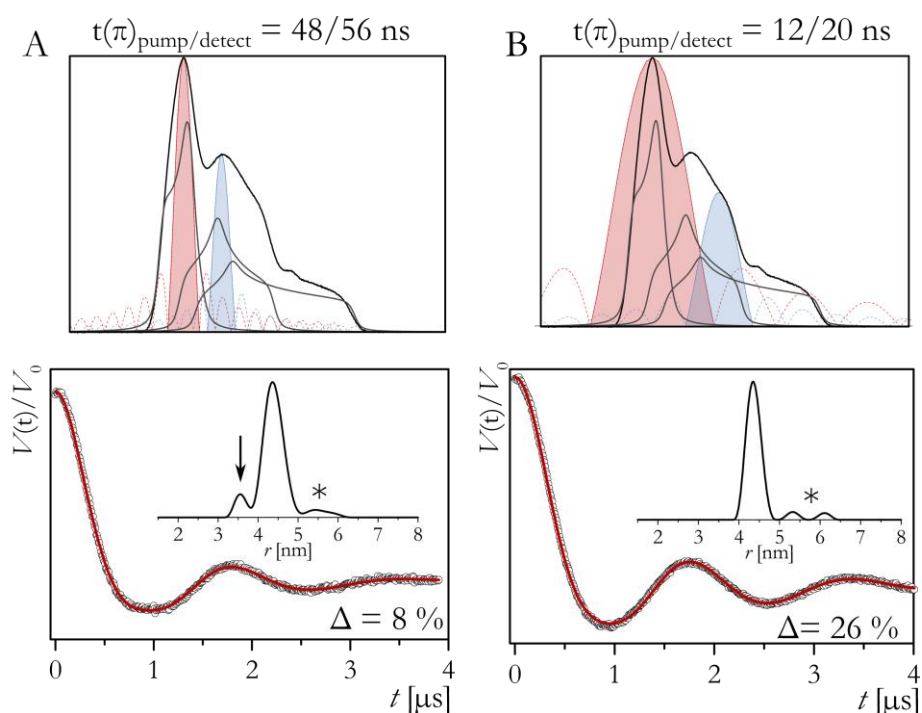


**Figure 6-4: Comparison of High and Low Power PELDOR Experiments**

Top (A,B): Echo-detected field-sweep nitroxide spectra recorded at  $Q$  band on sample **2** ([13,28] RNA duplex) and simulation illustrating the contributions of the three hyperfine transitions  $m_i = +1; 0; -1$ . Coloured lines illustrate pump- (red) and detect- (blue) pulse excitation profiles as sinc functions for low- (A) and high-power (B) setups. Bottom (A,B): Background corrected PELDOR/DEER traces (dots) and DEER analysis fits (red traces) corresponding to setup using selective pulses and a frequency separation of 50 MHz (A) and broadband excitation using a frequency separation of 90 MHz (B). Insets show corresponding distance distributions. Arrow marks an artefact due to orientation selection. Artefacts that are sensitive to background subtraction are marked by asterisks.

The assignment is proofed by the orientation selective experiments shown below. In contrast, the PELDOR/DEER trace recorded with broadband excitation does not exhibit orientation selection. The findings are supported by experiments and simulation of orientation selective PELDOR/DEER traces (Figure 6-8 - Figure 6-11). For experiments performed with the low power amplifier (selective pulses), six different

spectral positions for pumping and detection were chosen (Figure 6-5, left). The experimental time traces displayed in Figure 6-5 show a clear dependence on the spectral positions for pumping and detection.

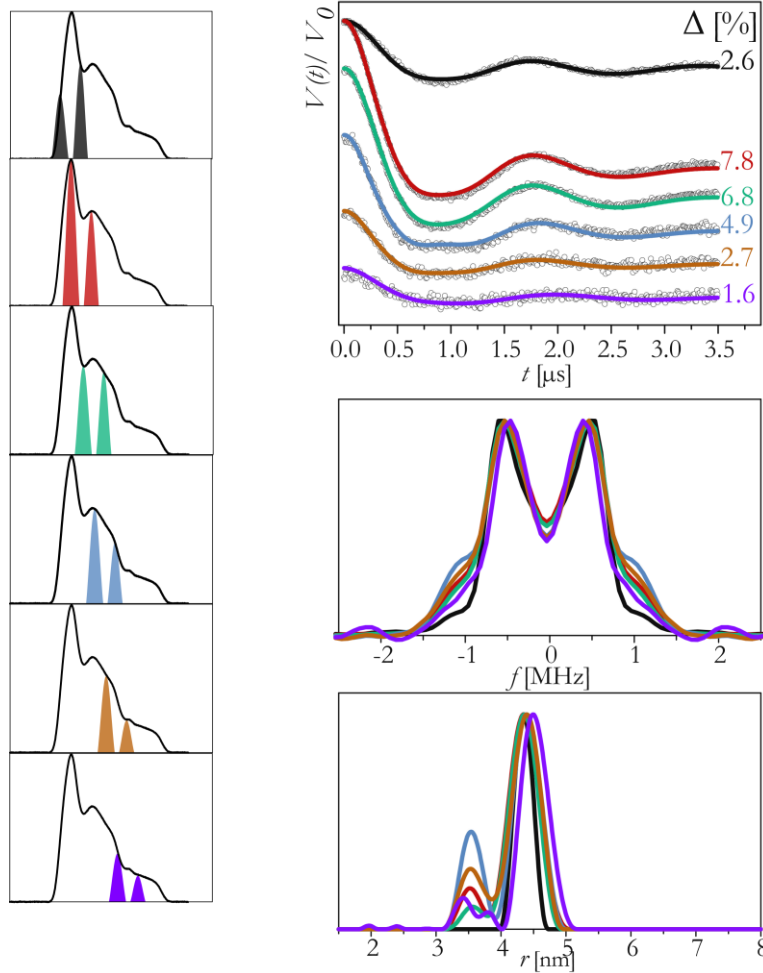


**Figure 6-5: Low-Power PELDOR Experiments Performed on Sample 2**

*PELDOR/DEER experiments performed with selective pulses (low power microwave amplification). Due to orientation selection effects, the resulting time traces and corresponding distance distributions show dependence on the experimental setup. Left: Spectral positions of the pump and detection pulses for selective excitation according to colour code. Right top: Experimental PELDOR/DEER traces and DEERanalysis fit and  $\Delta$  in per cent according to colour code. Right middle: Their Fourier transformations Right bottom: corresponding (artificial) distance distributions obtained with the program DEERanalysis on these traces.*

The effect can be best identified in the Fourier transformations of the traces, which show slightly distorted Pake patterns (Figure 6-5, right middle). It is important to note that the program DEERanalysis produces an artefact peak at lower distances, as it does not consider orientation selection. The intensity of this artificial peak, arising from the dipolar frequency component  $\nu_{\parallel}$ , does show a clear dependence on the experimental setup. It is most pronounced when pumping and detection positions are set around the centre of the EPR spectrum (Figure 6-5, blue), in this case the disproportionately large contribution of  $\nu_{\parallel}$  can be identified even in the time trace. Changing the pump and detection positions cannot diminish the effect. A similar study was performed, investigating the dependence of the dipolar frequency extracted from PELDOR/DEER traces recorded with broadband excitation. Figure 6-6 displays PELDOR/DEER traces recorded when pumping at the maximum of the nitroxide's EPR spectrum and detecting at 70-130 MHz lower microwave frequency. In this case no dependence of the distribution of the dipolar frequency is observed, as best seen by comparing the Fourier transformations of the four traces (Figure 6-6, right middle). The distance distributions obtained from DEERanalysis fit of the individual traces show no differences or artificial peaks (Figure 6-6, right bottom).

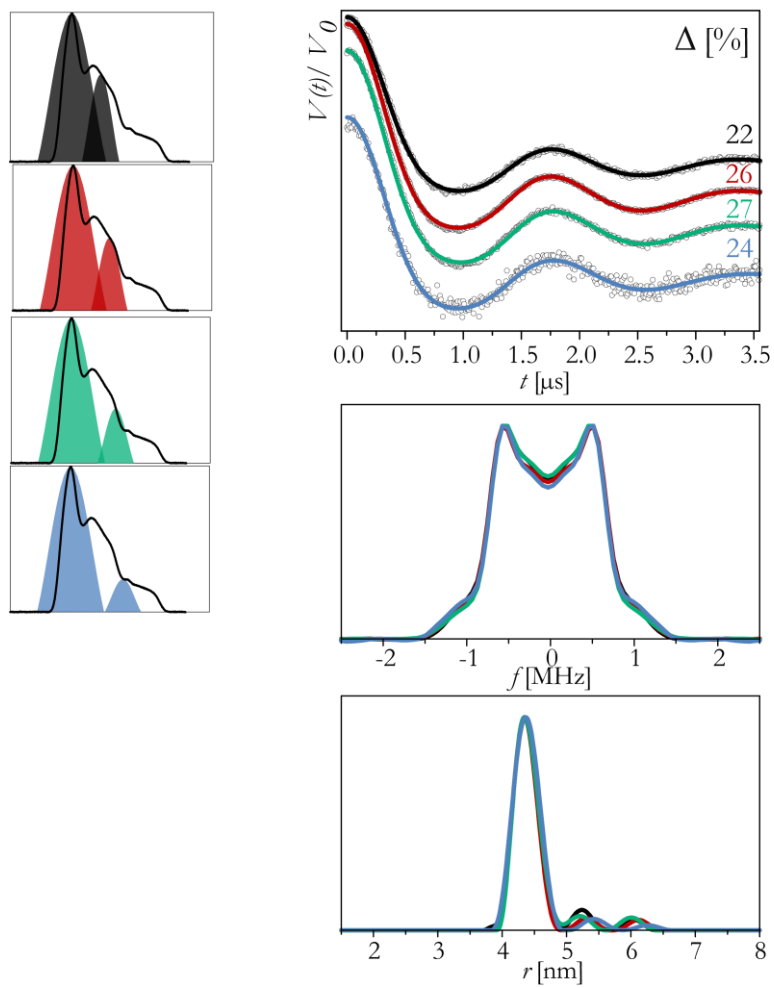


**Figure 6-6: High-Power PELDOR Experiments Performed on Sample 2**

PELDOR/DEER experiments performed with broadband excitation (low power microwave amplification). No orientation selection effects are observed. Left: Spectral positions of the pump and detection pulses for selective excitation according to colour code. Right top: Experimental PELDOR/DEER traces and DEERanalysis fit and  $\Delta$  in per cent according to colour code. Right middle: Their Fourier transformations Right bottom: corresponding distance distributions obtained with the program DEERanalysis on these traces.



Orientation selective simulations were conducted for four pairs of  $C^T$  conformations, corresponding to combinations of the most populated conformations **1** and **2** at both label positions (Figure 6-7) with their associated distance (described in § 6.1.3). All four combinations ([13/1, 28/1], [13/2, 28/2], [13/1, 28/2] and [13/2, 28/1]) generate a series of time traces for the set of experimental setups.

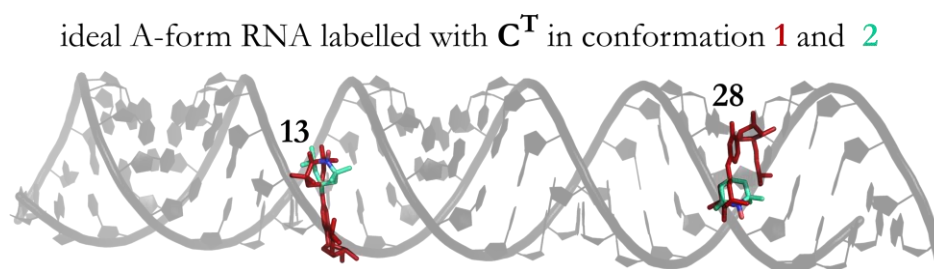


**Figure 6-7: Model of Sample 2 with  $C^T$  in Conformation 1 and 2**

*Schematic structure of the 34 base-pair RNA sample 2 (standard A-form) constructed with PyMOL. Labels are inserted in conformation **1** (red) and **2** (light cyan) with the dihedrals reported in Table iii.*

The traces simulated with the excitation bandwidth achieved with the 3 W amplifier show considerable dependence of the dipolar frequency on the chosen spectral positions (Figure 6-8, bottom) and the mutual orientation of the labels.

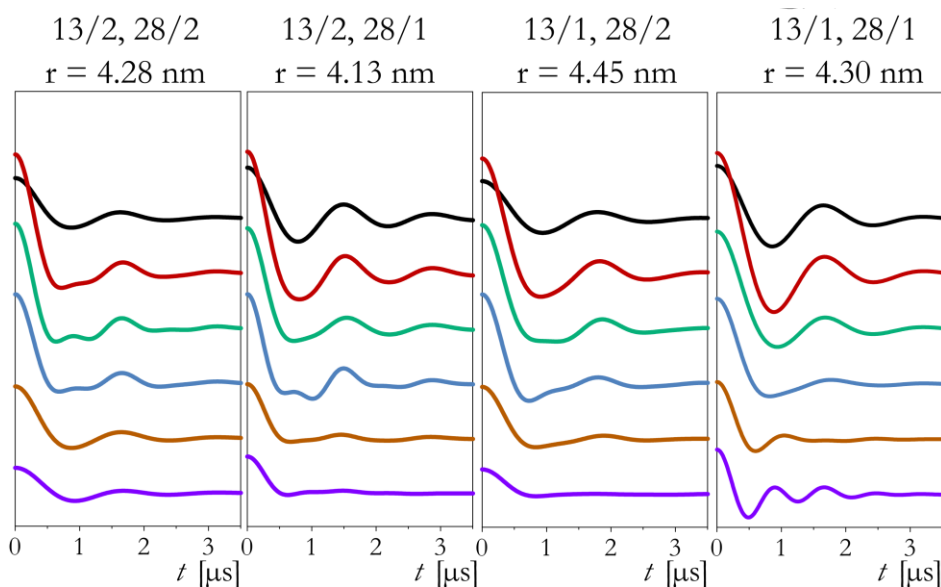


**Figure 6-8: Low-Power PELDOR Traces Simulated for Sample 2**

*Simulated time traces for four different label pairs arising from the combinations of the two most populated conformations **1** and **2** of the label, using the experimental parameters of Figure 6-5 and the distances corresponding to the label pair in the individual ideal A-form RNA. The four conformations are labelled [13/1, 28/1], [13/2, 28/2], [13/1, 28/2] and [13/2, 28/1]. Each individual conformation has a slightly different distance as indicated in the top of the figures.*

The combination of labels at position 13 and 28 in conformation **1** for example results in simulated time traces that show the largest contribution of  $\nu_{\parallel}$  when pumping and detecting at the high field side of the EPR line (Figure 6-8, right, violet trace). In contrast traces simulated with labels at both positions in conformation **2** will show the largest contribution of  $\nu_{\parallel}$  when pumping and detecting in the centre of the EPR spectrum (Figure 6-8, right, green and blue trace). If simulations are conducted under broadband excitation conditions (high power), the dependence of the dipolar frequency visible in the individual traces, is way less pronounced than in the low power simulation (Figure 6-9).

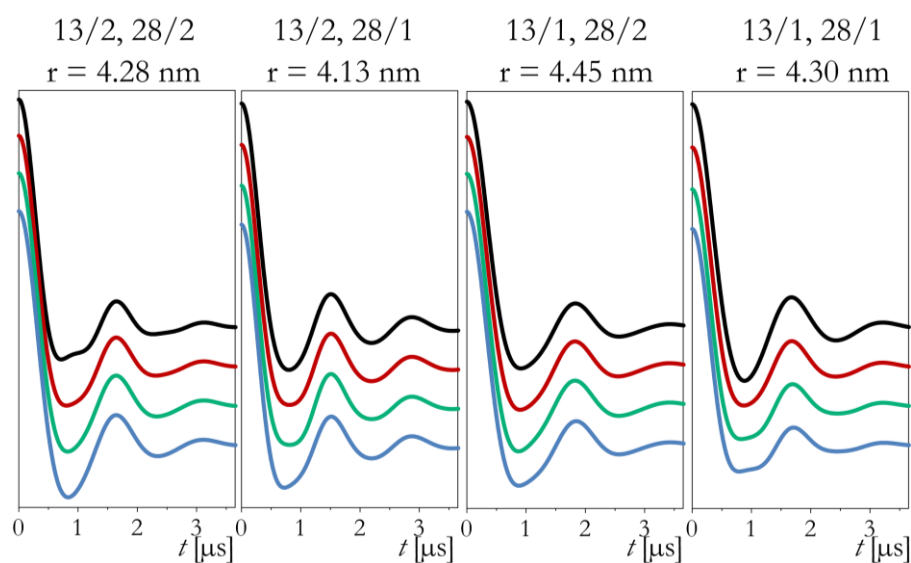


**Figure 6-9: High-Power PELDOR Traces Simulated for Sample 2**

*Simulated time traces for four different label pairs arising from the combinations of the two most populated conformations 1 and 2 of the label, using the experimental parameters of Figure 6-6 and the distances corresponding to the label pair in the individual ideal A-form RNA. The four conformations are labelled [13/1, 28/1], [13/2, 28/2], [13/1, 28/2] and [13/2, 28/1]. Each individual conformation has a slightly different distance as indicated in the top of the figures.*

For comparison with the experimental PELDOR/DEER traces of all four pairs were summed up for each spectral positions, to account for a possible conformational distribution. The results for the case of selective pulses (low power) are summarized in Figure 6-10. Both, the experimental time traces and the summed simulated time traces result show clear dependence on the spectral positions for pumping and detection. The Fourier transformations of the traces show slightly distorted dipolar Pake patterns, distinguished for every experimental setup (Figure 6-10, middle). Overall the predicted orientation selection is in very good qualitative agreement with the shape of the traces. However, the high field trace (violet) seems to overestimate the contribution of  $\nu_{\parallel}$  if the four simulations are summed with equal

probability. Qualitatively the experimental traces are better reproduced by conformation [13/2, 28/2], suggesting that this conformation is more populated. A further improvement in the simulation of the orientation selectivity would require a more detailed analysis of the individual contributions and more precise orientation selection at higher frequency, which goes beyond the scope of this work.

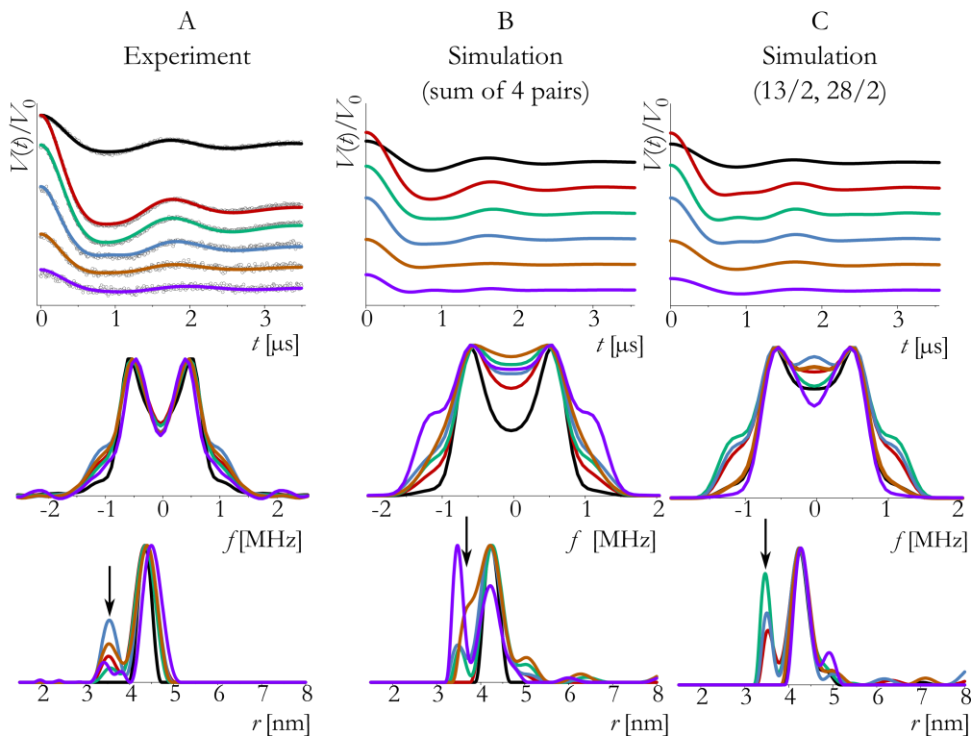


**Figure 6-10: Low-Power PELDOR Traces on Sample 2: Simulation vs. Experiments**

*Left (top to bottom): Experimental PELDOR/DEER traces, their Fourier transformations (Pake patterns) and corresponding (artificial) distance distributions obtained with the program DEERanalysis on these traces. Centre (top to bottom): Sum of simulated time traces of the four label pairs, their Fourier transformations (Pake patterns) and artificial distance distributions from DEERanalysis. Right (top to bottom): Comparison with simulated time traces for the pair having both labels in conformation 2, their Fourier transformations (Pake patterns) and artificial distance distributions obtained with DEERanalysis.*

The same comparison is shown for broadband excitation (Figure 6-11).

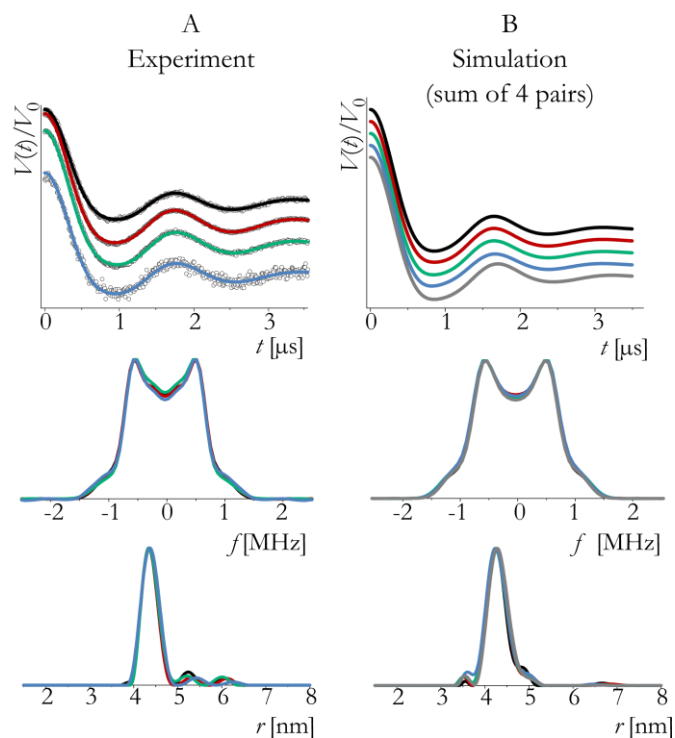


**Figure 6-11: High-Power PELDOR Traces on Sample 2: Simulation vs. Experiments**

*Left: experimental PELDOR/DEER traces, their Fourier transformations (Pake patterns) and corresponding distance distributions obtained with the program DEERanalysis on these traces. Right: Sum of the simulated time traces of the four label pair conformations, their Fourier transformations (Pake patterns) and corresponding distance distributions from DEERanalysis. The grey coloured line displays a simulation with full excitation of the nitroxide's EPR spectrum for comparison, but no differences are observed. The results best illustrate the effective suppression of orientation selective effects with broadband excitation*

If the traces of the four pairs are summed, no dependence of the dipolar frequency is observed, which is in agreement with the experimental results. A comparison of the traces simulated for the experimental setup (excitation bandwidth and spectral positions) with a simulation with full excitation (grey line, Figure 6-11) does evidence that there is no residue orientation selection. In this case, also the program DEERanalysis well reproduces the dipolar oscillation with only one

frequency contribution and results in a narrow ( $\Delta r = \pm 0.2$  nm) distribution width. Also on three other samples with spin labels at other positions in the sequence, no dependence of the dipolar frequency on the experimental setup could be observed under broadband excitation conditions (Figure 6-12).

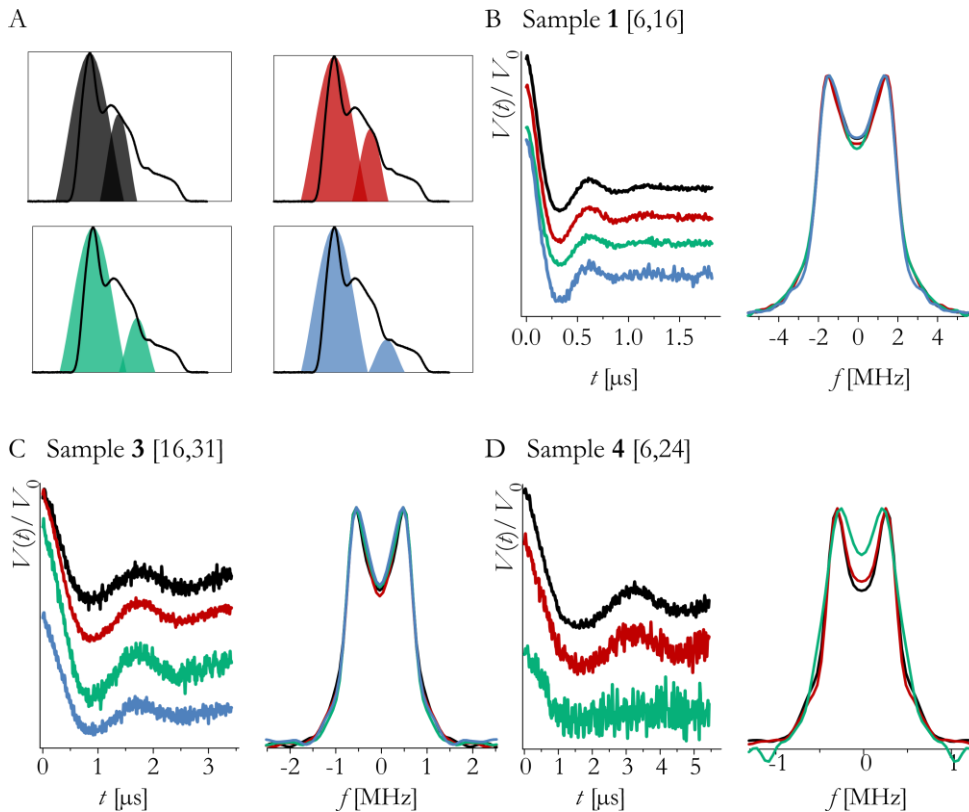


**Figure 6-12: High-Power PELDOR on Samples 1-4**

*A: Experimental echo detected field-sweeps (black line) with spectral position for pumping at the maximum of the EPR spectrum and detecting 70-150 MHz lower in frequency (higher field value). Excitation bandwidths are according to pulse lengths of 12 ns for pumping and 24 ns for detection. B-C: Background-corrected high-power Q-band PELDOR/DEER traces recorded on RNA samples **1**, **3**, and **5** and their corresponding Pake patterns from Fourier transformation.*

The results proof that orientation selection arising from C<sup>T</sup>'s restricted mobility are suppressed if broadband excitation (high microwave power) is applied.

### 6.2.2 Long-Range Distance Measurements

To inspect the capability of the Q-band PELDOR/DEER experiments on C<sup>T</sup> labelled RNA for a wide range of distances, experiments were performed on the eight samples introduced in Table i. To suppress orientation selection artefacts all traces were recorded under broadband excitation. The resulting time traces and distance distributions obtained from the analysis are summarized in Figure 6-13. The trace recorded on sample **1** with the label positions 6 and 16 (base-pair separation  $\Delta\text{bp} = 10$ ) shows a considerable enhancement in signal-to-noise ratio ( $\geq 10$ ) when compared to an earlier X-band PELDOR/DEER study on a 20 bp duplex C<sup>T</sup> labelled at the same position.<sup>115</sup> This increase in sensitivity is expected from the frequency dependence of PELDOR/DEER performance if experimental conditions are comparable (§ 4.1).<sup>146</sup> According to the analysis, a single Gaussian peak now replaces the asymmetry of the distance distribution extracted from the X-band experiments. Artefact peaks arising from ESEEM effects disappear. However, the distance and its distribution observed in the X-band study are reproduced ( $r = 3.1 \text{ nm}$   $\Delta r = \pm 0.2 \text{ nm}$ ,  $\Delta r$  defined as half width at half height). The samples **2** and **3** carry the nitroxides at cytosine positions separated by 15 base pairs, but the C<sup>T</sup> nucleotides reside in a different sequence environment (i.e. C<sup>T</sup> is flanked by different nucleotides).

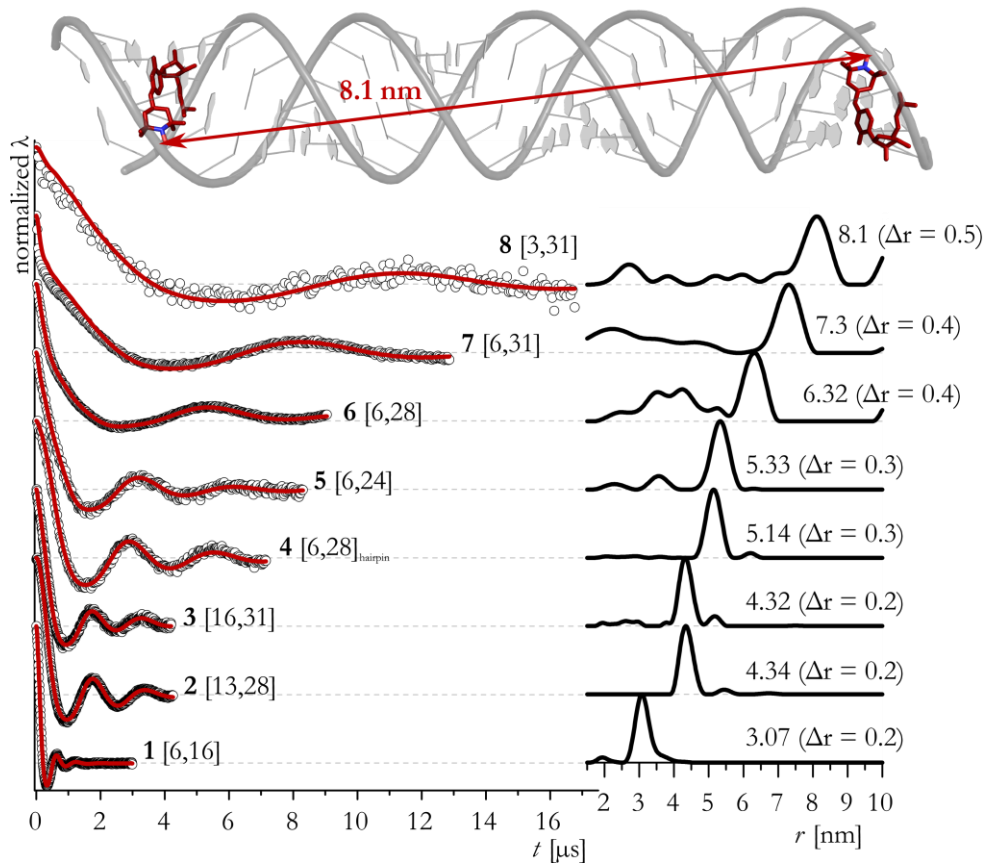


**Figure 6-13: Experimental PELDOR Traces and Distance Distributions of  $C^T$ -Labelled RNA**

Background corrected PELDOR/DEER traces recorded at  $Q$  band with broadband excitation (dots) of the 34 bp RNA duplex and hairpin, samples **1-8**, DEER analysis fits (red lines) and distance distributions in the inset. Experimental conditions: samples **1-6**:  $\Delta\nu = 90$  MHz,  $t(\pi, \text{pump}) = 12$  ns,  $t(\pi, \text{detect}) = 24$  ns; sample **7**:  $\Delta\nu = 90$  MHz,  $t(\pi, \text{pump}) = 16$  ns,  $t(\pi, \text{detect}) = 24$  ns. sample **8**:  $\Delta\nu = -90$  MHz,  $t(\pi, \text{pump}) = 26$  ns,  $t(\pi, \text{detect}) = 16$  ns. Time traces are shown with normalized intensity and modulation depth. Modulation depths were between 20 and 30 % for samples **1-7** and 10 % for sample **8**. Upper inset: Structure of the 34 bp RNA duplex (standard A-form)  $C^T$  labelled at positions 3 and 31 (sample **8**) generated with PyMOL. The structure illustrates the orientation of the  $C^T$  labels towards the inside of the duplex. Labels were inserted with dihedral angles of  $\phi_1 = 77^\circ$  (C4, N7, C8, C9) and  $\phi_2 = 11^\circ$  (C5, C4, N7, C8), (conformation **2**, Figure 6-3).

For both samples the experimental traces showed a clear oscillation resulting in a narrow, single, one-peak inter spin distance of 4.3 nm ( $\Delta r$



= 0.2 nm). Also distances on the order of 5 nm gave rise to sharp oscillations in the time traces recorded on samples **4** and **5**, which are labelled at cytosines being 18 base pairs apart. The obtained distance distribution is again very sharp, though slightly increasing to  $\Delta r = \pm 0.3$  nm. A 1.9 Å difference in the peak distance between the two samples is resolved in the dipolar oscillation frequency due to the fact that distributions are still narrow at this length scale. To confirm the analysis longer representative traces were recorded on sample **2** and **5** (Figure 6-14). The distances and distributions were confirmed giving confidence that the trace length chosen for the PELDOR/DEER experiments displayed in Figure 6-13 is sufficient for data analysis.

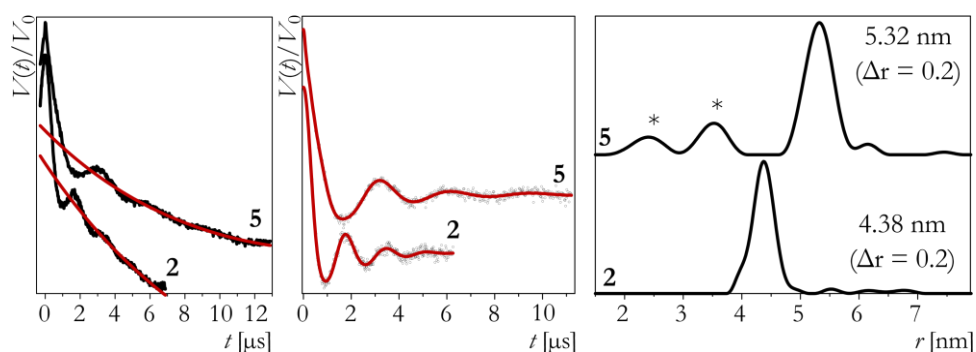


**Figure 6-14: PELDOR Traces with Longer Evolution Time for Sample 2 and 5**

*Time traces with a longer evolution time  $T$  of 7 and 13  $\mu$ s were recorded for samples **2** and **5** to evaluate the uncertainty in the distance distribution. A second order polynomial fitted to about the last 50 % of the traces was chosen for background correction (left). The distance distributions (right) obtained from DEERanalysis fit (middle) did not show any difference in  $\Delta r$  when compared to experiments recorded with an evolution time covering 2.5 oscillations (Figure 6-13). The signal-to-noise however is decreased due to the larger acquisition window. Asterisks in the distance distribution (right) denote additional frequency components that likely arise from aggregates (compare Figure 6-16).*

Owing the low dipolar frequency only one and a half full modulation periods could be recorded on samples **6-8**. Fitting of the traces resulted

in clear main peaks. However the error in the peak distance increases to approximately  $\pm 0.1$  nm due to uncertainties in the background correction as illustrated in § 6.2.3. The uncertainty also affects the determination of the distance distribution, which is now given as  $\Delta r \leq \pm 0.5$  nm. Table iv summarizes the observed distances and distributions. The experimental distances show a very good agreement with the distances between the two spin labels (average between O-O, N-N, O-N and N-O distances) that were extracted from a simple molecular model of the ideal A-form RNA.<sup>195</sup>

**Table iv**

*Experimental distances and distributions compared to estimated distances from a standard A-form RNA. The experimental error in the peak distance is much less than the distribution  $\Delta r$  and is estimated up to  $\pm 0.1$  nm (§ 6.2.3). Estimated distances are average of O-O, N-N, O-N and N-O distances. \*Hairpin distance was extracted from a model that contained only the double-stranded helix part of the hairpin, without the loop.*

sample	$\Delta bp$	distance [nm]		
		PELDOR		Model A-form RNA
		r	$\Delta r$	r
1 [6,16] <sub>duplex</sub>	10	3.07	0.2	2.82
2 [13,28] <sub>duplex</sub>	15	4.34	0.2	4.28
3 [16,31] <sub>duplex</sub>	15	4.32	0.2	4.28
4 [6,28] <sub>hairpin</sub>	18	5.14	0.3	5.11*
5 [6,24] <sub>duplex</sub>	18	5.33	0.3	5.11
6 [6,28] <sub>duplex</sub>	22	6.32	0.4	6.19
7 [6,31] <sub>duplex</sub>	25	7.3	0.4	7.06
8 [3,31] <sub>duplex</sub>	28	8.1	0.5	7.91

Figure 6-15 shows a plot of the experimental inter-spin distances against the corresponding base-pair separation  $\Delta bp$ . The linear dependence ( $R^2 = 0.998$ ) extracted from this plot has a slope corresponding to a rise

of 0.28 nm per bp step, which is in excellent agreement with the crystallographic value for A-RNA.<sup>196</sup>

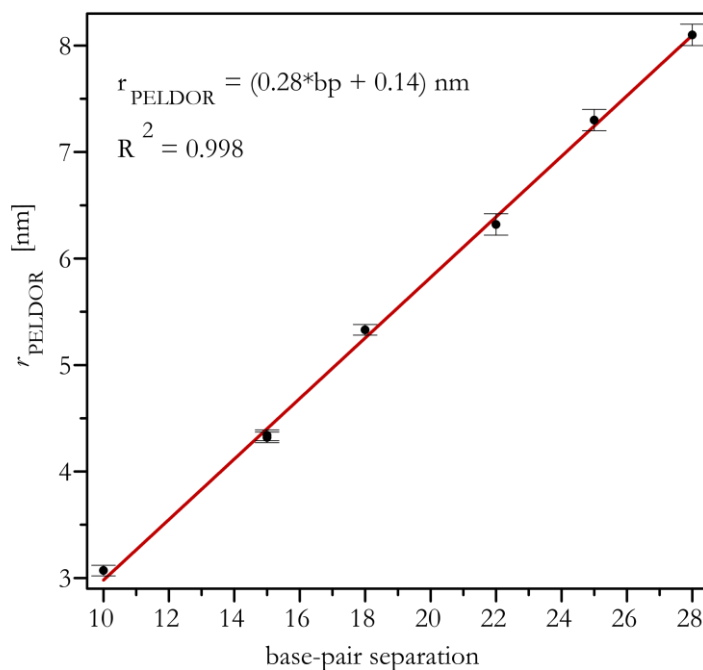


**Figure 6-15: Experimental Distances vs. Base-Pair Separation**

*Plot of experimental distances vs. base-pair separation between labelled cytosines in the RNA duplexes 1-8. Error bars indicate uncertainty in the peak distance (see § 6.2.3). A linear fit (correlation coefficient  $R^2 = 0.998$ ) reveals a rise of 0.28 nm for the experimental distance per base-pair step. The small value of 0.14 nm is found for an intercept, but it is unknown whether this value is significant as it is close to the estimated distance uncertainty.*

Time traces recorded on samples **6-8** displayed frequency contributions of short distances. The magnitude of this contribution was concentration dependent pointing to aggregates. Figure 6-16 (top) shows PELDOR/DEER experiments performed on samples of higher duplex concentration (100  $\mu\text{M}$ ), where the effect is visible as oscillations at short time points (marked by an arrow). Analysis of the trace recorded on sample **6** reveals a corresponding distance of approximately 3.5 nm for the high frequency component. According to the spectroscopic ruler

obtained in Figure 6-15 this distance is consistent with a base-pair separation of 12. For sample **6** this is in perfect agreement with an end-to-end stacking of the helices as shown in Figure 6-16 (bottom). This explains why the artefact is preferably observed when the labels are inserted at nucleotides close to the end of the sequence, as the intermolecular distance becomes shorter and better visible in this case.

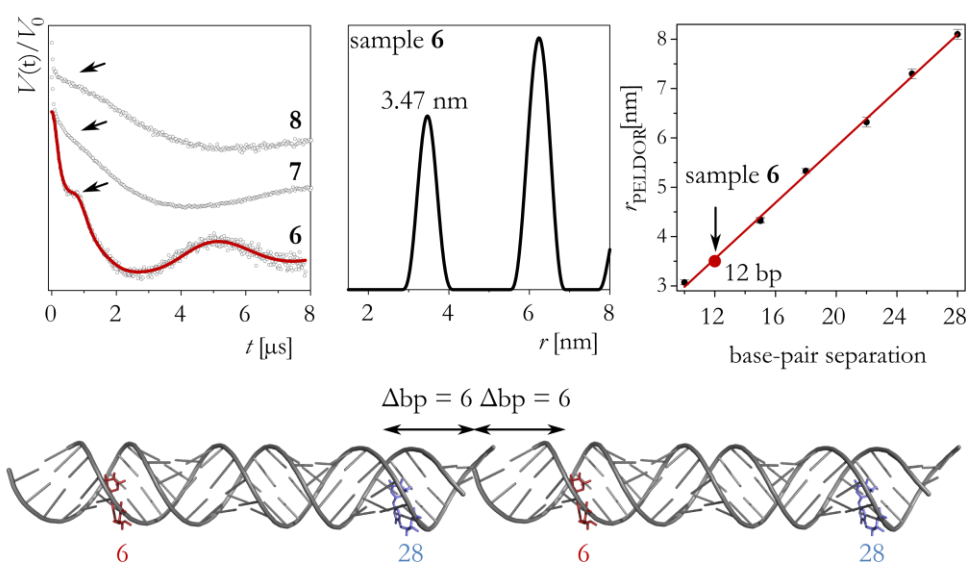


**Figure 6-16: PELDOR Traces of Samples 6 - 8 at Duplex Concentrations of 100  $\mu$ M.**

*Top: Traces recorded on samples with high duplex concentration display an additional high frequency component, which is specifically strong in sample **6**. Analysis of PELDOR/DEER trace of sample **6** results in a second distance at around 3.5 nm. Extraction of the  $\Delta bp$  from the linear relation derived in Figure 6-15 leads to a base-pair separation of about 12. Bottom: This base-pair separation is consistent with an end-to-end aggregate, in which the two duplexes add to form a longer one, as shown in the picture.*

### 6.2.3 Error Estimation - Effect of Trace Length and Background Subtraction

Uncertainties in the background correction are one contributor to errors in the determination of the main distance and its distribution. To

estimate the influence of the background model and the way it is fitted to the experimental traces on the analysis of the PELDOR/DEER experiments on the  $C^T$  labelled RNA, several background corrections have been performed; e. g. the use of a mono-exponential decay vs. a second order polynomial as model, and fitting to the last 50 % vs. to more than 50 % of the experimental time trace. The four background corrections are shown in Figure 6-17, A to Figure 6-20, A, with the Fourier transformations of the corrected traces as inset. A reasonable background subtraction should result (after Fourier transformation of the corrected time trace) in a Pake pattern showing little distortions around zero frequency.  $\alpha$ -values were chosen by the L-curve criterion as described in § 2.2.3, ensuring maximum smoothness with minimum r.m.s.d. between experimental and simulated time trace. To illustrate the effect of the  $\alpha$ -values Figure 6-17, B to Figure 6-20, B display the resulting fits and distributions corresponding to values around the corner of the L-curve. The analysis was performed for four representative traces:

- 1) *Experimental time trace for which the oscillation has decayed to zero*  
(sample **1**, Figure 6-17);
- 2) *Experimental time trace with 2.5 oscillation periods*  
(sample **3**, Figure 6-18);
- 3) *Experimental time trace with only 1.5 oscillation periods and large S/N*  
(sample **6**, Figure 6-19)
- 4) *Experimental time trace with only 1.5 oscillation periods and weaker S/N*  
(sample **7**, Figure 6-20)

Analysis of time traces corresponding to case 1 and 2 (sample 1 and 3) show little variation of the peak distance ( $\leq 0.02$  nm, standard deviation  $\sigma = \pm 0.01$ ) as a function of the background subtraction (Figure 6-17 and Figure 6-18, C). This is less than the statistical error when repeating the experiment.

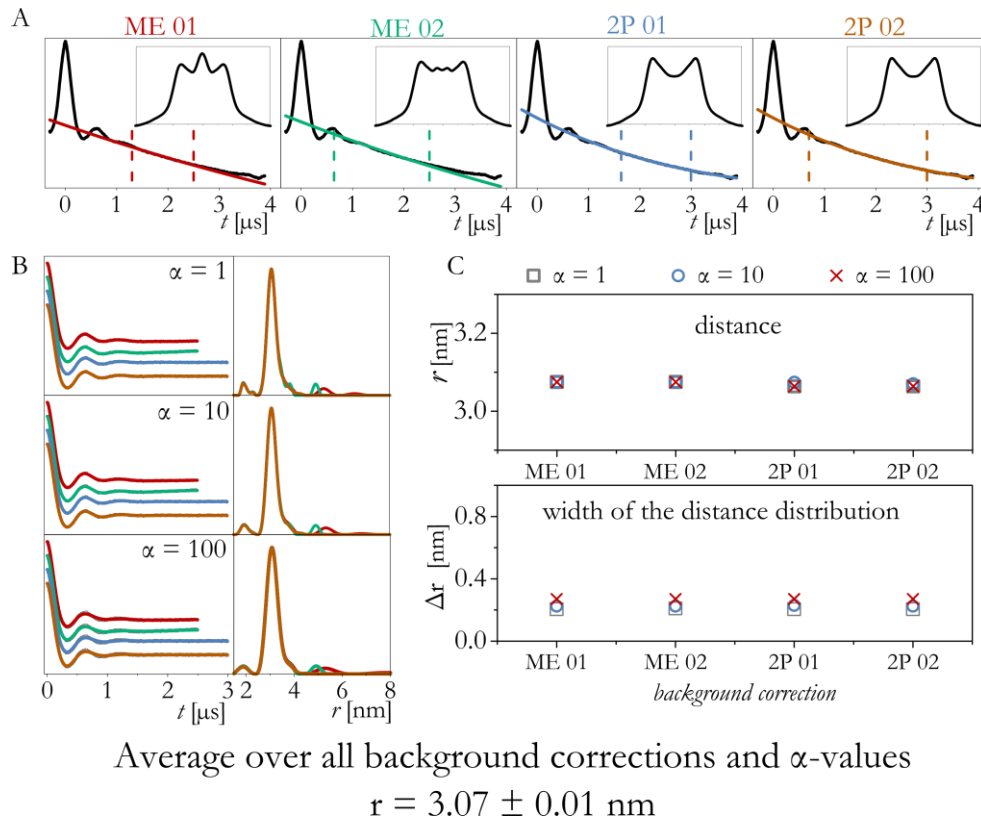
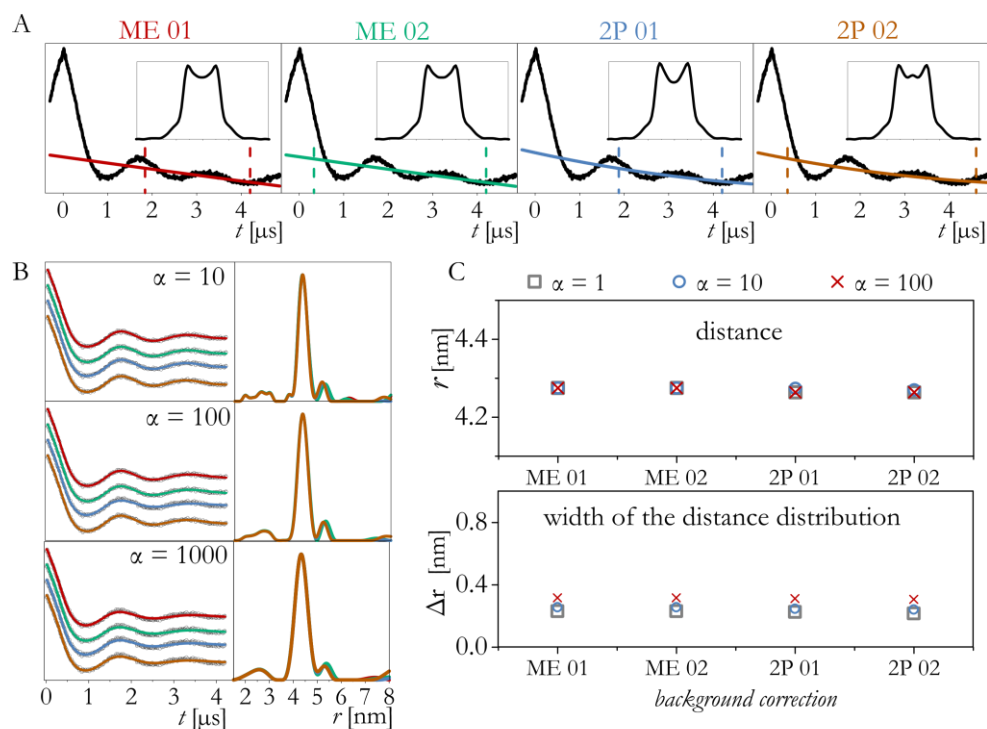


**Figure 6-17: Effect of Background Subtraction on the Analysis of Traces Recorded on Sample 1.**

TOP: Row experimental time traces and background for subtraction fitted with 4 different approaches. A mono-exponential decay was fitted to the last 50 % of the row data (ME 01) or to more than 50 % (ME 02). The same comparison is performed for a second order polynomial background (2P 01 and 2P 02). Insets show Fourier transformations of the background corrected traces. Bottom left: Background corrected time traces according to colour code, DEERanalysis fits and resulting distance distributions for three different  $\alpha$ -values. Bottom right: Table and plots illustrating the dependence of the peak distance and its distribution on the chosen background correction.

Traces corresponding to case 1 or 2 (samples 1-5) displayed in Figure 6-13 were corrected using a second order polynomial fitted to approximately 50 % of the time trace, labelled 2P 01 in Figure 6-17 to Figure 6-20.



Average over all background corrections and  $\alpha$ -values

$$r = 4.32 \pm 0.005 \text{ nm}$$

**Figure 6-18: Effect of Background Subtraction on the Analysis of Traces Recorded on Sample 3.**

TOP: Row experimental time traces and background for subtraction fitted with 4 different approaches. A mono-exponential decay was fitted to the last 50 % of the row data (ME 01) or to more than 50 % (ME 02). The same comparison is performed for a second order polynomial background (2P 01 and 2P 02). Insets show Fourier transformations of the background corrected traces. Bottom left: Background corrected time traces according to colour code, DEERanalysis fits and resulting distance distributions for three different  $\alpha$ -values. Bottom right: Table and plots illustrating the dependence of the peak distance and its distribution on the chosen background correction.

If the analysis is performed on traces corresponding to case 3 and 4 (only 1.5 full modulation periods are recorded) the peak distance varies up to 0.12 nm ( $\sigma = \pm 0.06$ ) with the chosen background subtraction.

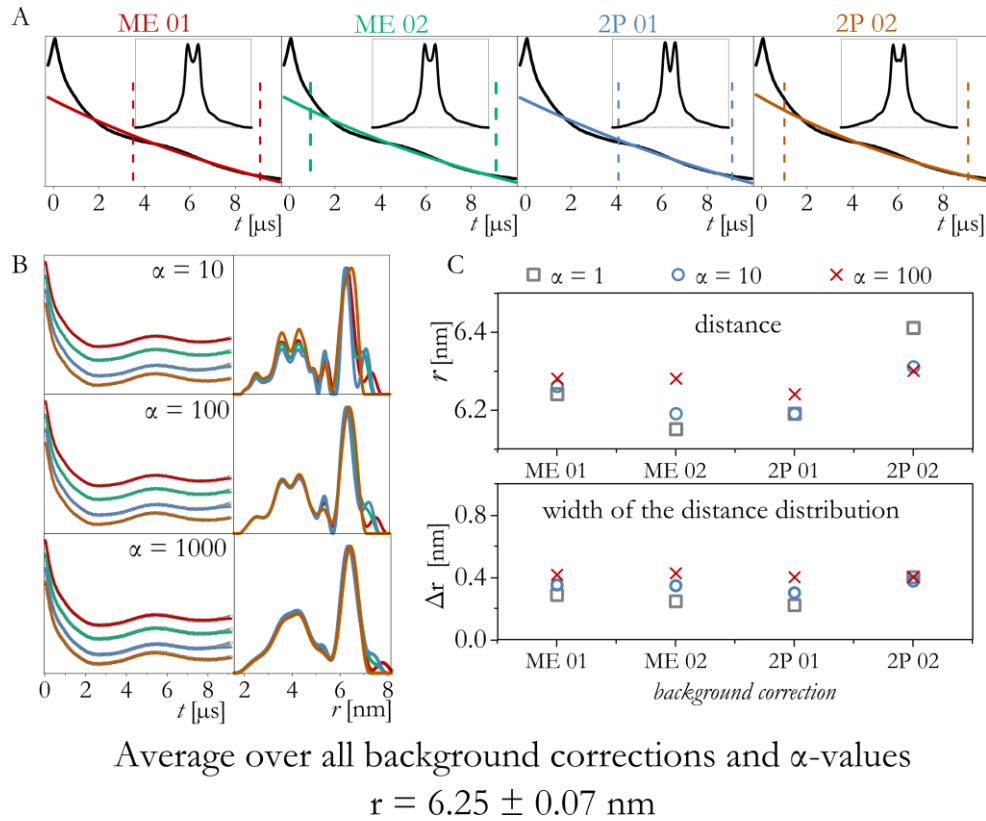


**Figure 6-19: Effect of Background Subtraction on the Analysis of Traces Recorded on Sample 6.**

TOP: Row experimental time traces and background for subtraction fitted with 4 different approaches. A mono-exponential decay was fitted to the last 50 % of the row data (ME 01) or to more than 50 % (ME 02). The same comparison is performed for a second order polynomial background (2P 01 and 2P 02). Insets show Fourier transformations of the background corrected traces. Bottom left: Background corrected time traces according to colour code, DEERanalysis fits and resulting distance distributions for three different  $\alpha$ -values. Bottom right: Table and plots illustrating the dependence of the peak distance and its distribution on the chosen background correction.



In this case the background model labelled 2P 02 (second order polynomial fitted to more than 50 % of the experimental time trace) resulted in a Pake pattern with least distortions and was therefore chosen for analysis of experiments on samples 6-8 as given in Figure 6-13.

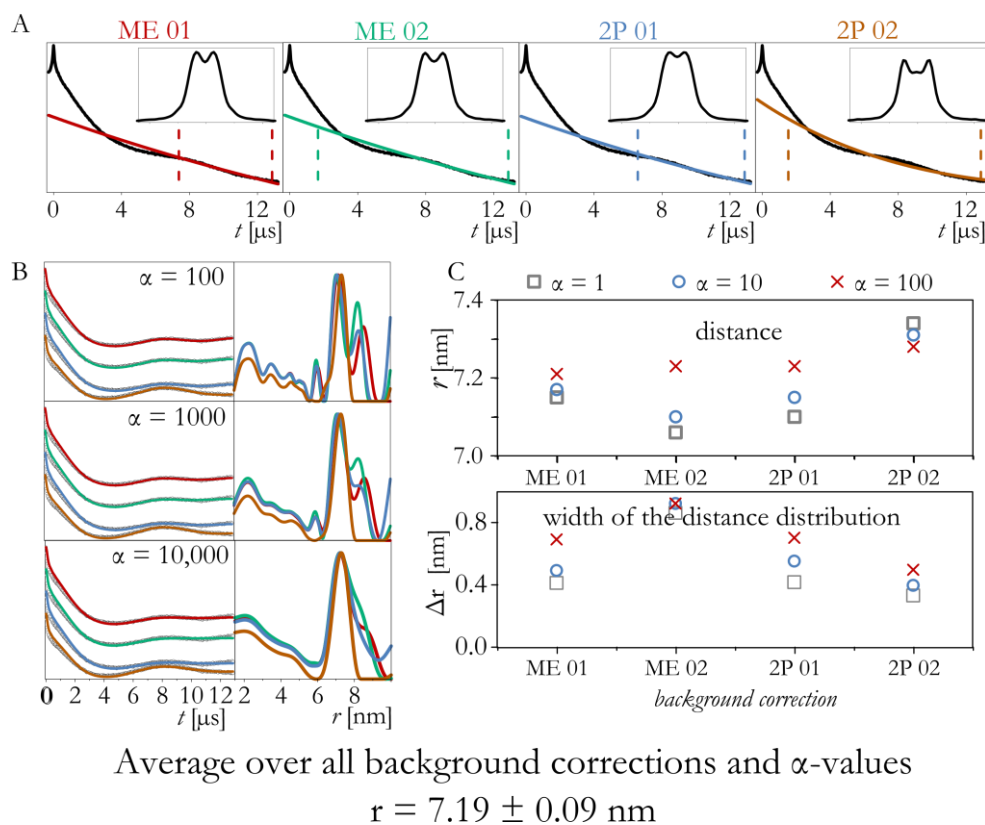


**Figure 6-20: Effect of Background Subtraction on the Analysis of Traces Recorded on Sample 7.**

TOP: Row experimental time traces and background for subtraction fitted with 4 different approaches. A mono-exponential decay was fitted to the last 50 % of the row data (ME 01) or to more than 50 % (ME 02). The same comparison is performed for a second order polynomial background (2P 01 and 2P 02). Insets show Fourier transformations of the background corrected traces. Bottom left: Background corrected time traces according to colour code, DEERanalysis fits and resulting distance distributions for three different  $\alpha$ -values. Bottom right: Table and plots illustrating the dependence of the peak distance and its distribution on the chosen background correction.

To determine the distance distribution the largest  $\Delta r$  was chosen as upper limit in case 3 (sample **6**, Figure 6-19). Inspection of Figure 6-20, C reveals that the width of the distribution for case 4 (sample **7**) strongly depends on the background correction, which is mainly caused by the artefacts marked by the asterisk in the distribution. As only the second order polynomial 2P 02 resulted in a reasonable Pake pattern,  $\Delta r$  was extracted from this analysis.

In summary, the uncertainty of the peak distance was mainly owed to the statistical error arising from three different sets of experiments if 2.5 oscillations are recorded to be approximately  $\pm 0.05$  nm (sample **1-5**). The estimated error increases up to  $\pm 0.1$  nm if only 1.5 oscillations are recorded (sample **6-8**). The uncertainty from the background correction in the peak distance is found less than the statistical error arising from the sample triplicates.

**Table v**

*Main distance  $r \pm$  estimated error and distance distributions  $\Delta r$  obtained by the analysis shown above.*

<b>Case</b>		<b>Sample</b>	<b>r [nm]</b>	<b><math>\Delta r</math> [nm]</b>
1	2.5 oscillations	<b>1</b>	$3.07 \pm 0.05$	0.23
2	2.5 oscillations	<b>3</b>	$4.32 \pm 0.05$	0.25
3	1.5 oscillations	<b>6</b>	$6.24 \pm 0.10$	0.38
4	1.5 oscillations	<b>7</b>	$7.3 \pm 0.10$	0.51

### 6.3 Discussion of PELDOR Experiments on C<sup>T</sup>-labelled RNA

The fact that PELDOR/DEER traces recorded at Q-band frequency with selective pulses exhibit weak orientation selection effects as reported in (§ 6.2.1) is symptomatic for the C<sup>T</sup> labels restricted conformational freedom in the RNA duplex structure. The restriction is owed to the zero-length linker to the nucleobase and the tight accommodation in the major groove. The use of broadband excitation can eliminate orientation selection in the experiments allowing extracting reliable distance distributions. The restriction of the label proves to be a significant advantage in this case, as it entails narrow distance distributions, which is preferable particular for the measurement of longer distances, as demonstrated in § 6.2.2. Another favourable property of the C<sup>T</sup> label is its position in the major groove with the NO group being located very close to the symmetry axis of the RNA duplex

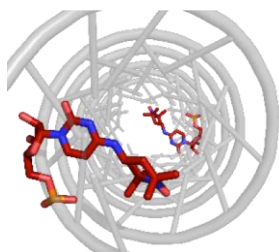


**Figure 6-21: Model of C<sup>T</sup>-Labelled RNA, Top View**

*Pymol model of A-form RNA labelled at position 3 and 31 illustrating the positioning of the NO group close to symmetry axis of the duplex.*

as shown in Figure 6-21. As a result the striking correlation between experimental inter spin distances and the length increment per base pair step could be observed (Figure 6-15), and the obtained relationship can be used as a ruler to directly convert experimental distances measured in RNA duplex structures into base-pair separation, dispensing the requirement of molecular modelling. Narrow distributions observed in the PELDOR/DEER experiments on the RNA samples are in agreement with previous results. Piton *et al.* performed distance

measurements on RNA duplexes using the rigid TPA label and observed distances up to 4 nm with distributions also varying between about  $\Delta r = \pm 0.1$  and  $\pm 0.4$  nm, however dependent on the label environment.<sup>114</sup> In contrast the results presented in § 6.2.2 indicate that the differences in stacking interactions caused by upstream or downstream nucleotides do not have a significant influence on the conformational preference of the nitroxide to sit in the major groove of the duplex, in the case of C<sup>T</sup>. The advantage of model-free interpretation of experimental distances when using the C<sup>T</sup> label is particularly apparent when comparing to distance measurements performed on RNA labelled with flexible nitroxides. PELDOR/DEER studies using the popular nucleic acid label R5 are reported to result in more complex distance.<sup>99</sup> The obtained dipolar frequencies could only be interpreted after identification of accessible conformations of R5, by molecular modelling taking into account possible clashes with the RNA backbone.<sup>102</sup> The spin label attached to 4-thiouridine, where the linker consists of five rotatable bonds and Watson-Crick base-pairing is not preserved, will result in a similar afford.<sup>107, 160</sup> Though the increase of distance distributions with increasing base pair separation between the labels is reflective of the dynamics of the duplex, the overall quite narrow distributions determined for distances up to 8 nm as reported in Table iv are not necessarily expected for experiments on nucleic acid duplexes. Previous PELDOR/DEER experiments on B-DNA carrying rigid labels positioned of the helix axis showed distributions of  $\Delta r = \pm 0.4$  nm for distances of 4 nm already. According to SAXS data even more pronounced distributions for increasing end-to-end distances can be caused by cooperative DNA stretching.<sup>197</sup> To understand the narrow distributions obtained for C<sup>T</sup> labelled RNA, Deniz Sezer

conducted MD simulations for the RNA sequence.<sup>194</sup> The simulations were carried out for two RNA duplexes, one carrying C<sup>T</sup> at position 6, 16 and 28 (Figure 6-22, A), the second one at positions 6, 16 and 31 (Figure 6-22, B). Starting structure was constructed from an ideal A-form RNA duplex with the C<sup>T</sup> label attached in conformation **2** (Table iii). Figure 6-22 shows histograms of the inter-spin distances extracted from the simulations.

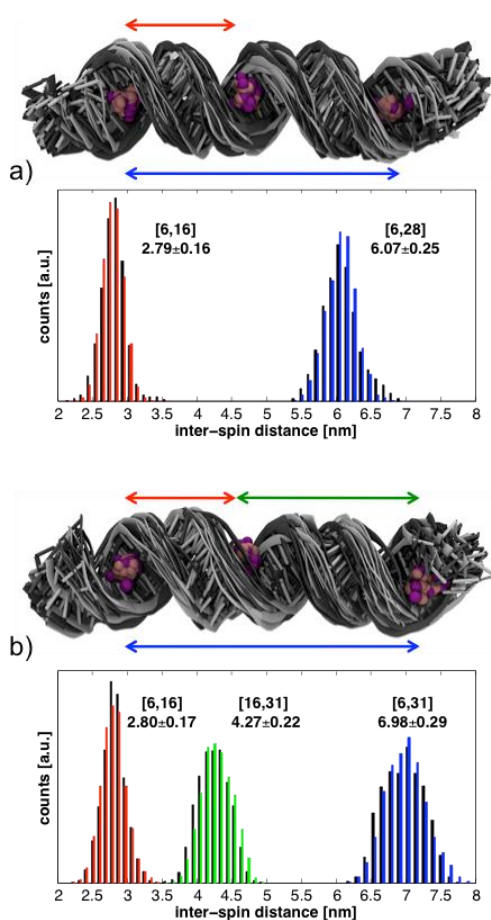


**Figure 6-22: MD Simulations**

Figure and caption are taken from reference<sup>194</sup> Structural ensembles and histograms of the inter-spin distances from the MD simulations of RNA helices labelled at positions (a) 6-16-28 and (b) 6-16-31. Structures and histograms from the first 17 ns are shown in black; those from the last 17 ns are in grey or in colour. The N and O atoms of the TEMPO moiety are shown with purple (first 17 ns) and pink (last 17 ns) balls. The reported average distances and their standard deviations (in nm) are calculated from the entire 34 ns simulations.

The width of the distance distributions extracted from the MD simulation show very good agreement with the ones obtained in the PELDOR/DEER experiment. The first question that was answered by

the MD simulations is the dynamic of the CT label itself. Although the two rotatable bonds in general enable the occupation of a relatively large conformation space, half of this space is eliminated for sterical reasons, due to Watson-Crick base-pairing (Figure 6-3). During the MD-simulation, when the label is inserted in the RNA duplex, it is observed to only populate conformation **1** and **2**, which lead to very similar position of the NO moiety. Restricted simulations, in which the RNA duplex itself was fixed, allowed estimating that the internal conformational freedom of the spin label to account for at most 0.15 nm of the width of the inter-spin distance distribution. In conclusion the small conformational contribution of the label to the observed distance distributions allows resolving subtle conformational dynamics of the RNA and the widths observed in the experiment should report on global RNA distortions. The overall narrow widths ( $\Delta r < 0.5$  nm) obtained in the distance measurements and the structural ensembles observed in the MD simulations suggest very small average deviations of the duplex from the ideal A-form structure. The results are supported by  $\mu$ s-long MD simulations reporting moderately small fluctuations of a RNA helix around the A-form.<sup>198</sup> The fluctuations are certainly smaller the ones reported for B-DNA. As MD simulations are performed at 300 K it can be concluded that the narrow distance distributions observed in PELDOR/DEER experiment are not an artefact of the frozen solution but reflect an intrinsic property of RNA helices.

## 7. Chapter

### PELDOR on TOPP-labelled Transmembrane Peptides

#### – Distance Measurements in Lipid Bilayers

This chapter will present the research performed on TOPP-labelled WALP24. The results presented here were published in *biophysical journal*.<sup>199</sup> Some figures are adapted from this manuscript.

### 7.1 Materials and Methods

Figure 7-1 displays the sequence of WALP24 as employed in this study. X denotes the positions at which the spin labels TOPP or MTSSL have been inserted. Samples were received dissolved in methanol, from Janine Wegner from the research group of Professor Diederichsen. (Georg August University, Göttingen)

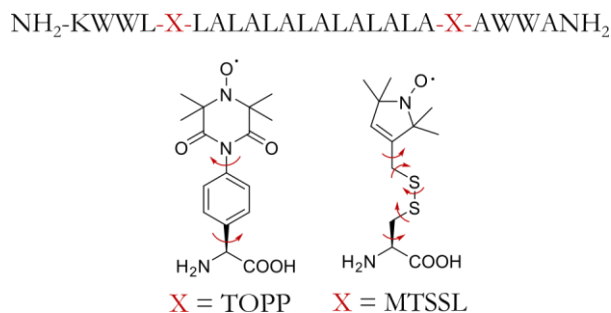


**Figure 7-1: Spin Labelled WALP24.**

*Top: Peptide sequence of WALP24 showing the positions (X), at which the spin labels have been inserted. Bottom: Chemical structure of the two spin labels MTSSL and TOPP. Red Arrows indicate rotatable bonds.*

### 7.1.1 Preparation of EPR samples

#### *Determination of Labelling Efficiency*

Labelling efficiency of WALP24-MTSSL samples was determined via room temperature cw EPR spectroscopy at X-band frequencies, in a Bruker Elexsys E500 spectrometer equipped with the Bruker super-high Q resonator ER4122SHQE. A sample volume of 20  $\mu\text{L}$  was filled into glass capillaries of 1 mm inner diameter (2 mm outer diameter). Spin concentrations were calculated with a calibration curve recorded with 4-hydroxy-TEMPO at concentrations between 5 and 100  $\mu\text{M}$ , from the double integral of the cw-EPR spectra. Comparison of the calculated spin concentration with the nominal WALP24-MTSSL concentration, determined by UV absorbance of the tryptophans, revealed labelling efficiencies around 80-90 % for different batches. The determination of WALP24-TOPP's peptide concentration is compromised as TOPP's absorption spectrum in the peptide is potentially overlapping with the tryptophans' absorption. Therefore the labelling efficiency was estimated by comparing the modulation depths achieved in PELDOR/DEER experiments on WALP24-MTSSL and WALP24-TOPP in methanol that were performed under the same experimental conditions. DEERanalysis does offer a tool for calibration of experimental modulation depths to a known labelling efficiency using the relation between the average number of spins per molecule  $\langle n \rangle$  ( $n = 2 = 100\%$  labelling efficiency), the modulation depth parameter  $\lambda$  and the total modulation depth  $\Delta$ :  $\Delta = 1 - [\lambda(\langle n \rangle - 1)]$ .<sup>64</sup> Table vi displays the estimated labelling efficiency assuming 80-100 % labelling efficiency for WALP24-MTSSL.



**Table vi**  
*Estimation of WALP24-TOPP's labelling efficiency.*

<b>Labelling efficiency WALP24-MTSSL</b>	<b>Labelling efficiency WALP24-TOPP</b>
Determination via cw-EPR ( $\Delta = 28 \%$ )	Estimation from $\Delta$ ( $\Delta = 16.5 \%$ )
100 % (2 spins)	77.5 % (1.55 spins)
80 % (1.6 spins)	66.5 % (1.33 spins)

The comparison of the modulation depths  $\Delta$  observed in the PELDOR/DEER experiments on WALP24 in MeOH, indicates a labelling efficiency of 65-75 % for WALP24-TOPP. It is important to note, that this is estimation, as no modulation depth calibration for samples of varying labelling efficiency was performed.

#### *EPR Sample Preparation*

For distance measurements in solution WALP-TOPP and WALP-MTSSL were dissolved in methanol containing 20% glycerol yielding a spin concentration of 40  $\mu\text{M}$ . EPR samples of WALP24-TOPP and WALP24-MTSSL in multilamellar vesicles (MLV) of deuterated phospholipids were prepared by combining stock solutions of the deuterated phospholipid (*Avanti*) in chloroform and the peptide in methanol, yielding a spin concentration of 40  $\mu\text{M}$  in the final sample volume and a spin-to-phospholipid molar ratio of 1-to-3000. Solvents were removed under nitrogen gas stream followed by 3-4 h vacuum drying. Next the peptide-lipid film was suspended in tris-HCl buffer (20 mM, pH = 7.4) and the resulting suspension was blended on a vortex mixer for 2 minutes above the lipids transition temperature. Three

freeze-thaw cycles with vortex mixing steps between each cycle were employed to increase the homogeneity of the vesicles. Samples were incubated for 30 min above the lipids main transition temperature. 50  $\mu\text{L}$  were mounted into an EPR tube (3 mm outer diameter, 2 mm inner diameter) and rapidly frozen in liquid nitrogen. Samples of varying peptide-to-lipid ratio of WALP24-MTSSL in DMPC MLVs were prepared by combining stock solutions of the peptide in methanol and the phospholipid (*Avanti*) in dichloromethane, yielding a peptide concentration of 30  $\mu\text{M}$  in the final sample volume and the desired peptide-to-phospholipid molar ratio. Following the protocol described above tris-HCl buffer (20 mM, pH = 7.4) was added to the peptide lipid film and the resulting suspension was mixed on a vortex mixer for 2 minutes above DMPC's transition temperature. After incubation 15  $\mu\text{L}$  were transferred into an EPR tube (1 mm inner diameter) and rapidly frozen in liquid nitrogen. 15  $\mu\text{L}$  WALP-MTSSL in methanol containing 20 % glycerol in an EPR tube (1 mm inner diameter) were prepared for comparison.

### 7.1.2 PELDOR/DEER Experiments

Employing EPR tubes of 3 mm outer diameter required the use of the Bruker ER5107QT-II resonator. The frequency at the dip centre was chosen for pumping at the maximum of the nitroxide's EPR spectrum giving a  $\pi$ -pulse length of 16-18 ns. Detection frequency was set 90 MHz lower with a  $\pi$ -pulse length of 26-28 ns. The time delay  $\tau$  between the first two pulses in the sequence was set to 400 ns and the dipolar evolution time  $T$  (spacing between second and third detection pulses) was set to 1.9  $\mu\text{s}$ . As the last 100 ns – 400 ns of the traces usually

contained artefacts they were not considered in data analysis. Acquisition times were typically on the order 10 to 15 h. As PELDOR/DEER experiments on samples of varying WALP24-MTSSL-to-DMPC ratios were conducted with smaller sample volumes (EPR tubes of 1.5 mm outer diameter), the EN5107D2 Bruker resonator was employed for these experiments. In this case the typical  $\pi$  pulse length was 12 ns at the dip centre and 24 ns when the frequency is shifted by 90 MHz. The pumping frequency was set in the resonator dip centre and at the maximum of the nitroxide's EPR spectrum, while detection frequency was chosen 90 MHz lower. The time delay  $\tau$  between the first two pulses in the sequence was set to 300 ns and the dipolar evolution time  $T$  (spacing between second and third detection pulses) was set to 1.4  $\mu$ s. For the sample having a ratio of 1-to-250  $T$  had to be shortened to 0.6  $\mu$ s due to a strongly shortened  $T_m$ . The last 200 ns of the traces usually contained artefacts and were not considered in data analysis. Acquisition times were on the order 20 h. Data analysis was performed after dipolar traces were background corrected using either a mono-exponential or a second-order polynomial function. Distance distributions were obtained with the program DEERanalysis, using a fitting procedure based on Tikhonov regularization and the L-curve criterion.

### **7.1.3 Construction of Molecular Model of TOPP and MTSSL-labelled WALP24**

Energy minimization of the peptide structure was performed using the PEP-FOLD webserver.<sup>195</sup> For the WALP-MTSSL case the peptide sequence for minimization contained a cysteine at the respective label

positions at which rotamers of MTSSL calculated using MMM were attached subsequently.<sup>119</sup> For modelling WALP24-TOPP, an optimized WALP24 peptide structure containing a tyrosine at the label positions was computed, to account for possible aromatic  $\pi$ -interaction by the TOPP label. In the geometry optimized structure the tyrosine was subsequently replaced by TOPP, with the TOPP structure as minimized earlier.<sup>142</sup>

#### 7.1.4 Experiments and Simulation of Orientation Selective PELDOR on WALP24-TOPP

PELDOR experiments were performed employing small sample volumes (EPR tubes of 1.5 mm outer diameter) and the EN5107D2 Bruker resonator. The spectral positions for pumping were chosen either at the maximum of TOPP's EPR spectrum or 10 G lower in field giving the two series of experiments 1 and 2 (§ 7.2.1). Frequency separation was varied between 90 and 130 MHz for both series. Simulations were conducted using a home written program that takes into account orientation selection in PELDOR/DEER experiments.<sup>59, 62</sup> Simulations considered experimental parameters (pulse lengths, frequency separation, EPR detection frequency, nitroxide EPR parameters).  $\mathbf{A}$ - and  $\mathbf{g}$ -tensor, which are required for simulating orientation selection were derived in an earlier study.<sup>62</sup> Euler angles were calculated from relative orientation of the two TOPP labels as extracted from the minimized WALP24-TOPP structure. Dipolar frequency for the simulation was obtained from the PELDOR/DEER experiments in methanol (§ 7.1.3). The rotational freedom of the TOPP label around its two single bonds,  $\Phi_1$  and  $\Phi_2$  (defined in Figure 7-2), was taken into account by rotating around the x-

axis of the  $\mathbf{g}$ - and  $\mathbf{A}$ -tensor which is parallel to the respective single bonds (Figure 7-2). Simulations were conducted with and without rotation ( $\pm 25^\circ$  vs.  $\pm 0^\circ$ ) for  $\Phi_1 + \Phi_2$  to average orientation selection (as observed in an earlier study<sup>62</sup>).

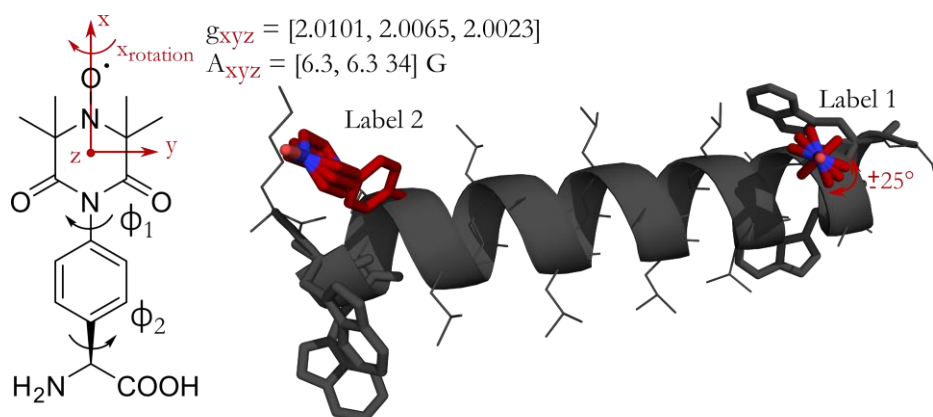


**Figure 7-2: Model of WALP24-TOPP for Simulation.**

*Left: Chemical structure of the TOPP label and orientation of the magnetic  $\mathbf{g}$ - and  $\mathbf{A}$ -tensor (red), which are collinear in the nitroxide radical and principal axis values of  $\mathbf{g}$ - and  $\mathbf{A}$ -tensor as published in <sup>62</sup>. Molecular Model of WALP24-TOPP with the TOPP label at position 5 (label 2) and position 20 (label 1) rotated  $\pm 25^\circ$  around one of the single bonds illustrating the rotation around the  $\mathbf{g}$ -tensors x-axis. Methyl-groups and oxygen of the TOPP label are hidden for simplicity.*

## 7.2 Results on TOPP and MTSSL-labelled WALP24

This section will display the results of PELDOR experiments on WALP24 in methanol solution and lipid environment.

### 7.2.1 Examination of Orientation Selection

To examine whether Q-band distance measurements performed on the quasi-rigid TOPP label are affected by orientation selection,

PELDOR/DEER experiments with changing resonance positions were performed. All experiments were performed under broadband excitation conditions. Figure 7-3 displays PELDOR/DEER traces recorded with pumping at the maximum of TOPP's EPR spectrum and detecting at 70-130 MHz lower frequency (higher field values).

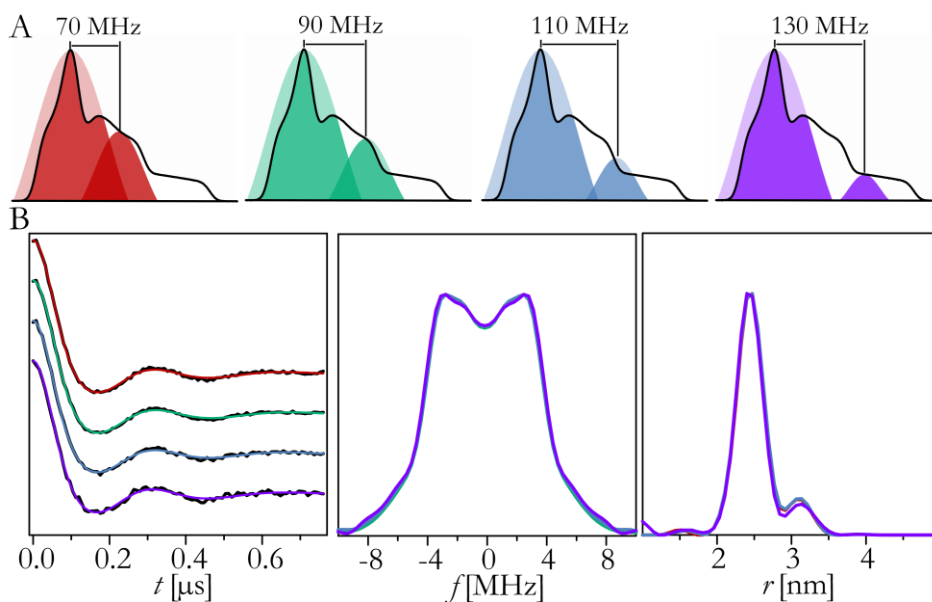


**Figure 7-3: Orientation Selection Experiment WALP24-TOPP Series 1**

*A: Experimental setup series 1: experimental ESE (black line), and pulses according to the experimental setup (coloured) with the pump pulse applied at the maximum of the EPR spectrum. Frequency separation between pump and detection was varied from 70 MHz to 130 MHz. Pulse lengths were 12 and 18-28 ns for pumping and detection, respectively. B: DEER analysis fits (left, coloured lines) of the experimental time traces (left, black lines), their Fourier transformations (middle) and corresponding distance distributions (right). Experimental time traces and distance distributions show no dependence on the experimental setup.*

A set of experiments with the resonance position of the frequency for pumping set to a field value 10 G below the maximum of the EPR line and detection set 70-130 MHz lower is shown in Figure 7-4. The traces

and their Fourier transformations do not reflect a dependence of the dipolar frequency on the experimental setup, demonstrating the absence of orientation selection with high-power hard pulses.

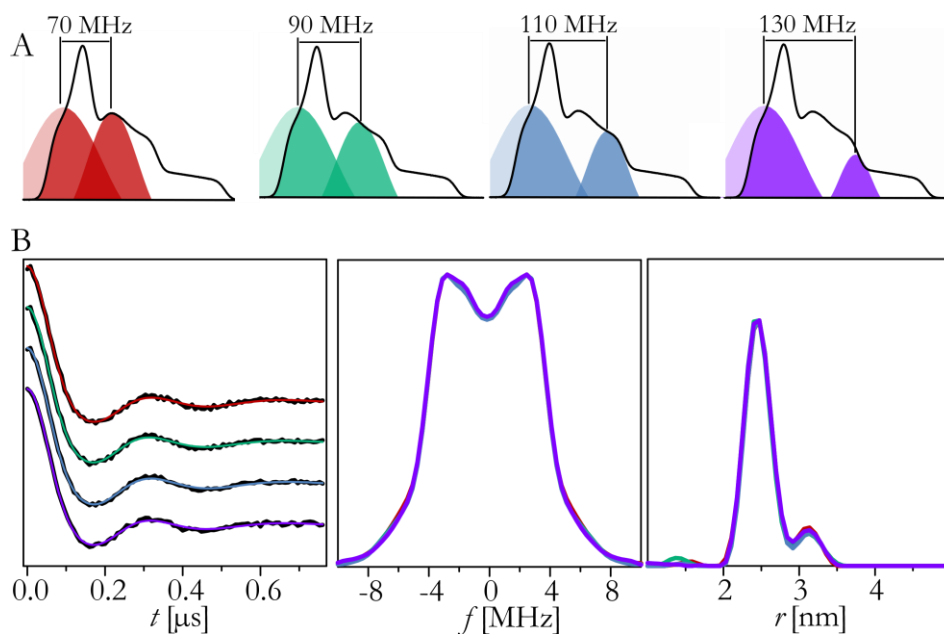


**Figure 7-4: Orientation Selection Experiment WALP24-TOPP Series 2**

*A: Experimental setup series 2: experimental ESE (black line), and pulses according to the experimental setup (coloured) with the pump pulse applied 10 G below the maximum of the EPR spectrum. Frequency separation between pump and detection was varied from 70 to 130 MHz. Pulse lengths were 12 and 18-28 ns for pumping and detection, respectively. B: DEER analysis fits (left, coloured lines) of the experimental time traces (left, black lines), their Fourier transformations (middle) and corresponding distance distributions (right). Experimental time traces and distance distributions show no dependence on the experimental setup.*

The experimental findings are supported by simulation of orientation selective PELDOR/DEER traces for the experimental conditions as described in § 7.1.4. To account for a possible rotation of the label around its two single bonds simulation was performed with a libration of

the  $\mathbf{g}$ - and  $\mathbf{A}$ -tensor around its x-axis, which is parallel to the NO-axis of the molecule. Results of the simulations conducted for series 1 (pumping at the maximum of the EPR spectrum) are summarized in Figure 7-5.

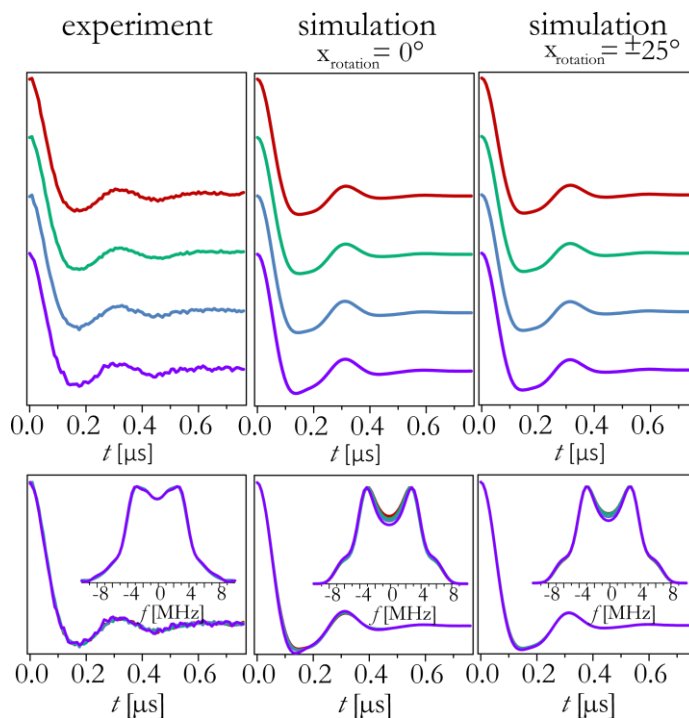


**Figure 7-5: Orientation Selective PELDOR Series 1 Simulation vs. Experiment**

*Orientation selective experiments and simulations for pumping at the maximum of TOPP's EPR spectrum and frequency separation of 70 to 130 MHz as displayed in Figure 7-3, A Top: experimental (left) and simulated time traces (for rotation around the x-axis of  $0^\circ$  (middle) and  $\pm 25^\circ$  (right)) for the four setups of series 1. Bottom: Time traces and corresponding Fourier transformations (inset).*

When comparing the time traces corresponding to the four setups (illustrated Figure 7-3, A) simulated without rotation around the two bonds, only the setup with 130 MHz frequency separation (Figure 7-5 middle, violet line) displays a noticeable deviation in the distribution of the dipolar frequency. However, this effect vanishes upon averaging over a rotation of  $\pm 25^\circ$  around the NO-axis. Figure 7-6 shows the



simulations performed with the experimental conditions of series 2 (Figure 7-4, A) compared to the experiment. In this case, the simulated time traces do not display a distinguishable difference between the two cases of averaging over  $\pm 25^\circ$  vs.  $0^\circ$ .

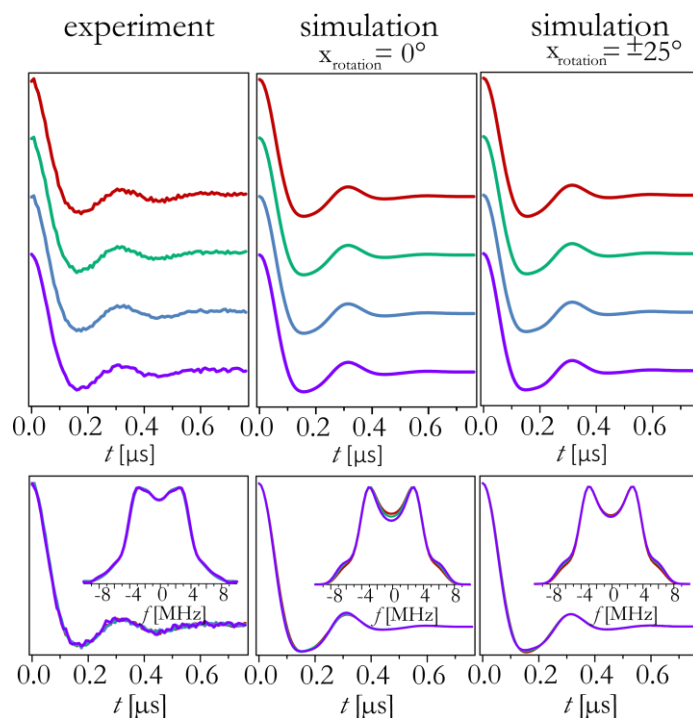


**Figure 7-6: Orientation Selection Simulation WALP24-TOPP Series 2**

*Orientation selective experiments and simulations for pumping 10 G below the maximum of TOPP's EPR spectrum and frequency separation of 70 to 130 MHz, as displayed in Figure 7-4, A. Top: experimental (left) and simulated time traces (for rotation around the x-axis of  $0^\circ$  (middle) and  $\pm 25^\circ$  (right)) for the four setups of series 1. Bottom: Time traces and corresponding Fourier transformations (inset).*

This subtle difference between the two setups of pumping at the maximum of the EPR spectrum vs. pumping at 10 G lower field observed in the simulation are not resolved in the experiment as shown in Figure 7-7. While the trace obtained from orientation selective simulation with pumping 10 G below the maximum of the EPR

spectrum (grey line) perfectly represents the trace simulated with full excitation of the EPR spectrum (red dashed line), the trace corresponding to pumping at the maximum of the spectrum (black line) displays slight deviation from the full excitation case.

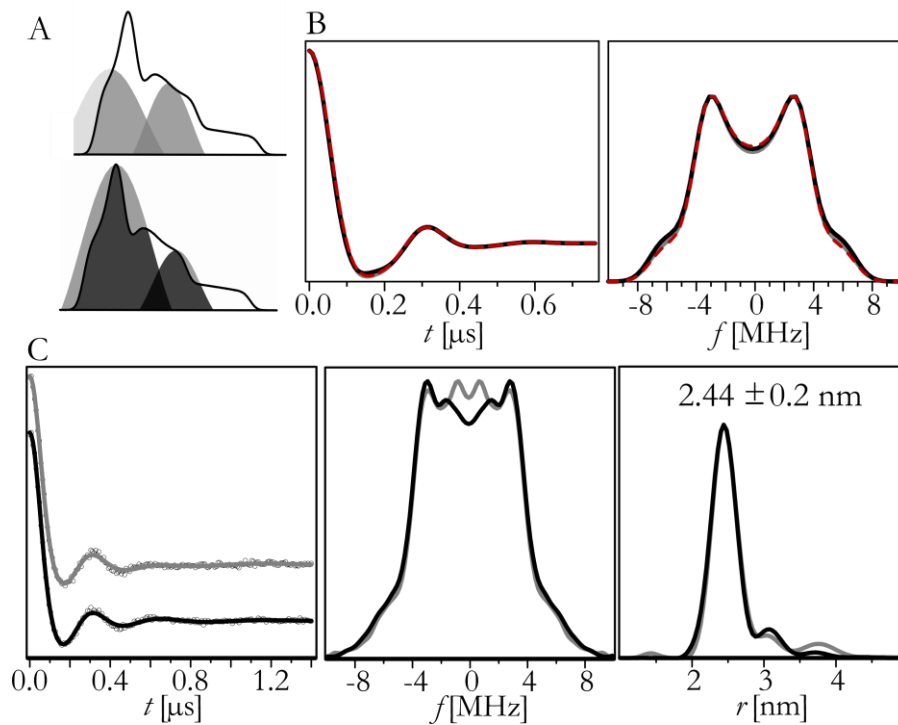


**Figure 7-7: Comparison of Experiments from Series 1 and Series 2**

*A: Experimental echo-detected field-sweep (black line) of WALP24-TOPP, and pulses according to the experimental setup. Frequency separation between pump and detection was 90 MHz,  $\pi$ -pulse lengths for pumping and detection were 12 and 18 ns, respectively. B: Orientation selective simulations series for PELDOR/DEER experiments with 90 MHz frequency separation and pump position either at the maximum of the EPR line (black) or set 10 G lower (grey). The red line represents a simulation with full excitation of the EPR spectrum. C: Experimental time traces (dots, left), DEER analysis fits (lines, left), their Fourier transformations (middle) and corresponding distance distributions (right). Experimental time traces and distance distributions show no dependence on the experimental setup. The subtle differences in simulations for both setups are not resolved in the experiment.*

The comparison of PELDOR/DEER experiments recorded for both setups (Figure 7-7, C) do not show any significant difference in the

obtained distance distribution, illustrating that there are no residue orientation selection artefacts visible in the experiments. The results illustrate that orientation selection is not observed if broadband excitation is employed.

### 7.2.2 PELDOR Experiments in Solution

For characterization of the sample, experiments were first performed in solvent (MeOH), as peptide concentration can be controlled in this case and peptide aggregation can be minimized. To evaluate the performance of the TOPP label, PELDOR/DEER experiments were performed on WALP24-TOPP and WALP24-MTSSL under the same experimental conditions. The background corrected PELDOR/DEER traces are shown in Figure 7-8. Both experiments resulted in time traces with well visible modulations, however in the case of WALP24-MTSSL multiple frequencies contribute to the dipolar oscillation that give rise to a complex distance distribution. WALP24-TOPP in contrast delivered a much clearer single-peak distance. These findings can be rationalized by molecular modelling. Figure 7-8 displays the molecular models (PyMOL) of both systems. Minimized peptide structures and attached labels were derived as described in § 7.1.3. The distance measured between the two TOPP labels (average of O-O, N-N, O-N and N-O) in the model was 2.33 nm. The distance is represented by a Gaussian (width of  $\pm 0.2$  nm) in the distance distribution. The deviation between model and experiment of  $\approx 0.1$  nm is larger than the error estimated for the experiment ( $\approx \pm 0.05$  nm), which is probably owed to the simplicity of the modelling. For WALP24-MTSSL a conformational ensemble predicted by MMM resulted in the distribution shown in red, and

indicate that MTSSL rotamers are responsible for the complex distance distribution obtained from the EPR distance measurement.

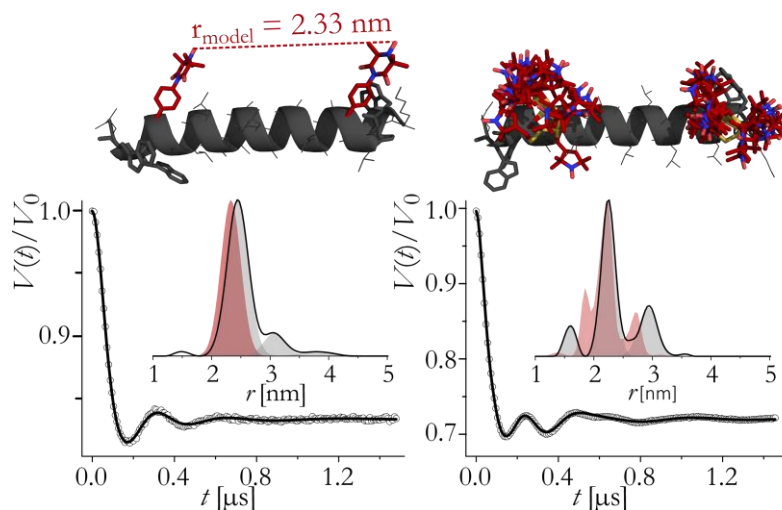


**Figure 7-8: WALP24-MTSSL vs. WALP24-TOPP in MeOH**

*Top: Pymol structures of WALP24-TOPP and WALP24-MTSSL modelled as explained in § 7.1.3 Bottom: PELDOR experiments in methanol. Background corrected PELDOR time traces (dots) and fits using DEERanalysis (black lines) for WALP24-TOPP (left) and WALP24-MTSSL (right). Experimental and modelled distance distributions are shown in comparison (inset, black and red lines).*

### 7.2.3 PELDOR/DEER Experiments in Lipid Environment

The Phospholipids DMPC and POPC were chosen to study the behaviour of WALP24-TOPP and WALP24-MTSSL in lipid environment. While the hydrophobic thickness of POPC ( $r \approx 2.7$  nm)<sup>200</sup> matches well the hydrophobic length of WALP24, DMPC's hydrophobic thickness ( $r \approx 2.3$  nm)<sup>201</sup> creates a positive hydrophobic mismatch. Thus,

these two lipids are suited model systems to compare the capability of the labels to report on peptide structure in different lipid environments.

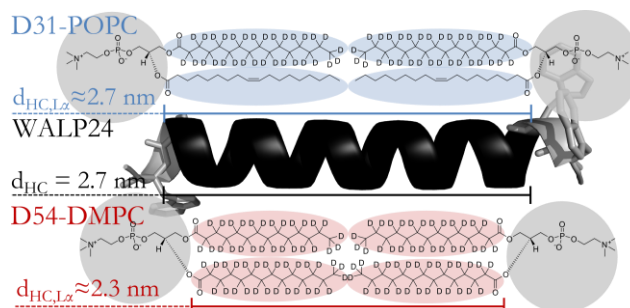


**Figure 7-9: Illustration of WALP24, DMPC and POPC**

*Chemical structure and schematic representation of the deuterated phospholipids D54-DMPC (14:0<sub>2</sub>-d54 PC) and D31-POPC (16:0-d31-18:1 PC) used in this study with their hydrophobic thickness as compared to the length of WALP24.*

Before comparing the behaviour of the WALP24 peptides in the two environments, an extensive study on WALP24-MTSSL in DMPC was performed. To investigate possible aggregation effects, different peptide-to-lipid ratios, from 1-to-250 up to 1-to-3000 were tested and modulation depths  $\Delta$  were evaluated qualitatively. Figure 7-10 shows the PELDOR traces recorded on three samples of different peptide-to-lipid ratios. It can be seen that for the ratio of 1-to-250 electron-spin relaxation time and modulation depth of the PELDOR signal were drastically reduced, indicating the formation of large spin clusters. When the ratio was lowered to 1-to-1500 the spin relaxation time was not significantly affected anymore. However, the modulation depth was increased when compared to the solution state, which is symptomatic for the formation of multi-spin systems as explained in § 2.2.3. The onset of some oligomerization can be concluded from this finding.

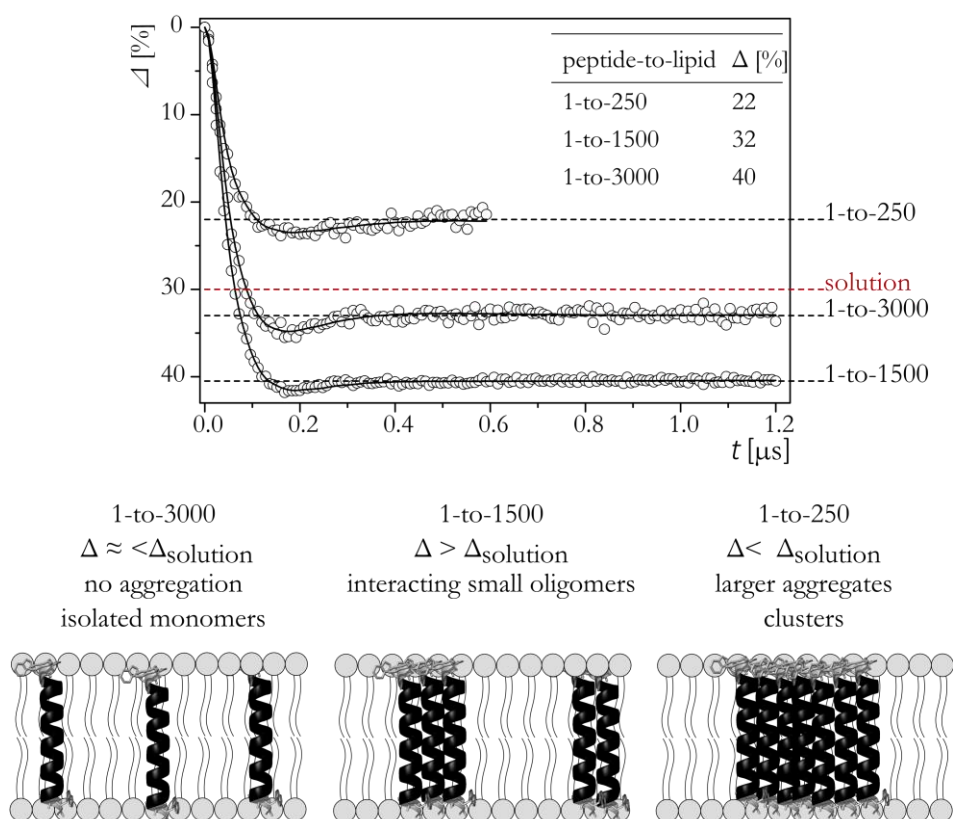


**Figure 7-10: PELDOR Experiments on WALP24-MTSSL in DMPC for Different Peptide-to-Lipid Ratios**

*Top: Background corrected time traces (dots) and DEERanalysis fits (black lines) recorded on samples of varying WALP24-MTSSL-to-DMPC ratio. Dashed lines illustrate corresponding modulation depths observed in the PELDOR/DEER experiments ( $\Delta$  obtained on WALP24-MTSSL in MeOH as shown as red dashed line). Values of  $\Delta$  are given in the inset. Bottom: Qualitative model of aggregation derived from the experiment. At 1-to-3000 peptide-to-lipid ratio  $\Delta$  is comparable to the one in solution indicating the occurrence of isolated monomers. The increased experimental  $\Delta$  at the ratio of 1-to-1500 suggests the formation of small oligomers. Aggregation to large clusters of peptides can be concluded from the decrease of  $\Delta$  and relaxation time  $T_m$  when at a ratio of 1-to-250.*

Further lowering of the ratio to 1-to-3000 resulted in a time trace with a modulation depth comparable to the one observed in methanol. Hence, to exclude oligomerization, which would introduce contributions from intermolecular distances to the PELDOR/DEER experiments, all

distance measurements were performed at ratios around 1-to-3000 or even lower. Additionally, all distance measurements comparing the WALP24 peptides in DMPC vs. POPC were performed in deuterated lipids to increase  $T_m$  and thereby improving the signal-to-noise ratio.

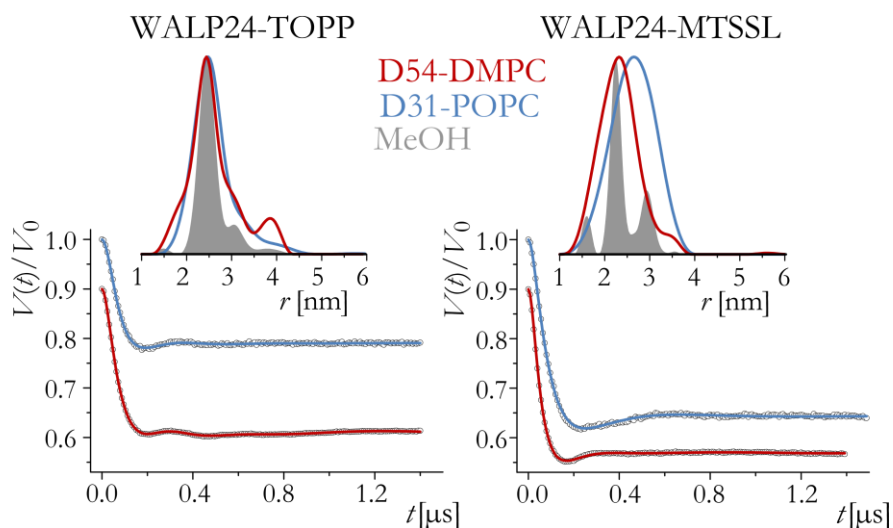


**Figure 7-11: PELDOR Experiment on WALP24-MTSSL vs. WALP24-TOPP in Different Environments**

*PELDOR experiments on WALP24-TOPP (left) and WALP24-MTSSL (right) in different environments. Comparison of dipolar traces recorded in lipid environment (dots) and DEERanalysis fits for D54-DMPC (red) and D31-POPC (blue). Corresponding distance distributions as well as distribution in MeOH (§ 7.2.2) in grey for comparison are shown.*

Figure 7-11 displays a comparison of PELDOR/DEER traces recorded on WALP24-TOPP and WALP24-MTSSL in D54-DMPC and D31-POPC as well as results obtained in solution for comparison. The distance distributions obtained from the experiments are summarized in Table vii and reveal significant differences between the two labels. The main distances reported by the TOPP labelled WALP24 do not show a dependence on the lipid environment within the experimental error. The

width of the distribution is increasing from  $\pm 0.2$  nm in methanol solution to  $\pm 0.4$  nm in lipid environment though.

**Table vii**

*Experimental distances and distributions ( $\Delta r =$  half width at half maximum) of WALP24-TOPP and WALP24-MTSSL in different environments and hydrophobic thickness of the lipids for comparison. \*In the case of WALP24-MTSSL in MeOH the distribution consists of several peaks that cannot be represented by a width of the distribution.*

	hydrophobic thickness lipid	rPELDOR $\pm \Delta r$ [nm]	
		TOPP	MTSSL
MeOH	--	$2.45 \pm 0.2$	2.25*
D31-POPC	2.7 nm	$2.47 \pm 0.4$	$2.65 \pm 0.6$
D54-DMPC	2.3 nm	$2.43 \pm 0.4$	$2.29 \pm 0.5$

The distances reported by WALP24-MTSSL in contrast do show a clear dependence on their environment. In fact the main distances measured on WALP24-MTSSL in MLVs reflect the hydrophobic thickness of the respective lipids.

### 7.3 Discussion of PELDOR Experiments on MTSSL- and TOPP-Labelled WALP24

PELDOR experiments on WALP24 labelled with TOPP vs. MTSSL in methanol solution together with the constructed molecular models gave clear evidence for TOPP's superiority in terms of the conformational space contributed from the label. Interpretation of inter-spin distances using MTSSL labels, in contrast becomes ambiguous. This intrinsic advantage of TOPP becomes even more essential for PELDOR/DEER experiments in the lipid bilayer. In this case, the more flexible MTSSL label reports broad distance distributions. It is significant that the peak



distances correspond to the hydrophobic thicknesses of the lipid environment, suggesting that the flexibility of the MTSSL allows adapting to the membrane thickness by moving towards the nitroxide's favourable electrostatic environment. The insertion of the nitroxide label into the lipid bilayer with a tendency to move to the interface region between the lipids tails and head groups has been reported.<sup>82, 202</sup> This behaviour results in loss of information about the internal peptide structure. Experimental distances obtained from EPR distance measurements on WALP24-TOPP on the other hand do not change with the hydrophobic thickness of DMPC and POPC. From this finding the preservation of the peptide's structure in the different lipids can be concluded, which excludes compression or kinking of the peptide as possible reaction to the mismatch situation (D and E, Figure 4-1). According to the results presented for experiments on samples of varying peptide-to-lipid ratio, aggregation should neither be the main adaption mechanism (C, Figure 4-1). Adaption of the lipid bilayer by stretching its acyl chains as depicted in Figure 4-1, A is a reasonable mechanism, as the influence of tryptophan anchors on bilayer thickness has been proposed.<sup>184</sup> However, this conclusion is contradicted by the presented results with WALP24-MTSSL, which still report  $\approx 2.3$  nm distance in DMPC. Taken together the results point to peptide tilting as an alternative adaptation mechanism that would not alter the inter-spin distance.<sup>179</sup> WALP peptides are known to have an intrinsic tilt angle.<sup>186</sup> STRANDBERG *et al.* determined tilt angles of WALP23 (hydrophobic length = 2.55 nm) to vary slightly but systematically between  $4.5^\circ$  to  $5.5^\circ$  and  $8.2^\circ$  upon insertion into DOPC (18:1<sub>2</sub>), DMPC (14:0<sub>2</sub>) and DLPC (12:0<sub>2</sub>) based on <sup>2</sup>H NMR quadrupolar couplings.<sup>203</sup> While NMR studies observed a tilt angle of  $4.4^\circ$ - $4.8^\circ$  when WALP23 was broad into DOPC

(18:1), a fluorescence investigation on the same system (WALP23 in DOPC) suggested an angle of  $24^\circ \pm 5^\circ$ . The authors argued that the tilt angles determined by NMR are underestimated by the data analysis procedure.<sup>187, 203, 204</sup> After this finding another NMR study used a number of constraints including  $^{13}\text{C}$  and  $^{15}\text{N}$  chemical shift anisotropies and  $^{13}\text{C}$ - $^{15}\text{N}$  dipolar couplings to revise WALP23's tilt angle in DMPC. The tilt angle resulting from this study was  $\approx 21^\circ$  (compared to  $\approx 5^\circ$  in the earlier study) which is in better agreement with MD simulations that predict  $\approx 33^\circ \pm 9^\circ$  for the system.<sup>205, 206</sup> PELDOR/DEER spectroscopy in conjunction with a rigid label like TOPP will be suited for the investigation of the peptide tilt angles in an aligned membrane as the orientation between the inter-spin vector and the magnetic field is naturally encoded in the experiment (§ 8.2).<sup>182</sup> The results obtained in § 7.2 established that the TOPP label is a suited choice for high-resolution distance measurements in transmembrane peptides. PELDOR/DEER studies on WALP23 labelled with MTSSL and gadolinium chelates detected the peptide's  $\alpha$ -helical pitch by systematically varying the labelling position. Adversely, the flexibility of the applied labels led to a rather low resolution with distribution widths on the order of 1-2 nm, which is unfavourably large in proportion to the length of the peptide itself (3-4 nm). The resolution of distance measurements using TOPP is much higher.

## 8. Chapter

### **Conclusion – Perspectives for High Power Q-band PELDOR Using Semi-Rigid Spin Labels**

The results presented in this work demonstrate the capability of high-power Q-band distance measurements by PELDOR/DEER in conjunction with spin labels of reduced mobility. High sensitivity of the distance measurements at Q band combined with high microwave power allows for experiments with biomolecule concentrations of 20–50  $\mu\text{M}$  with lower sample volume, when compared to X band. This is demonstrated by the high signal-to-noise ratio of PELDOR/DEER traces recorded for the two challenging cases of measuring very long distances (up to 8 nm in  $\text{C}^{\text{T}}$ -labelled RNA) and distance measurements in systems with enhanced relaxation (TOPP-labelled WALP24 in lipid bilayer). Additionally, high microwave power, resulting in large excitation bandwidth of the applied pulses, allows to take advantage of measuring accurate distances using restricted labels, without suffering the consequence of orientation selection.

#### **8.1 $\text{C}^{\text{T}}$ label for Distance Measurements in RNA**

High-power Q-band PELDOR/DEER using the  $\text{C}^{\text{T}}$  label offers a simple, model-free approach to measure distances at atomic resolution in RNA. Compared to other nitroxide labels rigidly attached to RNA, the synthetic approach is substantially simplified as it permits the use of commercially available convertible nucleosides to which the TEMPO

label can be attached with high efficiency. The labelling strategy will permit to disentangle more complex rearrangements of larger RNAs and RNA-protein interactions. The combined advancements in spectroscopy and label chemistry will make even larger RNA systems accessible<sup>207</sup> and provide unparalleled insights into macromolecular assemblies. The high-resolution distance ruler for RNA duplexes obtained in § 6.2.2 might have interesting applications in studies of natural systems like tracking of conformational changes upon activation of catalytic nucleic acids. One example shall be introduced in the following section. First results from EPR distance measurements on a  $C^{13}$  labelled RNA-DNA complex illustrate the method's potential for studying conformational equilibria.

While in nature RNA and protein enzymes are used for catalysis, synthetic bimolecular catalysts can be made of DNA as well. The 9DB1 deoxyribozyme is an example of such a DNA-catalyst.<sup>207, 208</sup> It catalyses the regioselective formation of a native phosphodiester bond between the 3'-hydroxyl and the 5'-triphosphate termini of two RNA-strands as illustrated in Figure 8-1, A. The 44 nucleotide long DNA strand contains the minimally required catalytic core of 31 nucleotides to catalyse the reaction. A complex of the 44 nucleotide DNA and a 15 nucleotide long RNA could be crystallized in its post-catalytic state.<sup>209</sup> The resulting structure is shown in Figure 8-1, B. Overall the folding unit is stabilized by numerous tertiary interactions, including extensive contacts to the ligation junction shown in light blue. Five duplexes P1 to P5 are formed, with P2 and P3 are formed within the DNA strand and P1 and P4 as RNA-DNA hybrid duplexes. Additionally there are some long-range Watson-Crick base pairs. To compare the structure determined with x-ray crystallography with the conformation in frozen solution,  $C^{13}$

was introduced at two positions in the RNA strand. The structure of the complex with  $C^T$  sitting in the RNA strand of P1 and P4 is shown in Figure 8-1, C. The distance between the nitroxide moieties extracted from the model is 2.85 nm.

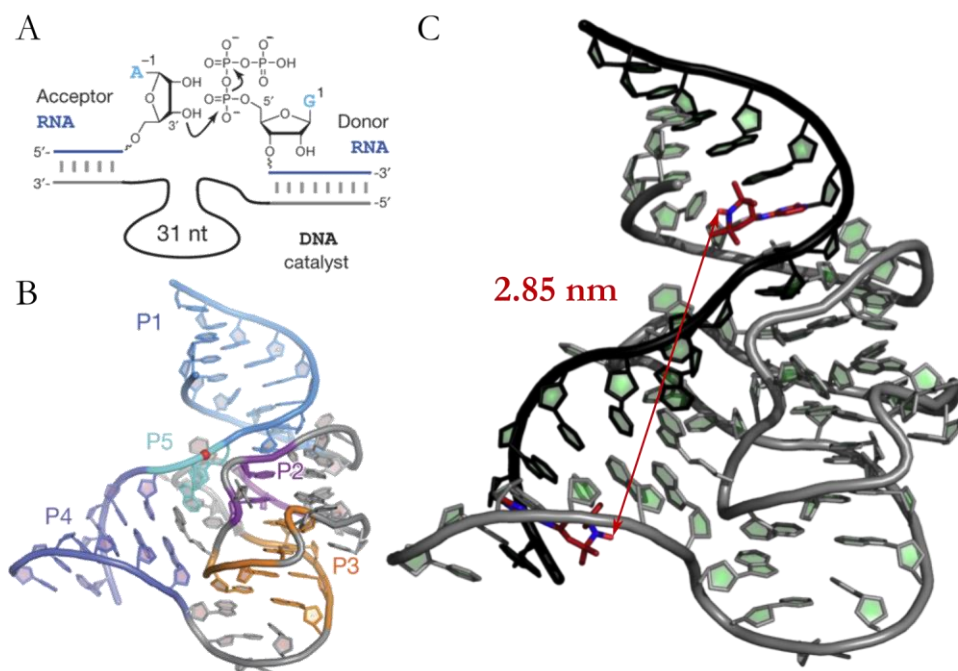


**Figure 8-1: Architecture of the Deoxyribozyme 9DB1**

*A: Ligation between RNAs' 3'-OH and 5'-phosphate (blue) catalysed by the DNA (black: catalytic core of 31 nucleotides). B: Resulting crystal structure: cartoon representation of the deoxyribozyme in complex with the ligated RNA product. C: Crystal structure of 9DB1 with the  $C^T$  labels attached in its preferred conformation (conformation 2, Table iii).*

However, the first PELDOR experiment performed on the  $C^T$  labelled complex revealed a complex distance distribution with the three distances of 3.49, 2.87 and 1.93 nm (Figure 8-2, black line). This experimental finding suggests that in frozen solution 9DB1 is represented by a conformational ensemble, with the conformation,

giving rise to the distance peak of highest intensity (3.49 nm), not matching the distance expected from with the crystal structure. To elucidate whether the equilibrium between multiple conformations is influenced by sample preparation three additional samples were prepared. The conditions are summarised in Table viii.

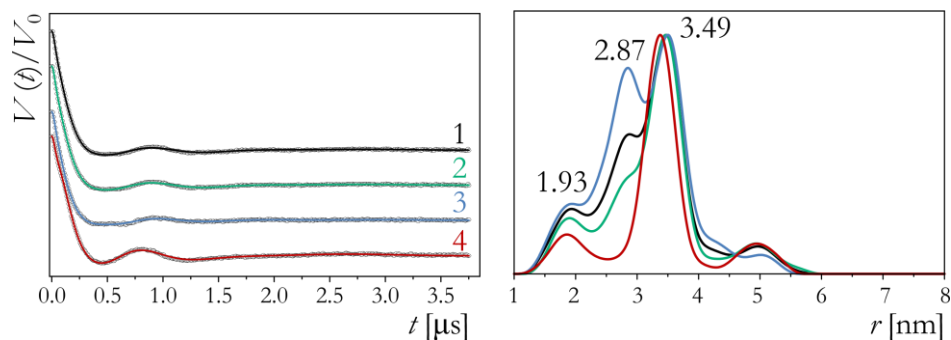


**Figure 8-2: PELDOR Traces Recorded on 9DB1**

*Left: PELDOR/DEER traces recorded on  $C^T$ -labelled 9DB1-RNA complex (dots) and DEERanalysis fits (lines). Four different sample conditions as denoted in Table viii were employed. Bottom: Distance distributions obtained from the four traces according to colour code. Distributions are scaled to the peak around 3.49 nm. Observation of the distance around 2.87 nm, which is expected from the crystal structure, is very much dependent on the sample conditions.*

Inspection of the distributions resulting from the four experiments reveals that the proportion of the distance expected from the crystal structure is strongly dynamic. However a dramatic change is observed when the magnesium concentration in the buffer is increased from 20 to 80 mM. The peak around 2.87 nm, which is in agreement with the crystal structure, is not observed in this PELDOR/DEER experiment (Figure 8-2, red line).

**Table viii**

*Conditions employed for the four different samples (1-4) for PELDOR/DEER experiments on the C<sup>T</sup>-labelled 9DB1-RNA complex (rt...room temperature)*

#	c <sub>RNA</sub> (μM)	c <sub>MgCl<sub>2</sub></sub> (mM)	Freezing conditions
1	50	20	rt → frozen in N <sub>2</sub> (l)
2	50	20	= 1, reheated to 50°C, 15 min @ rt, 1 h @ 4°C, frozen in N <sub>2</sub> (l)
3	25	20	rt → frozen in N <sub>2</sub> (l)
4	25	80	rt → frozen in N <sub>2</sub> (l)

The observation of conformational dynamics in this complex is an exciting application for the PELDOR experiments in conjunction with the C<sup>T</sup> label, illustrating the contribution pulsed EPR spectroscopy can offer to understanding RNA structure and function.

## 8.2 TOPP Label for Investigation of Peptide Structure in Lipid Bilayers

Owing to its restricted mobility the TOPP label is a better reporter for monitoring peptide structures and structural changes by inter-spin distance measurements than standard labels like MTSSL that contribute a large conformational space to the distance distribution. The TOPP-labelled WALP24 is a promising tool to systematically study hydrophobic mismatch, by varying parameters like the label positions within the peptide, peptide-to-lipid ratio, the peptide length and the hydrophobic thickness of the lipid. PELDOR spectroscopy offers tools for monitoring all adaption mechanisms presented in § 4.1.2. Even though only an adaption of the peptide length and kinking (Figure 4-1/

8-3, D and E) should alter the experimental distance observed under match or mismatch conditions, also situations A-C presented in Figure 4-1/Figure 8-3 can be differentiated by the experiment. Possible aggregation propensity of the peptides can be studied by evaluation of the modulation depth as explained in § 2.2.1.

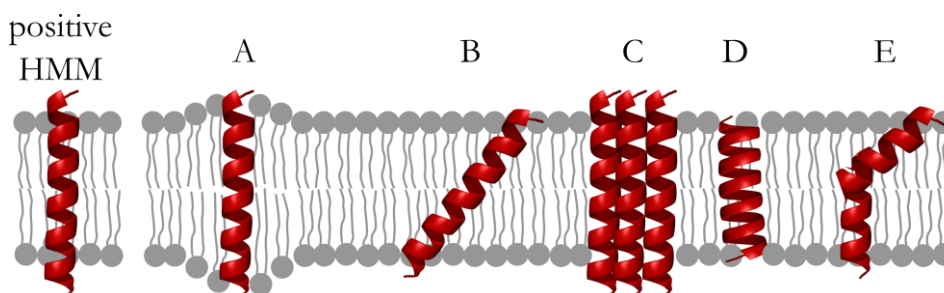


**Figure 8-3: Illustration of Possible Reactions to Hydrophobic Mismatch**

*Illustration of possible reaction mechanisms for the case when the helix's hydrophobic length is exceeding the hydrophobic thickness of the lipid bilayer, also known as positive hydrophobic mismatch (HMM), adapted from reference<sup>179</sup> A: Stretching of the lipids acyl chains. B: Tilting of the helix. C: Aggregation of helices. D) Distortion/deformation of the helix backbone E: Kinking of the backbone*

The rigidity of the TOPP label provides the intrinsic advantage that the dipolar vector between the two labels has a well-defined orientation in space towards the peptide axis, and therefore also towards the membrane axis if the peptide adapts to a defined orientation within the lipid bilayer. This orientation could be naturally measured by PELDOR/DEER, if the membrane is oriented in the magnetic field.<sup>182</sup> Figure 8-4 schematically illustrates the concept of measuring a helix tilt angle in a membrane. As discussed in § 2.1.1 the strength of the dipolar coupling will depend on the angle  $\theta$  between the inter-spin vector  $\mathbf{r}_{AB}$  and the external magnetic field  $B_0$  (Figure 8-4, A).



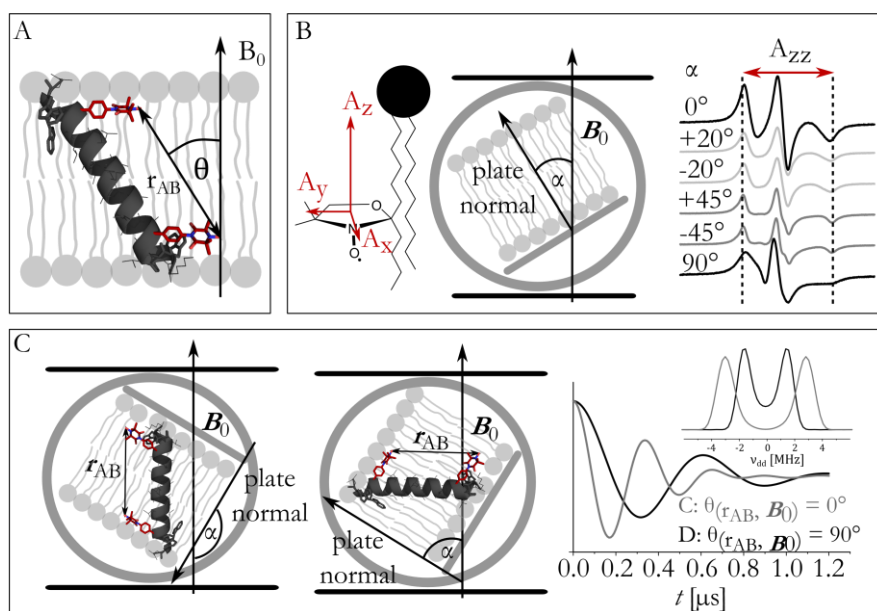


**Figure 8-4: Determination of a Helix Tilt Angle in a Membrane**

*A: Pymol model of WALP24-TOPP in an aligned membrane. Due to the rigidity of the TOPP-label the inter-spin vector  $r_{AB}$  has a fixed orientation towards the helix axis. If the peptide is inserted in an aligned membrane, the angle  $\theta$  between  $r_{AB}$  and the internal magnetic field  $B_0$  can be determined according to chapter 2.1.1. B: Representation of a TOAC labelled lipid (14-PC) and the orientation of TOAC's  $A$ -tensor in the nitroxide's molecular frame. (left) Schematic top view of an EPR tube containing a glass plate with a sample of 14-PC in an aligned membrane. The tube is positioned with a known angle  $\alpha$  between the plate normal and the external magnetic field (middle). Due to the anisotropy of the  $A$ -tensor, the size of the hyperfine splitting observed in the EPR experiment will change upon rotation of the EPR tube. cw-EPR spectra recorded at X band on a sample of 14-PC in an aligned membranes are shown on the right. The clear dependence of the size of the hyperfine splitting on  $\alpha$ , illustrates a reasonable membrane alignment. C: Schematic top view of an EPR tube containing a glass plate with a sample of WALP24-TOPP in an aligned membrane. The frequency distribution of the resulting PELDOR/DEER time trace and its Fourier transformation. If the sample is positioned in the spectrometer having the  $r_{AB}$  parallel to the  $B_0$  (left) the largest dipolar frequency will be observed (right, grey line). Rotation of the EPR tube of  $90^\circ$  will result in a dipolar frequency half that value (D).*

When a sample of WALP24-TOPP in an aligned membrane (on a glass plate) is broad into the magnetic field a systematic change of the direction of the membrane normal (which is parallel to the glass plate's

normal) towards  $\mathbf{B}_0$  will result in a systematic change in the dipolar frequency distribution (Figure 8-4, C). The direction of  $\mathbf{r}_{AB}$  towards the membrane normal and ultimately the tilt angle of the helix, can be extracted from the experiment. The quality of membrane alignment will determine the resolution of the experiment. Using spin-labelled lipids (14-PC (Figure 8-4, C left) and measuring the size of the strongly anisotropic  $^{14}\text{N}$  hyperfine coupling and its distribution, which depends on the tilt angle of the lipids, can uncomplicatedly test the degree of alignment. Indeed, elaborate protocols for alignment can be found in literature<sup>210, 211</sup> and initial tests have shown that reasonable alignment might be achievable on glass plates using spin coating (Figure 8-4, C right).

The benefits discussed here highlight how high-power Q-band PELDOR/DEER experiments on TOPP labelled WALP peptides is a promising method for contributing to the understanding mechanisms underlying hydrophobic mismatch.

## Bibliography

1. Shi, Y. (2014) A glimpse of structural biology through X-ray crystallography, *Cell* 159, 995-1014.
2. Kendrew, J. C., Bodo, G., Dintzis, H. M., Parrish, R. G., Wyckoff, H., and Phillips, D. C. (1958) A Three-Dimensional Model of the Myoglobin Molecule Obtained by X-Ray Analysis, *Nature* 181, 662-666.
3. [www.rcsb.org](http://www.rcsb.org).
4. H.M. Berman, J. W., Z. Feng, G. Gilliland, T.N. Bhat, H. Weissig, I.N. Shindyalov, P.E. Bourne. (2000) The Protein Data Bank, *Nucleic Acids Research* 28, 235-242.
5. Gavira, J. A. (2016) Current trends in protein crystallization, *Archives of Biochemistry and Biophysics* 602, 3-11.
6. Carlon, A., Ravera, E., Andralojc, W., Parigi, G., Murshudov, G. N., and Luchinat, C. (2016) How to tackle protein structural data from solution and solid state: An integrated approach, *Progress in Nuclear Magnetic Resonance Spectroscopy* 92-93, 54-70.
7. Nogales, E. (2016) The development of cryo-EM into a mainstream structural biology technique, *Nature Methods* 13, 24-27.
8. Schuler, B., Soranno, A., Hofmann, H., and Nettels, D. (2016) Single-Molecule FRET Spectroscopy and the Polymer Physics of Unfolded and Intrinsically Disordered Proteins, *Annual Review of Biophysics* 45, 207-231.
9. Sustarsic, M., and Kapanidis, A. N. (2015) Taking the ruler to the jungle: single-molecule FRET for understanding biomolecular structure and dynamics in live cells, *Current opinion in structural biology* 34, 52-59.
10. Weisenburger, S., Jing, B., Hanni, D., Reymond, L., Schuler, B., Renn, A., and Sandoghdar, V. (2014) Cryogenic colocalization microscopy for nanometer-distance measurements, *Chemphyschem : a European journal of chemical physics and physical chemistry* 15, 763-770.
11. Altenbach, C., Flitsch, S. L., Khorana, H. G., and Hubbell, W. L. (1989) Structural studies on transmembrane proteins. 2. Spin labeling of bacteriorhodopsin mutants at unique cysteines, *Biochemistry* 28, 7806-7812.
12. Bennati, M., and Prisner, T. F. (2005) New developments in high field electron paramagnetic resonance with applications in structural biology, *Reports on Progress in Physics* 68, 411-448.
13. Telser, J., Krzystek, J., and Ozarowski, A. (2014) High-frequency and high-field electron paramagnetic resonance (HFEPFR): a new spectroscopic tool for bioinorganic chemistry, *JBIC Journal of Biological Inorganic Chemistry* 19, 297-318.
14. Feher, G. (1956) Observation of Nuclear Magnetic Resonances via the Electron Spin Resonance Line, *Physical Review* 103, 834-835.
15. L. Kevan, L. D. K. (1976) Electron nuclear double resonance, *Wiley: New York*.
16. Cutsail Iii, G. E., Telser, J., and Hoffman, B. M. (2015) Advanced paramagnetic resonance spectroscopies of iron-sulfur proteins: Electron nuclear double resonance (ENDOR) and electron spin echo envelope modulation (ESEEM), *Biochimica et Biophysica Acta (BBA) - Molecular Cell Research* 1853, 1370-1394.

17. Stich, T. A., Myers, W. K., and Britt, R. D. (2014) Paramagnetic intermediates generated by radical S-adenosylmethionine (SAM) enzymes, *Accounts of chemical research* 47, 2235-2243.
18. Fielding, A. J., Parey, K., Ermler, U., Scheller, S., Jaun, B., and Bennati, M. (2013) Advanced electron paramagnetic resonance on the catalytic iron-sulfur cluster bound to the CCG domain of heterodisulfide reductase and succinate: quinone reductase, *Journal of Biological Inorganic Chemistry* 18, 905-915.
19. Nick, T. U., Lee, W., Kossmann, S., Neese, F., Stubbe, J., and Bennati, M. (2015) Hydrogen bond network between amino acid radical intermediates on the proton-coupled electron transfer pathway of E. coli alpha2 ribonucleotide reductase, *Journal of the American Chemical Society* 137, 289-298.
20. Schiemann, O., and Prisner, T. F. (2007) Long-range distance determinations in biomacromolecules by EPR spectroscopy, *Quarterly reviews of biophysics* 40, 1-53.
21. Borbat, P. P., and Freed, J. H. (2013) Pulse Dipolar Electron Spin Resonance: Distance Measurements, In *Structural Information from Spin-Labels and Intrinsic Paramagnetic Centres in the Biosciences* (Timmel, R. C., and Harmer, R. J., Eds.), pp 1-82, Springer Berlin Heidelberg, Berlin, Heidelberg.
22. Milov, A. D., Tsvetkov, Y. D., Raap, J., De Zotti, M., Formaggio, F., and Toniolo, C. (2016) Review conformation, self-aggregation, and membrane interaction of peptaibols as studied by pulsed electron double resonance spectroscopy, *Peptide Science* 106, 6-24.
23. Ciecierska-Tworek, Z., Van, S. P., and Griffith, O. H. (1973) Electron-electron dipolar splitting anisotropy of a dinitroxide oriented in a crystalline matrix, *Journal of Molecular Structure* 16, 139-148.
24. Dong, G., Wang, H., Cong, J., Wang, C., Guo, J., Zhang, T., Yang, J., Yang, G., and Wu, K. (2015) Calibration ruler for CW-EPR distance measurement using diradical molecule of rigid structure, *Acta Biochimica et Biophysica Sinica* 47, 342-348.
25. Steinhoff, H. J., Radzwill, N., Thevis, W., Lenz, V., Brandenburg, D., Antson, A., Dodson, G., and Wollmer, A. (1997) Determination of interspin distances between spin labels attached to insulin: comparison of electron paramagnetic resonance data with the X-ray structure, *Biophysical journal* 73, 3287-3298.
26. Sahu, I. D., Hustedt, E. J., Ghimire, H., Inbaraj, J. J., McCarrick, R. M., and Lorigan, G. A. (2014) CW dipolar broadening EPR spectroscopy and mechanically aligned bilayers used to measure distance and relative orientation between two TOAC spin labels on an antimicrobial peptide, *Journal of magnetic resonance* 249, 72-79.
27. Edwards, D. T., Ma, Z., Meade, T. J., Goldfarb, D., Han, S., and Sherwin, M. S. (2013) Extending the distance range accessed with continuous wave EPR with Gd<sup>3+</sup> spin probes at high magnetic fields, *Physical Chemistry Chemical Physics* 15, 11313-11326.
28. Kurshev, V. V., Astashkin, A. V., and Raitsimring, A. M. (1988) Modulation effects in A 2+1 electron spin echo pulse sequence, *Journal of Structural Chemistry* 29, 62-68.
29. Borbat, P. P., and Freed, J. H. (1999) Multiple-quantum ESR and distance measurements, *Chemical Physics Letters* 313, 145-154.

30. Saxena, S., and Freed, J. H. (1996) Double quantum two-dimensional Fourier transform electron spin resonance: Distance measurements, *Chemical Physics Letters* 251, 102-110.
31. Orlando, B. J., Borbat, P. P., Georgieva, E. R., Freed, J. H., and Malkowski, M. G. (2015) Pulsed Dipolar Spectroscopy Reveals That Tyrosyl Radicals Are Generated in Both Monomers of the Cyclooxygenase-2 Dimer, *Biochemistry* 54, 7309-7312.
32. Jeschke, G., Pannier, M., Godt, A., and Spiess, H. W. (2000) Dipolar spectroscopy and spin alignment in electron paramagnetic resonance, *Chemical Physics Letters* 331, 243-252.
33. Kulik, L. V., Dzuba, S. A., Grigoryev, I. A., and Tsvetkov, Y. D. (2001) Electron dipole-dipole interaction in ESEEM of nitroxide biradicals, *Chemical Physics Letters* 343, 315-324.
34. Milikisyants, S., Scarpelli, F., Finiguerra, M. G., Ubbink, M., and Huber, M. (2009) A pulsed EPR method to determine distances between paramagnetic centers with strong spectral anisotropy and radicals: The dead-time free RIDME sequence, *Journal of magnetic resonance* 201, 48-56.
35. Abdullin, D., Duthie, F., Meyer, A., Müller, E. S., Hagelueken, G., and Schiemann, O. (2015) Comparison of PELDOR and RIDME for Distance Measurements between Nitroxides and Low-Spin Fe(III) Ions, *The Journal of Physical Chemistry B* 119, 13534-13542.
36. Meyer, A., Abdullin, D., Schnakenburg, G., and Schiemann, O. (2016) Single and double nitroxide labeled bis(terpyridine)-copper(II): influence of orientation selectivity and multispin effects on PELDOR and RIDME, *Physical Chemistry Chemical Physics* 18, 9262-9271.
37. Collauto, A., Frydman, V., Lee, M. D., Abdelkader, E. H., Feintuch, A., Swarbrick, J. D., Graham, B., Otting, G., and Goldfarb, D. (2016) RIDME distance measurements using Gd(III) tags with a narrow central transition, *Physical Chemistry Chemical Physics*.
38. Spindler, P. E., Zhang, Y., Endeward, B., Gershernzon, N., Skinner, T. E., Glaser, S. J., and Prisner, T. F. (2012) Shaped optimal control pulses for increased excitation bandwidth in EPR, *Journal of magnetic resonance* 218, 49-58.
39. Borbat, P. P., Georgieva, E. R., and Freed, J. H. (2013) Improved Sensitivity for Long-Distance Measurements in Biomolecules: Five-Pulse Double Electron-Electron Resonance, *The journal of physical chemistry letters* 4, 170-175.
40. Doll, A., Pribitzer, S., Tschaggelar, R., and Jeschke, G. (2013) Adiabatic and fast passage ultra-wideband inversion in pulsed EPR, *Journal of magnetic resonance* 230, 27-39.
41. Spindler, P. E., Glaser, S. J., Skinner, T. E., and Prisner, T. F. (2013) Broadband Inversion PELDOR Spectroscopy with Partially Adiabatic Shaped Pulses, *Angewandte Chemie International Edition* 52, 3425-3429.
42. Doll, A., and Jeschke, G. (2014) Fourier-transform electron spin resonance with bandwidth-compensated chirp pulses, *Journal of magnetic resonance* 246, 18-26.
43. Doll, A., Qi, M., Pribitzer, S., Wili, N., Yulikov, M., Godt, A., and Jeschke, G. (2015) Sensitivity enhancement by population transfer in Gd(III) spin labels, *Physical chemistry chemical physics : PCCP* 17, 7334-7344.

44. Jeschke, G., Pribitzer, S., and Doll, A. (2015) Coherence Transfer by Passage Pulses in Electron Paramagnetic Resonance Spectroscopy, *The journal of physical chemistry. B* 119, 13570-13582.
45. Schöps, P., Spindler, P. E., Marko, A., and Prisner, T. F. (2015) Broadband spin echoes and broadband SIFTER in EPR, *Journal of magnetic resonance* 250, 55-62.
46. Segawa, T. F., Doll, A., Pribitzer, S., and Jeschke, G. (2015) Copper ESEEM and HYSCORE through ultra-wideband chirp EPR spectroscopy, *Journal of Chemical Physics* 143, 044201.
47. Spindler, P. E., Waclawska, I., Endeward, B., Plackmeyer, J., Ziegler, C., and Prisner, T. F. (2015) Carr–Purcell Pulsed Electron Double Resonance with Shaped Inversion Pulses, *The journal of physical chemistry letters* 6, 4331-4335.
48. Milov, A. D., Ponomarev, A. B., and Tsvetkov, Y. D. (1984) Electron-electron double resonance in electron spin echo: Model biradical systems and the sensitized photolysis of decalin, *Chemical Physics Letters* 110, 67-72.
49. Martin, R. E., Pannier, M., Diederich, F., Gramlich, V., Hubrich, M., and Spiess, H. W. (1998) Determination of End-to-End Distances in a Series of TEMPO Diradicals of up to 2.8 nm Length with a New Four-Pulse Double Electron Electron Resonance Experiment, *Angewandte Chemie International Edition* 37, 2833-2837.
50. Pannier, M., Veit, S., Godt, A., Jeschke, G., and Spiess, H. W. (2000) Dead-time free measurement of dipole-dipole interactions between electron spins, *Journal of magnetic resonance* 142, 331-340.
51. Tait, C. E., and Stoll, S. (2016) Coherent pump pulses in Double Electron Electron Resonance spectroscopy, *Physical chemistry chemical physics : PCCP* 18, 18470-18485.
52. Reginsson, Gunnar W., and Schiemann, O. (2011) Pulsed electron–electron double resonance: beyond nanometre distance measurements on biomacromolecules, *Biochemical Journal* 434, 353-363.
53. Raitsimring, A., Crepeau, R. H., and Freed, J. H. (1995) Nuclear modulation effects in “2+1” electron spin-echo correlation spectroscopy, *The Journal of Chemical Physics* 102, 8746-8762.
54. Milov, A. D., Maryasov, A. G., and Tsvetkov, Y. D. (1998) Pulsed electron double resonance (PELDOR) and its applications in free-radicals research, *Applied Magnetic Resonance* 15, 107-143.
55. Jeschke, G. (2002) Distance Measurements in the Nanometer Range by Pulse EPR, *ChemPhysChem* 3, 927-932.
56. Milov, A. D., Tsvetkov, Y. D., Formaggio, F., Crisma, M., Toniolo, C., and Raap, J. (2000) Self-Assembling Properties of Membrane-Modifying Peptides Studied by PELDOR and CW-ESR Spectroscopies, *Journal of the American Chemical Society* 122, 3843-3848.
57. Bode, B. E., Margraf, D., Plackmeyer, J., Dürner, G., Prisner, T. F., and Schiemann, O. (2007) Counting the Monomers in Nanometer-Sized Oligomers by Pulsed Electron–Electron Double Resonance, *Journal of the American Chemical Society* 129, 6736-6745.
58. Larsen, R. G., and Singel, D. J. (1993) Double electron–electron resonance spin–echo modulation: Spectroscopic measurement of electron spin pair separations in orientationally disordered solids, *The Journal of Chemical Physics* 98, 5134-5146.

59. Denysenkov, V. P., Prisner, T. F., Stubbe, J., and Bennati, M. (2006) High-field pulsed electron–electron double resonance spectroscopy to determine the orientation of the tyrosyl radicals in ribonucleotide reductase, *Proceedings of the National Academy of Sciences* 103, 13386-13390.
60. Sicoli, G., Argirević, T., Stubbe, J., Tkach, I., and Bennati, M. (2009) Effects in 94 GHz Orientation-Selected PELDOR on a Rigid Pair of Radicals with Non-Collinear Axes, *Applied Magnetic Resonance* 37, 539-548.
61. Stevens, M. A., McKay, J. E., Robinson, J. L. S., El Mkami, H., Smith, G. M., and Norman, D. G. (2016) The use of the Rx spin label in orientation measurement on proteins, by EPR, *Physical Chemistry Chemical Physics* 18, 5799-5806.
62. Tkach, I., Pornsuwan, S., Hobartner, C., Wachowius, F., Sigurdsson, S. T., Baranova, T. Y., Diederichsen, U., Sicoli, G., and Bennati, M. (2013) Orientation selection in distance measurements between nitroxide spin labels at 94 GHz EPR with variable dual frequency irradiation, *Physical Chemistry Chemical Physics* 15, 3433-3437.
63. Tkach, I., Halbmaier, K., Höbartner, C., and Bennati, M. (2014) High-frequency 263 GHz PELDOR, *Applied Magnetic Resonance* 45, 969-979.
64. Jeschke, G., Chechik, V., Ionita, P., Godt, A., Zimmermann, H., Banham, J., Timmel, C. R., Hilger, D., and Jung, H. (2006) DeerAnalysis2006—a comprehensive software package for analyzing pulsed ELDOR data, *Applied Magnetic Resonance* 30, 473-498.
65. Ward, R., Bowman, A., Sozudogru, E., El-Mkami, H., Owen-Hughes, T., and Norman, D. G. (2010) EPR distance measurements in deuterated proteins, *Journal of magnetic resonance* 207, 164-167.
66. Chiang, Y. W., Borbat, P. P., and Freed, J. H. (2005) The determination of pair distance distributions by pulsed ESR using Tikhonov regularization, *Journal of magnetic resonance* 172, 279-295.
67. Altenbach, C., Marti, T., Khorana, H., and Hubbell, W. (1990) Transmembrane protein structure: spin labeling of bacteriorhodopsin mutants, *Science* 248, 1088-1092.
68. Hubbell, W. L., Lopez, C. J., Altenbach, C., and Yang, Z. (2013) Technological advances in site-directed spin labeling of proteins, *Current opinion in structural biology* 23, 725-733.
69. Roser, P., Schmidt, M. J., Drescher, M., and Summerer, D. (2016) Site-directed spin labeling of proteins for distance measurements in vitro and in cells, *Organic & Biomolecular Chemistry* 14, 5468-5476.
70. Barthelmes, D., Granz, M., Barthelmes, K., Allen, K. N., Imperiali, B., Prisner, T., and Schwalbe, H. (2015) Encoded loop-lanthanide-binding tags for long-range distance measurements in proteins by NMR and EPR spectroscopy, *Journal of Biomolecular NMR* 63, 275-282.
71. Ching, H. Y., Mascali, F. C., Bertrand, H. C., Bruch, E. M., Demay-Drouhard, P., Rasia, R. M., Policar, C., Tabares, L. C., and Un, S. (2016) The Use of Mn(II) Bound to His-tags as Genetically Encodable Spin-Label for Nanometric Distance Determination in Proteins, *The journal of physical chemistry letters* 7, 1072-1076.
72. Liu, C. C., and Schultz, P. G. (2010) Adding new chemistries to the genetic code, *Annual Review of Biochemistry* 79, 413-444.

73. Fleissner, M. R., Brustad, E. M., Kálai, T., Altenbach, C., Cascio, D., Peters, F. B., Hideg, K., Peuker, S., Schultz, P. G., and Hubbell, W. L. (2009) Site-directed spin labeling of a genetically encoded unnatural amino acid, *Proceedings of the National Academy of Sciences* 106, 21637-21642.
74. Schmidt, M. J., Borbas, J., Drescher, M., and Summerer, D. (2014) A genetically encoded spin label for electron paramagnetic resonance distance measurements, *Journal of the American Chemical Society* 136, 1238-1241.
75. Shelke, S. A., and Sigurdsson, S. T. (2012) Site-Directed Spin Labelling of Nucleic Acids, *European Journal of Organic Chemistry* 2012, 2291-2301.
76. Bagryanskaya, E. G., Krumkacheva, O. A., Fedin, M. V., and Marque, S. R. (2015) Development and Application of Spin Traps, Spin Probes, and Spin Labels, *Methods in enzymology* 563, 365-396.
77. Babaylova, E. S., Malygin, A. A., Lomzov, A. A., Pyshnyi, D. V., Yulikov, M., Jeschke, G., Krumkacheva, O. A., Fedin, M. V., Karpova, G. G., and Bagryanskaya, E. G. (2016) Complementary-addressed site-directed spin labeling of long natural RNAs, *Nucleic Acids Research*.
78. Yulikov, M. (2015) Chapter 1 Spectroscopically orthogonal spin labels and distance measurements in biomolecules, In *Electron Paramagnetic Resonance: Volume 24*, pp 1-31, The Royal Society of Chemistry.
79. Cunningham, T. F., Putterman, M. R., Desai, A., Horne, W. S., and Saxena, S. (2015) The double-histidine Cu(2)(+)-binding motif: a highly rigid, site-specific spin probe for electron spin resonance distance measurements, *Angewandte Chemie* 54, 6330-6334.
80. Raitsimring, A. M., Gunanathan, C., Potapov, A., Efremenko, I., Martin, J. M. L., Milstein, D., and Goldfarb, D. (2007) Gd<sup>3+</sup> Complexes as Potential Spin Labels for High Field Pulsed EPR Distance Measurements, *Journal of the American Chemical Society* 129, 14138-14139.
81. Song, Y., Meade, T. J., Astashkin, A. V., Klein, E. L., Enemark, J. H., and Raitsimring, A. (2011) Pulsed dipolar spectroscopy distance measurements in biomacromolecules labeled with Gd(III) markers, *Journal of magnetic resonance* 210, 59-68.
82. Matalon, E., Huber, T., Hagelueken, G., Graham, B., Frydman, V., Feintuch, A., Otting, G., and Goldfarb, D. (2013) Gadolinium(III) spin labels for high-sensitivity distance measurements in transmembrane helices, *Angewandte Chemie* 52, 11831-11834.
83. Yagi, H., Banerjee, D., Graham, B., Huber, T., Goldfarb, D., and Otting, G. (2011) Gadolinium tagging for high-precision measurements of 6 nm distances in protein assemblies by EPR, *Journal of the American Chemical Society* 133, 10418-10421.
84. Martorana, A., Bellapadrone, G., Feintuch, A., Di Gregorio, E., Aime, S., and Goldfarb, D. (2014) Probing protein conformation in cells by EPR distance measurements using Gd<sup>3+</sup> spin labeling, *Journal of the American Chemical Society* 136, 13458-13465.
85. Theillet, F. X., Binolfi, A., Bekei, B., Martorana, A., Rose, H. M., Stuiver, M., Verzini, S., Lorenz, D., van Rossum, M., Goldfarb, D., and Selenko, P. (2016) Structural disorder of monomeric alpha-synuclein persists in mammalian cells, *Nature* 530, 45-50.
86. Owenius, R., Eaton, G. R., and Eaton, S. S. (2005) Frequency (250 MHz to 9.2 GHz) and viscosity dependence of electron spin relaxation of



- triarylmethyl radicals at room temperature, *Journal of magnetic resonance* 172, 168-175.
87. Fielding, A. J., Carl, P. J., Eaton, G. R., and Eaton, S. S. (2005) Multifrequency EPR of four triarylmethyl radicals, *Applied Magnetic Resonance* 28, 231-238.
  88. Kuzhelev, A. A., Strizhakov, R. K., Krumkacheva, O. A., Polienko, Y. F., Morozov, D. A., Shevelev, G. Y., Pyshnyi, D. V., Kirilyuk, I. A., Fedin, M. V., and Bagryanskaya, E. G. (2016) Room-temperature electron spin relaxation of nitroxides immobilized in trehalose: Effect of substituents adjacent to NO-group, *Journal of magnetic resonance* 266, 1-7.
  89. Meyer, V., Swanson, M. A., Clouston, L. J., Boratynski, P. J., Stein, R. A., McHaourab, H. S., Rajca, A., Eaton, S. S., and Eaton, G. R. (2015) Room-temperature distance measurements of immobilized spin-labeled protein by DEER/PELDOR, *Biophysical journal* 108, 1213-1219.
  90. Reginsson, G. W., Kunjir, N. C., Sigurdsson, S. T., and Schiemann, O. (2012) Trityl radicals: spin labels for nanometer-distance measurements, *Chemistry* 18, 13580-13584.
  91. Yang, Z., Liu, Y., Borbat, P., Zweier, J. L., Freed, J. H., and Hubbell, W. L. (2012) Pulsed ESR dipolar spectroscopy for distance measurements in immobilized spin labeled proteins in liquid solution, *Journal of the American Chemical Society* 134, 9950-9952.
  92. Fielding, A. J., Concilio, M. G., Heaven, G., and Hollas, M. A. (2014) New developments in spin labels for pulsed dipolar EPR, *Molecules* 19, 16998-17025.
  93. Jagtap, A. P., Krstic, I., Kunjir, N. C., Hänsel, R., Prisner, T. F., and Sigurdsson, S. T. (2015) Sterically shielded spin labels for in-cell EPR spectroscopy: Analysis of stability in reducing environment, *Free Radical Research* 49, 78-85.
  94. Le Breton, N., Martinho, M., Kabytaev, K., Topin, J., Mileo, E., Blocquel, D., Habchi, J., Longhi, S., Rockenbauer, A., Golebiowski, J., Guigliarelli, B., Marque, S. R., and Belle, V. (2014) Diversification of EPR signatures in Site Directed Spin Labeling using a beta-phosphorylated nitroxide, *Physical chemistry chemical physics : PCCP* 16, 4202-4209.
  95. Dzuba, S. A., Maryasov, A. G., Salikhov, K. M., and Tsvetkov, Y. D. (1984) Superslow rotations of nitroxide radicals studied by pulse EPR spectroscopy, *Journal of Magnetic Resonance (1969)* 58, 95-117.
  96. Kathirvelu, V., Smith, C., Parks, C., Mannan, M. A., Miura, Y., Takeshita, K., Eaton, S. S., and Eaton, G. R. (2009) Relaxation rates for spirocyclohexyl nitroxyl radicals are suitable for interspin distance measurements at temperatures up to about 125 K, *Chemical Communications*, 454-456.
  97. Kirilyuk, I. A., Bobko, A. A., Semenov, S. V., Komarov, D. A., Irtegov, I. G., Grigor'ev, I. A., and Bagryanskaya, E. (2015) Effect of Sterical Shielding on the Redox Properties of Imidazoline and Imidazolidine Nitroxides, *Journal of Physical Organic Chemistry* 80, 9118-9125.
  98. Qin, P. Z., Butcher, S. E., Feigon, J., and Hubbell, W. L. (2001) Quantitative Analysis of the Isolated GAAA Tetraloop/Receptor Interaction in Solution: A Site-Directed Spin Labeling Study, *Biochemistry* 40, 6929-6936.
  99. Qin, P. Z., Haworth, I. S., Cai, Q., Kusnetzow, A. K., Grant, G. P., Price, E. A., Sowa, G. Z., Popova, A., Herreros, B., and He, H. (2007) Measuring

- nanometer distances in nucleic acids using a sequence-independent nitroxide probe, *Nature protocols* 2, 2354-2365.
100. Cai, Q., Kusnetzow, A. K., Hubbell, W. L., Haworth, I. S., Gacho, G. P., Van Eps, N., Hideg, K., Chambers, E. J., and Qin, P. Z. (2006) Site-directed spin labeling measurements of nanometer distances in nucleic acids using a sequence-independent nitroxide probe, *Nucleic Acids Research* 34, 4722-4730.
  101. Zhang, X., Xu, C. X., Di Felice, R., Sponer, J., Islam, B., Stadlbauer, P., Ding, Y., Mao, L., Mao, Z. W., and Qin, P. Z. (2016) Conformations of Human Telomeric G-Quadruplex Studied Using a Nucleotide-Independent Nitroxide Label, *Biochemistry* 55, 360-372.
  102. Tangprasertchai, N. S., Zhang, X., Ding, Y., Tham, K., Rohs, R., Haworth, I. S., and Qin, P. Z. (2015) An Integrated Spin-Labeling/Computational-Modeling Approach for Mapping Global Structures of Nucleic Acids, *Methods in enzymology* 564, 427-453.
  103. Nguyen, P. H., Popova, A. M., Hideg, K., and Qin, P. Z. (2015) A nucleotide-independent cyclic nitroxide label for monitoring segmental motions in nucleic acids, *BMC biophysics* 8, 6.
  104. Edwards, T. E., Okonogi, T. M., Robinson, B. H., and Sigurdsson, S. T. (2001) Site-Specific Incorporation of Nitroxide Spin-Labels into Internal Sites of the TAR RNA; Structure-Dependent Dynamics of RNA by EPR Spectroscopy, *Journal of the American Chemical Society* 123, 1527-1528.
  105. Edwards, T. E., and Sigurdsson, S. T. (2007) Site-specific incorporation of nitroxide spin-labels into 2'-positions of nucleic acids, *Nature protocols* 2, 1954-1962.
  106. Ward, R., Keeble, D. J., El-Mkami, H., and Norman, D. G. (2007) Distance determination in heterogeneous DNA model systems by pulsed EPR, *Chembiochem : a European journal of chemical biology* 8, 1957-1964.
  107. Ramos, A., and Varani, G. (1998) A new method to detect long-range protein-RNA contacts: NMR detection of electron-proton relaxation induced by nitroxide spin-labeled RNA, *Journal of the American Chemical Society* 120, 10992-10993.
  108. Ding, P., Wunnicke, D., Steinhoff, H. J., and Seela, F. (2010) Site-directed spin-labeling of DNA by the azide-alkyne 'click' reaction: nanometer distance measurements on 7-deaza-2'-deoxyadenosine and 2'-deoxyuridine nitroxide conjugates spatially separated or linked to a 'dA-dT' base pair, *Chemistry* 16, 14385-14396.
  109. Jakobsen, U., Shelke, S. A., Vogel, S., and Sigurdsson, S. T. (2010) Site-Directed Spin-Labeling of Nucleic Acids by Click Chemistry: Detection of Abasic Sites in Duplex DNA by EPR Spectroscopy, *Journal of the American Chemical Society* 132, 10424-10428.
  110. Kerzhner, M., Abdullin, D., Wiecek, J., Matsuoka, H., Hagelueken, G., Schiemann, O., and Famulok, M. (2016) Post-synthetic Spin-Labeling of RNA through Click Chemistry for PELDOR Measurements, *Chemistry*.
  111. Spaltenstein, A., Robinson, B. H., and Hopkins, P. B. (1988) A rigid and nonperturbing probe for duplex DNA motion, *Journal of the American Chemical Society* 110, 1299-1301.
  112. Hustedt, E. J., Kirchner, J. J., Spaltenstein, A., Hopkins, P. B., and Robinson, B. H. (1995) Monitoring DNA Dynamics Using Spin-Labels with Different Independent Mobilities, *Biochemistry* 34, 4369-4375.

113. Piton, N., Schiemann, O., Mu, Y., Stock, G., Prisner, T., and Engels, J. W. (2005) Synthesis of Spin-Labeled Rnas for Long Range Distance Measurements by Peldor, *Nucleosides, Nucleotides and Nucleic Acids* 24, 771-775.
114. Piton, N., Mu, Y. G., Stock, G., Prisner, T. F., Schiemann, O., and Engels, J. W. (2007) Base-specific spin-labeling of RNA for structure determination, *Nucleic Acids Research* 35, 3128-3143.
115. Sicoli, G., Wachowius, F., Bennati, M., and Hobartner, C. (2010) Probing secondary structures of spin-labeled RNA by pulsed EPR spectroscopy, *Angewandte Chemie* 49, 6443-6447.
116. Berliner, L. J., Grunwald, J., Hankovszky, H. O., and Hideg, K. (1982) A novel reversible thiol-specific spin label: Papain active site labeling and inhibition, *Analytical Biochemistry* 119, 450-455.
117. Todd, A. P., Cong, J., Levinthal, F., Levinthal, C., and Hubell, W. L. (1989) Site-directed mutagenesis of colicin E1 provides specific attachment sites for spin labels whose spectra are sensitive to local conformation, *Proteins: Structure, Function, and Bioinformatics* 6, 294-305.
118. Abdullin, D., Hagelueken, G., and Schiemann, O. (2016) Determination of nitroxide spin label conformations via PELDOR and X-ray crystallography, *Physical Chemistry Chemical Physics* 18, 10428-10437.
119. Polyhach, Y., Bordignon, E., and Jeschke, G. (2011) Rotamer libraries of spin labelled cysteines for protein studies, *Physical chemistry chemical physics : PCCP* 13, 2356-2366.
120. Hagelueken, G., Ward, R., Naismith, J. H., and Schiemann, O. (2012) MtsslWizard: In Silico Spin-Labeling and Generation of Distance Distributions in PyMOL, *Applied Magnetic Resonance* 42, 377-391.
121. Fleissner, M. R., Bridges, M. D., Brooks, E. K., Cascio, D., Kálai, T., Hideg, K., and Hubbell, W. L. (2011) Structure and dynamics of a conformationally constrained nitroxide side chain and applications in EPR spectroscopy, *Proceedings of the National Academy of Sciences* 108, 16241-16246.
122. Islam, S. M., and Roux, B. (2015) Simulating the distance distribution between spin-labels attached to proteins, *The journal of physical chemistry. B* 119, 3901-3911.
123. Sahu, I. D., McCarrick, R. M., Troxel, K. R., Zhang, R., Smith, H. J., Dunagan, M. M., Swartz, M. S., Rajan, P. V., Kroncke, B. M., Sanders, C. R., and Lorigan, G. A. (2013) DEER EPR measurements for membrane protein structures via bifunctional spin labels and lipodisq nanoparticles, *Biochemistry* 52, 6627-6632.
124. Stevens, M. A., McKay, J. E., Robinson, J. L., El Mkami, H., Smith, G. M., and Norman, D. G. (2016) The use of the Rx spin label in orientation measurement on proteins, by EPR, *Physical chemistry chemical physics : PCCP* 18, 5799-5806.
125. Hankovszky, O. H., Hideg, K., Goldammer, E. v., Matuszak, E., Kolkenbrock, H., Tschesche, H., and Wenzel, H. R. (1987) New nitroxide reagents for the selective spin-labelling at the guanidino moiety of arginine residues in peptides and proteins, *Biochimica et Biophysica Acta (BBA) - Protein Structure and Molecular Enzymology* 916, 152-155.
126. Berliner, L. J., and McConnell, H. M. (1966) A spin-labeled substrate for alpha-chymotrypsin, *Proceedings of the National Academy of Sciences of the United States of America* 55, 708-712.

127. Adackaparayil, M., and Smith, J. H. (1977) Preparation and reactivity of a new spin label reagent, *The Journal of Organic Chemistry* 42, 1655-1656.
128. Lorenzi, M., Puppo, C., Lebrun, R., Lignon, S., Roubaud, V., Martinho, M., Mileo, E., Tordo, P., Marque, S. R., Gontero, B., Guigliarelli, B., and Belle, V. (2011) Tyrosine-targeted spin labeling and EPR spectroscopy: an alternative strategy for studying structural transitions in proteins, *Angewandte Chemie* 50, 9108-9111.
129. Mileo, E., Etienne, E., Martinho, M., Lebrun, R., Roubaud, V., Tordo, P., Gontero, B., Guigliarelli, B., Marque, S. R., and Belle, V. (2013) Enlarging the Panoply of Site-Directed Spin Labeling Electron Paramagnetic Resonance (SDSL-EPR): Sensitive and Selective Spin-Labeling of Tyrosine Using an Isoindoline-Based Nitroxide, *Bioconjugate chemistry*.
130. Mileo, E., Lorenzi, M., Eroles, J., Lignon, S., Puppo, C., Le Breton, N., Etienne, E., Marque, S. R., Guigliarelli, B., Gontero, B., and Belle, V. (2013) Dynamics of the intrinsically disordered protein CP12 in its association with GAPDH in the green alga *Chlamydomonas reinhardtii*: a fuzzy complex, *Molecular bioSystems* 9, 2869-2876.
131. Le Breton, N., Martinho, M., Mileo, E., Etienne, E., Gerbaud, G., Guigliarelli, B., and Belle, V. (2015) Exploring intrinsically disordered proteins using site-directed spin labeling electron paramagnetic resonance spectroscopy, *Frontiers in molecular biosciences* 2, 21.
132. Hagelueken, G., Hoffmann, J., Schubert, E., Duthie, F. G., Florin, N., Konrad, L., Imhof, D., Behrmann, E., Morgner, N., and Schiemann, O. (2016) Studies on the X-Ray and Solution Structure of FeoB from *Escherichia coli* BL21, *Biophysical journal* 110, 2642-2650.
133. Schmidt, M. J., Fedoseev, A., Bucker, D., Borbas, J., Peter, C., Drescher, M., and Summerer, D. (2015) EPR Distance Measurements in Native Proteins with Genetically Encoded Spin Labels, *ACS chemical biology* 10, 2764-2771.
134. Nakaie CR, G. G., Schreier S, Paiva ACM. (1981) pH dependence of EPR spectra of nitroxides containing ionizable groups, *Brazilian Journal of Medical and Biological Research* 14, 173-180.
135. Schreier, S., Bozelli, J. C., Jr., Marin, N., Vieira, R. F., and Nakaie, C. R. (2012) The spin label amino acid TOAC and its uses in studies of peptides: chemical, physicochemical, spectroscopic, and conformational aspects, *Biophysical reviews* 4, 45-66.
136. Inbaraj, J. J., Laryukhin, M., and Lorigan, G. A. (2007) Determining the Helical Tilt Angle of a Transmembrane Helix in Mechanically Aligned Lipid Bilayers Using EPR Spectroscopy, *Journal of the American Chemical Society* 129, 7710-7711.
137. Toniolo, C., Valente, E., Formaggio, F., Crisma, M., Pilloni, G., Corvaja, C., Toffoletti, A., Martinez, G. V., Hanson, M. P., Millhauser, G. L., George, C., and Flippen-Anderson, J. L. (1995) Synthesis and conformational studies of peptides containing TOAC, a spin-labelled  $C\alpha,\alpha$ -disubstituted glycine, *Journal of Peptide Science* 1, 45-57.
138. Inbaraj, J. J., Cardon, T. B., Laryukhin, M., Grosser, S. M., and Lorigan, G. A. (2006) Determining the Topology of Integral Membrane Peptides Using EPR Spectroscopy, *Journal of the American Chemical Society* 128, 9549-9554.
139. Wright, K., Sarciaux, M., de Castries, A., Wakselman, M., Mazaleyrat, J.-P., Toffoletti, A., Corvaja, C., Crisma, M., Peggion, C., Formaggio, F., and

- Toniolo, C. (2007) Synthesis of Enantiomerically Pure cis- and trans-4-Amino-1-oxyl-2,2,6,6-tetramethylpiperidine-3-carboxylic Acid: A Spin-Labeled, Cyclic, Chiral  $\beta$ -Amino Acid, and 3D-Structural Analysis of a Doubly Spin-Labeled  $\beta$ -Hexapeptide, *European Journal of Organic Chemistry* 2007, 3133-3144.
140. Tominaga, M., Barbosa, S. R., Poletti, E. F., Zukerman-Schpector, J., uacute, lio, Marchetto, R., Schreier, S., Paiva, A. C. M. M., and Nakaie, C. R. (2001) Fmoc-POAC: [(9-Fluorenylmethyloxycarbonyl)-2, 2, 5, 5-tetramethylpyrrolidine-N-oxyl-3-amino-4-carboxylic Acid]: A Novel Protected Spin Labeled  $\beta$ -Amino Acid for Peptide and Protein Chemistry, *Chemical and Pharmaceutical Bulletin* 49, 1027-1029.
141. Wright, K., Wakselman, M., Mazaleyrat, J. P., Franco, L., Toffoletti, A., Formaggio, F., and Toniolo, C. (2010) Synthesis and conformational characterisation of hexameric beta-peptide foldamers by using double POAC spin labelling and cw-EPR, *Chemistry* 16, 11160-11166.
142. Stoller, S., Sicoli, G., Baranova, T. Y., Bennati, M., and Diederichsen, U. (2011) TOPP: a novel nitroxide-labeled amino acid for EPR distance measurements, *Angewandte Chemie* 50, 9743-9746.
143. Borbat, P. P., Crepeau, R. H., and Freed, J. H. (1997) Multifrequency Two-Dimensional Fourier Transform ESR: An X/Ku-Band Spectrometer, *Journal of magnetic resonance* 127, 155-167.
144. Ghimire, H., McCarrick, R. M., Budil, D. E., and Lorigan, G. A. (2009) Significantly improved sensitivity of Q-band PELDOR/DEER experiments relative to X-band is observed in measuring the intercoil distance of a leucine zipper motif peptide (GCN4-LZ), *Biochemistry* 48, 5782-5784.
145. Prisner, T., Rohrer, M., and MacMillan, F. (2001) PULSED EPR SPECTROSCOPY: Biological Applications, *Annual Review of Physical Chemistry* 52, 279-313.
146. Polyhach, Y., Bordignon, E., Tschaggelar, R., Gandra, S., Godt, A., and Jeschke, G. (2012) High sensitivity and versatility of the DEER experiment on nitroxide radical pairs at Q-band frequencies, *Physical chemistry chemical physics : PCCP* 14, 10762-10773.
147. Kruger, K., Grabowski, P. J., Zaug, A. J., Sands, J., Gottschling, D. E., and Cech, T. R. (1982) Self-splicing RNA: Autoexcision and autocyclization of the ribosomal RNA intervening sequence of tetrahymena, *Cell* 31, 147-157.
148. Mattick, J. S., and Makunin, I. V. (2005) Small regulatory RNAs in mammals, *Human Molecular Genetics* 14 Spec No 1, R121-132.
149. Ha, M., and Kim, V. N. (2014) Regulation of microRNA biogenesis, *Nature Reviews Molecular Cell Biology* 15, 509-524.
150. Breaker, R. R., and Joyce, G. F. (2014) The expanding view of RNA and DNA function, *Chemical Biology* 21, 1059-1065.
151. Waters, L. S., and Storz, G. (2009) Regulatory RNAs in bacteria, *Cell* 136, 615-628.
152. Marraffini, L. A., and Sontheimer, E. J. (2010) CRISPR interference: RNA-directed adaptive immunity in bacteria and archaea, *Nat Rev Genet* 11, 181-190.
153. Storz, G., Altuvia, S., and Wassarman, K. M. (2005) An abundance of RNA regulators, *Annual Review of Biochemistry* 74, 199-217.
154. Ward, R., and Schiemann, O. (2013) Structural Information from Oligonucleotides, In *Structural Information from Spin-Labels and Intrinsic*

- Paramagnetic Centres in the Biosciences* (Timmel, R. C., and Harmer, R. J., Eds.), pp 249-281, Springer Berlin Heidelberg, Berlin, Heidelberg.
155. Prisner, T. F., Marko, A., and Sigurdsson, S. T. (2015) Conformational dynamics of nucleic acid molecules studied by PELDOR spectroscopy with rigid spin labels, *Journal of magnetic resonance* 252, 187-198.
  156. Duss, O., Yulikov, M., Allain, F. H., and Jeschke, G. (2015) Combining NMR and EPR to Determine Structures of Large RNAs and Protein-RNA Complexes in Solution, *Methods in enzymology* 558, 279-331.
  157. Kim, N.-K., Bowman, M. K., and DeRose, V. J. (2010) Precise Mapping of RNA Tertiary Structure via Nanometer Distance Measurements with Double Electron–Electron Resonance Spectroscopy, *Journal of the American Chemical Society* 132, 8882-8884.
  158. Wunnicke, D., Strohbach, D., Weigand, J. E., Appel, B., Feresin, E., Suess, B., Muller, S., and Steinhoff, H. J. (2011) Ligand-induced conformational capture of a synthetic tetracycline riboswitch revealed by pulse EPR, *RNA* 17, 182-188.
  159. Krstić, I., Frolow, O., Sezer, D., Endeward, B., Weigand, J. E., Suess, B., Engels, J. W., and Prisner, T. F. (2010) PELDOR Spectroscopy Reveals Preorganization of the Neomycin-Responsive Riboswitch Tertiary Structure, *Journal of the American Chemical Society* 132, 1454-1455.
  160. Duss, O., Yulikov, M., Jeschke, G., and Allain, F. H. (2014) EPR-aided approach for solution structure determination of large RNAs or protein-RNA complexes, *Nature Communications* 5, 3669.
  161. Duss, O., Michel, E., Yulikov, M., Schubert, M., Jeschke, G., and Allain, F. H. (2014) Structural basis of the non-coding RNA RsmZ acting as a protein sponge, *Nature* 509, 588-592.
  162. Sun, Y., Borbat, P. P., Grigoryants, V. M., Myers, W. K., Freed, J. H., and Scholes, C. P. (2015) Pulse dipolar ESR of doubly labeled mini TAR DNA and its annealing to mini TAR RNA, *Biophysical journal* 108, 893-902.
  163. Malygin, A. A., Graifer, D. M., Meschaninova, M. I., Venyaminova, A. G., Krumkacheva, O. A., Fedin, M. V., Karpova, G. G., and Bagryanskaya, E. G. (2015) Doubly Spin-Labeled RNA as an EPR Reporter for Studying Multicomponent Supramolecular Assemblies, *Biophysical journal* 109, 2637-2643.
  164. Wallin, E., and Von Heijne, G. (1998) Genome-wide analysis of integral membrane proteins from eubacterial, archaean, and eukaryotic organisms, *Protein Science* 7, 1029-1038.
  165. Loll, P. J. (2014) Membrane proteins, detergents and crystals: what is the state of the art?, *Acta Crystallographica Section F: Structural Biology Communications* 70, 1576-1583.
  166. Moraes, I., Evans, G., Sanchez-Weatherby, J., Newstead, S., and Stewart, P. D. (2014) Membrane protein structure determination - the next generation, *Biochimica et biophysica acta* 1838, 78-87.
  167. Deisenhofer, J., Epp, O., Miki, K., Huber, R., and Michel, H. (1985) Structure of the protein subunits in the photosynthetic reaction centre of *Rhodospseudomonas viridis* at 3[ångström] resolution, *Nature* 318, 618-624.
  168. Hunte, C., and Richers, S. (2008) Lipids and membrane protein structures, *Current opinion in structural biology* 18, 406-411.

169. Dumas, F., Lebrun, M. C., and Tocanne, J.-F. (1999) Is the protein/lipid hydrophobic matching principle relevant to membrane organization and functions?, *FEBS Letters* *458*, 271-277.
170. Koshy, C., and Ziegler, C. (2015) Structural insights into functional lipid-protein interactions in secondary transporters, *Biochimica et biophysica acta* *1850*, 476-487.
171. Milovanovic, D., Honigmann, A., Koike, S., Gottfert, F., Pahler, G., Junius, M., Mullar, S., Diederichsen, U., Janshoff, A., Grubmuller, H., Risselada, H. J., Eggeling, C., Hell, S. W., van den Bogaart, G., and Jahn, R. (2015) Hydrophobic mismatch sorts SNARE proteins into distinct membrane domains, *Nature Communications* *6*, 5984.
172. Khadria, A. S., and Senes, A. (2015) Fluorophores, environments, and quantification techniques in the analysis of transmembrane helix interaction using FRET, *Biopolymers* *104*, 247-264.
173. Gautier, A. (2014) Structure determination of alpha-helical membrane proteins by solution-state NMR: emphasis on retinal proteins, *Biochimica et biophysica acta* *1837*, 578-588.
174. Wang, S., and Ladizhansky, V. (2014) Recent advances in magic angle spinning solid state NMR of membrane proteins, *Progress in Nuclear Magnetic Resonance Spectroscopy* *82*, 1-26.
175. Georgieva, E. R., Borbat, P. P., Norman, H. D., and Freed, J. H. (2015) Mechanism of influenza A M2 transmembrane domain assembly in lipid membranes, *Scientific Reports* *5*, 11757.
176. Ling, S., Wang, W., Yu, L., Peng, J., Cai, X., Xiong, Y., Hayati, Z., Zhang, L., Zhang, Z., Song, L., and Tian, C. (2016) Structure of an E. coli integral membrane sulfurtransferase and its structural transition upon SCN(-) binding defined by EPR-based hybrid method, *Scientific Reports* *6*, 20025.
177. Ulmschneider, M. B., and Sansom, M. S. P. (2001) Amino acid distributions in integral membrane protein structures, *Biochimica et Biophysica Acta (BBA) - Biomembranes* *1512*, 1-14.
178. Arkin, I. T., and Brunger\*, A. T. (1998) Statistical analysis of predicted transmembrane  $\alpha$ -helices, *Biochimica et Biophysica Acta (BBA) - Protein Structure and Molecular Enzymology* *1429*, 113-128.
179. Holt, A., and Killian, J. A. (2010) Orientation and dynamics of transmembrane peptides: the power of simple models, *European biophysics journal : EBJ* *39*, 609-621.
180. Killian, J. A. (1998) Hydrophobic mismatch between proteins and lipids in membranes, *Biochimica et Biophysica Acta (BBA) - Reviews on Biomembranes* *1376*, 401-416.
181. Grau-Campistany, A., Strandberg, E., Wadhvani, P., Reichert, J., Burck, J., Rabanal, F., and Ulrich, A. S. (2015) Hydrophobic mismatch demonstrated for membranolytic peptides, and their use as molecular rulers to measure bilayer thickness in native cells, *Scientific Reports* *5*, 9388.
182. Freed, J. H., Dzikovski, B. G., and Borbat, P. P. (2010) Channel and Nonchannel Forms of Spin-Labeled Gramicidin in Membranes and Their Equilibria, *The Journal of Physical Chemistry B* *115*, 176-185.
183. Killian, J. A., Salemink, I., de Planque, M. R. R., Lindblom, G., Koeppe, R. E., and Greathouse, D. V. (1996) Induction of Nonbilayer Structures in Diacylphosphatidylcholine Model Membranes by Transmembrane  $\alpha$ -Helical

- Peptides: Importance of Hydrophobic Mismatch and Proposed Role of Tryptophans, *Biochemistry* 35, 1037-1045.
184. de Planque, M. R. R., Greathouse, D. V., Koeppe, R. E., Schäfer, H., Marsh, D., and Killian, J. A. (1998) Influence of Lipid/Peptide Hydrophobic Mismatch on the Thickness of Diacylphosphatidylcholine Bilayers. A <sup>2</sup>H NMR and ESR Study Using Designed Transmembrane  $\alpha$ -Helical Peptides and Gramicidin A, *Biochemistry* 37, 9333-9345.
  185. de Planque, M. R. R., Kruijtzter, J. A. W., Liskamp, R. M. J., Marsh, D., Greathouse, D. V., Koeppe, R. E., de Kruijff, B., and Killian, J. A. (1999) Different Membrane Anchoring Positions of Tryptophan and Lysine in Synthetic Transmembrane  $\alpha$ -Helical Peptides, *Journal of Biological Chemistry* 274, 20839-20846.
  186. van der Wel, P. C. A., Strandberg, E., Killian, J. A., and Koeppe, R. E. (2002) Geometry and intrinsic tilt of a tryptophan-anchored transmembrane  $\alpha$ -helix determined by (<sup>2</sup>H) NMR, *Biophysical journal* 83, 1479-1488.
  187. Holt, A., Koehorst, R. B., Rutters-Meijneke, T., Gelb, M. H., Rijkers, D. T., Hemminga, M. A., and Killian, J. A. (2009) Tilt and rotation angles of a transmembrane model peptide as studied by fluorescence spectroscopy, *Biophysical journal* 97, 2258-2266.
  188. Lueders, P., Jager, H., Hemminga, M. A., Jeschke, G., and Yulikov, M. (2013) Distance Measurements on Orthogonally Spin-Labeled Membrane Spanning WALP23 Polypeptides, *The journal of physical chemistry. B* 117, 2061-2068.
  189. Matalon, E., Kaminker, I., Zimmermann, H., Eisenstein, M., Shai, Y., and Goldfarb, D. (2013) Topology of the Trans-Membrane Peptide WALP23 in Model Membranes under Negative Mismatch Conditions, *The journal of physical chemistry. B* 117, 2280-2293.
  190. Dastvan, R., Bode, B. E., Karuppiiah, M. P. R., Marko, A., Lyubenova, S., Schwalbe, H., and Prisner, T. F. (2010) Optimization of Transversal Relaxation of Nitroxides for Pulsed Electron–Electron Double Resonance Spectroscopy in Phospholipid Membranes, *The Journal of Physical Chemistry B* 114, 13507-13516.
  191. Murphy, D. M. (2004) Principles of pulse electron paramagnetic resonance. By A Schweiger and G Jeschke, Oxford University Press, UK, 2001, 578 pp. ISBN 0 19 850634 1, *Journal of Chemical Technology & Biotechnology* 79, 103-103.
  192. Stoll, S., and Schweiger, A. (2006) *Journal of Magnetic Resonance* 178, 42-55.
  193. Hofer, P., Heilig, R., and Schmalbein, D. *Bruker Spin Report* 152/153, 37-43.
  194. Halbmaier, K., Seikowski, J., Tkach, I., Hobartner, C., Sezer, D., and Bennati, M. (2016) High-resolution measurement of long-range distances in RNA: pulse EPR spectroscopy with TEMPO-labeled nucleotides, *Chemical Science* 7, 3172-3180.
  195. Zheng, G., Lu, X.-J., and Olson, K. (2009) *Nucleic Acids Research* 37 (Web Server issue), W240-W246.
  196. Arnott, S., Hukins, D. W., Dover, S. D., Fuller, W., and Hodgson, A. R. (1973) Structures of synthetic polynucleotides in the A-RNA and A'-RNA conformations: x-ray diffractions analyses of the molecular conformations., *Journal of Molecular Biology* 81, 107-122.
  197. Mathew-Fenn, R. S., Das, R., and Harbury, P. A. B. (2008) Remeasuring the double helix, *Science* 322, 446-449.



198. Liebl, K., Drsata, T., Lankas, F., Lipfert, J., and Zacharias, M. (2015) Explaining the striking difference in twist-stretch coupling between DNA and RNA: A comparative molecular dynamics analysis, *Nucleic Acids Research*.
199. Halbmaier, K., Wegner, J., Diederichsen, U., and Bennati, M. Pulse EPR Measurements of Intramolecular Distances in a TOPP-Labeled Transmembrane Peptide in Lipids, *Biophysical journal* 111, 2345-2348.
200. Kucerka, N., Tristram-Nagle, S., and Nagle, J. F. (2005) Structure of fully hydrated fluid phase lipid bilayers with monounsaturated chains, *The Journal of membrane biology* 208, 193-202.
201. de Planque, M. R. R., Goormaghtigh, E., Greathouse, D. V., Koeppe, R. E., Kruijtzter, J. A. W., Liskamp, R. M. J., de Kruijff, B., and Killian, J. A. (2001) Sensitivity of Single Membrane-Spanning  $\alpha$ -Helical Peptides to Hydrophobic Mismatch with a Lipid Bilayer: Effects on Backbone Structure, Orientation, and Extent of Membrane Incorporation, *Biochemistry* 40, 5000-5010.
202. Dzikovski, B., Tipikin, D., and Freed, J. (2012) Conformational distributions and hydrogen bonding in gel and frozen lipid bilayers: a high frequency spin-label ESR study, *The journal of physical chemistry. B* 116, 6694-6706.
203. Strandberg, E., Özdirekcan, S., Rijkers, D. T., van der Wel, P. C., Koeppe, R. E., 2nd, Liskamp, R. M., and Killian, J. A. (2004) Tilt angles of transmembrane model peptides in oriented and non-oriented lipid bilayers as determined by <sup>2</sup>H solid-state NMR, *Biophysical journal* 86, 3709-3721.
204. Özdirekcan, S., Rijkers, D. T. S., Liskamp, R. M. J., and Killian, J. A. (2005) Influence of Flanking Residues on Tilt and Rotation Angles of Transmembrane Peptides in Lipid Bilayers. A Solid-State <sup>2</sup>H NMR Study, *Biochemistry* 44, 1004-1012.
205. Holt, A., Rougier, L., Réat, V., Jolibois, F., Saurel, O., Czaplicki, J., Killian, J. A., and Milon, A. (2010) Order Parameters of a Transmembrane Helix in a Fluid Bilayer: Case Study of a WALP Peptide, *Biophysical journal* 98, 1864-1872.
206. Özdirekcan, S., Etchebest, C., Killian, J. A., and Fuchs, P. F. J. (2007) On the Orientation of a Designed Transmembrane Peptide: Toward the Right Tilt Angle?, *Journal of the American Chemical Society* 129, 15174-15181.
207. Büttner, L., Seikowski, J., Wawrzyniak, K., Ochmann, A., and Höbartner, C. (2013) *Bioorganic & Medicinal Chemistry* 21, 6171-6180.
208. Purtha, W. E., Coppins, R. L., Smalley, M. K., and Silverman, S. K. (2005) General Deoxyribozyme-Catalyzed Synthesis of Native 3'-5' RNA Linkages, *Journal of the American Chemical Society* 127, 13124-13125.
209. Ponce-Salvatierra, A., Wawrzyniak-Turek, K., Steuerwald, U., Hobartner, C., and Pena, V. (2016) Crystal structure of a DNA catalyst, *Nature* 529, 231-234.
210. Ge, M., Budil, D. E., and Freed, J. H. (1994) ESR studies of spin-labeled membranes aligned by isopotential spin-dry ultracentrifugation: lipid-protein interactions, *Biophysical journal* 67, 2326-2344.
211. Tristram-Nagle, S. A. (2007) Preparation of Oriented, Fully Hydrated Lipid Samples for Structure Determination Using X-Ray Scattering, In *Methods in Membrane Lipids* (Dopico, A. M., Ed.), pp 63-75, Humana Press, Totowa, NJ.



## Publications

2016

- Halbmaier, K., Wegner, J., Diederichsen, U., and Bennati, M. (2016) Measurements of intramolecular distances in a TOPP-labelled transmembrane peptide in lipids by pulsed EPR spectroscopy, *Biophysical Journal* 111, 2345-2348.
- Halbmaier, K., Seikowski, J., Tkach, I., Höbartner, C., Sezer, D., and Bennati, M. (2016) High-resolution measurement of long-range distances in RNA: pulse EPR spectroscopy with TEMPO-labeled nucleotides, *Chemical Science* 7, 3172-3180.

2014

- Tkach, I., Halbmaier, K., Höbartner, C., and Bennati, M. (2014) High-frequency 263 GHz PELDOR, *Applied Magnetic Resonance* 45, 969-979.

2012

- Baumgartner, J., Lesevic, P., Kumari, M., Halbmaier, K., Bennet, M., Körnig, A., Widdrat, M., Andert, J., Wollgarten, M., Bertinetti, L., Strauch, P., Hirt A. and Faivre, D. (2012) From magnetotactic bacteria to hollow spirilla-shaped silica containing a magnetic chain, *RCS Advances* 2, 8007-8009